Contraction/Expansion Flow of Dilute Elastic Solutions in Microchannels

by

Timothy Peter Scott

B.S. Mechanical Engineering
Tufts University, 2002

SUBMITTED TO THE DEPARTMENT OF MECHANICAL ENGINEERING IN
PARTIAL FULFILLMENTOF THE REQUIREMENTS FOR THE DEGREE OF

MASTER OF SCIENCE IN MECHANICAL ENGINEERING
AT THE
MASSACHUSETTS INSTITUTE OF TECHNOLOGY

JUNE 2004

© 2004 Timothy Peter Scott. All rights reserved.

The author hereby grants to MIT permission to reproduce
and to distribute publicly paper and electronic
copies of this thesis in whole or in part.

Signature of Author: _____
Department of Mechanical Engineering
May 7, 2004

Certified by:_____
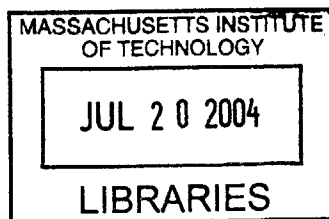Gareth H. McKinley
Professor of Mechanical Engineering
Thesis Supervisor

Accepted by: _____
Ain A. Sonin
Professor of Mechanical Engineering

BARKER

Contraction/Expansion Flow of Dilute Elastic Solutions in Microchannels

by

Timothy Peter Scott

Submitted to the Department of Mechanical Engineering
on May 7, 2004 in Partial Fulfillment
of the Requirements for the Degree of Master of Science in
Mechanical Engineering

ABSTRACT

An experimental study is conducted on the nature of extensional flows of mobile dilute polymer solutions in microchannel. By observing such fluids on the microscale it is possible to generate large strain rates ($\sim$ 50,000 s^{-1}) that are greater than values which have been observed in macroscale contraction flows. Subsequently, large Deborah numbers (equivalent to those observed on the macro scale in high viscosity solutions) are generated for low viscosity solutions without the interplay of significant inertial effects.

High quality microfluidic channels are fabricated using soft lithography techniques. Rheological behavior in these channels is dominated by an abrupt planar contraction, which generates extensional flow in the working fluids. Dilute viscoelastic aqueous solutions of polyethylene oxide are passed through 16:1 planar micro-contractions. Fluids exhibit substantial elastic behavior marked by elastic instabilities followed by subsequent lip vortices and eventually stable vortex growth. The onset of flow instabilities (De =50) and the nature of vortex growth are similar for PEO solutions at various concentrations. Differential pressure measurements indicate that substantial extensional thickening occurs at the onset of flow instabilities and indicate that planar extensional viscosities grow rapidly with increasing strain rates. Also apparent Trouton ratios are calculated indicating that extensional viscosities are two orders of magnitude larger than shear viscosities at high Deborah numbers.

Thesis Supervisor: Gareth H. McKinley
Title: Professor of Mechanical Engineering

Table of Contents

List of Figures

List of Tables

1 Introduction

In recent years advances on the microscale have modified the landscape of many technical fields, including that of fluid mechanicians. The development of microfluidics has renewed interest in many of the classical fluids problems which had been solved in previous years. The microfluidics community is rapidly growing, and the "lab-on-a-chip" phenomenon is becoming applicable to nearly all scientific disciplines. The introduction of rapid prototyping (Effenhauser et al., 1997; Duffy et al., 1998) has now increased the accessibility to microfluidics, making dramatic advances in the field, in both depth and bredth, inevitable.

1.1 Microfluidics

The term microfluidics refers to fluidic devices with smallest feature sizes at lengthscales of one micron or greater. Microfluidic endeavors have focused on various topics ranging from biological systems to fluidic circuitry. And with increasing amounts of research focused on microfluidic technologies, the potential applications of this research are virtually unbounded.

Microfluidic devices have become critical components of various scientific and medical applications. Such small-scale systems are ideal for many chemical and biological endeavors for which small sample sizes and accurately defined geometries are imperative. Microfluidic systems have been developed to assist in the analysis and separation of deoxyribonucleic acid (DNA) (Effenhauser et al., 1997; Chou et al., 1999). Also microfluidic devices have been employed in microfluidic networks with immunoglobins for subsequent assays (Delamarche et al., 1997). These devices have also been employed for cell sorting and cell analysis (Fu et al., 1999). The ultimate goal of microfluidic research is to develop Micro Total Analysis Systems (μTAS), which are capable of performing all sample analyses within one microfluidic chip. However, one of

the limiting factors on this research has been the inability to effectively generate simple valves and pumps to control transportation of samples between analysis chambers.

There are several means of fabricating microfluidic systems, each of which have their own benefits and applications. Soft lithography has become the most utilized means of microfluidic generation in recent years based on its simplicity, cost, efficiency, optical transparency, and compatibility (Quake and Scherer, 2000; Stone and Kim, 2001). Soft lithography uses photolithography to develop a mold off which multiple elastic polymer channels may be reproduced. This polymer can be bonded to glass surfaces and allows for simple fabrication of accurate microchannels. Other techniques for developing microchannels include etching into surfaces such as silicon or glass. These techniques, originally the backbone of microfluidics, are being used less due to the cost and time of fabrication (Quake and Scherer, 2000; Stone and Kim, 2001). Recently techniques have been developed which use chemical modification of surface properties to define microfluidic boundaries (Zhao et al., 2001). These techniques define hydrophobic boundaries to confine flow to hydrophilic regions, but these channels are only able to withstand small pressures.

In microfluidic channels there are several means of developing flow within the network. The simplest method is by creating a pressure gradient across the channel, either by applying pressure at the input or a vacuum at the outlet. These techniques are capable of generating large flow velocities, but require fluids to adhere to the physics of developed pipe flow (parabolic velocity field). Another common technique for driving flow fields in microfluidics is electrophoresis, which involves the use of electrically charged particles which are set into motion by an imposed electric field. This technique allows for a uniform flow field, but it is limited in achievable velocities. Other techniques involve the usage of concentration gradients to stimulate osmotic movements within microchannels. Lastly, boundary conditions, such as surface evaporation, capillary forces, or surface permeability can be used to induce fluid motion. However, the only technique that can generate large flow velocities (> 1 mm/s) in a liquid filled medium is the application of an external pressure gradient.

1.2 Complex Fluids in Microchannels

Non-Newtonian fluids are fluids that appear homogenous on the macroscale but actually have a complex internal microstructure. Because of this internal structure, the properties of these complex fluids can change based on the lengthscales and timescales of associated flows (Bird et al., 1987). Many non-Newtonian fluids are marked by substantial elastic and viscous properties which, unlike and Newtonian fluids, can lead to counterintuitive flow and stress response. The nature of this elasticity is encapsulated in a relaxation time, which is the timescale over which the fluid is able to return to a stress-free condition: larger relaxation times are indicative of more elastic fluids.

Microfluidics as a field has its roots in observing non-Newtonian fluids. Some of the earliest microfluidic devices were designed to test the flow of biological fluids in channels constructed of silicon, designed on the same lengthscale as human capillaries (Karlsson et al., 1991; Wilding et al., 1994). These fluids contain large microstructures (such as proteins, DNA, or blood cells) which can generate highly non-Newtonian behavior in the fluids. Works were primarily focused on the biological aspects of the blood cell behavior, however bulk fluid viscosity was considered. Yet in these studies, the elastic properties of the fluids were always neglected or not understood. There has been little effort to focus on the rheological aspects of complex fluid flow on the microscale.

Groisman and Steinberg examined the use of polymeric liquid in for the purpose of enhanced mixing (2001) in small geometries (3 mm). While these were not microchannels, the small lengthscales involved restrict fluids to low Reynolds numbers and laminar flow, which is typical of microfluidics. In laminar flow of Newtonian fluids, the primary means of mixing fluids is through diffusion. Because diffusion is small over the timescales frequently considered ($\sim$ 100 ms), enhancing fluid mixing is frequently a challenge for many microfluidic devices. Groisman and Steinberg investigated the use of polymeric liquids to enhance mixing at low Reynolds numbers.

The experiments of Groisman and Steinberg involved dissolving a small amount (800 parts per million) of high molecular weight (M_w) polymer (polyacrylamide: M_w = 18,000,000 g/mol) in a Newtonian solvent. Then they compared the mixing of this solution with the mixing of just the Newtonian solvent. The basis for using this polymer was to reach the onset of elastic instabilities in the fluid and, therefore, enhance mixing. This technique is similar to macroscale mixing in which the critical Reynolds numbers are exceeded to induce turbulent mixing. However, for elastic instabilities the critical parameter for the onset of instabilities is the Deborah number (or Weissenberg number):

$$De = \lambda \dot{\gamma} \tag{1.1}$$

where λ is the fluid's relaxation time and $\dot{\gamma}$ is the characteristic shear rate. When the Deborah number becomes large the fluid elements are being sheared faster than they can relax, thus instabilities occur (Bird et al., 1987) and mixing is enhanced (Groisman and Steinberg, 2000).

These experiments made use of the large shear rates generated in small channels to induce elastic instabilities in their viscoelastic solutions. They dyed the two fluid inlets different colors to distinguish between the two flows (see figure 1-1). For the Newtonian solvent, little mixing was observed (only that of diffusion), but for the polymer solution, significant mixing occurs. Clearly the elastic instabilities are the driving force behind allowing the two solutions to mix. They also examined concentration dependence of their mixing device and determined that mixing was observed at concentrations as low as 7 ppm (parts per million) and showed that mixing could be enhanced in even high viscosity solutions with Reynolds numbers as small as 0.016. However, the paper fails to adequately analyze several of the rheological aspects (only the bulk viscosity and characteristic relaxation time are given), which dictate the behavior of the fluids in such geometries.
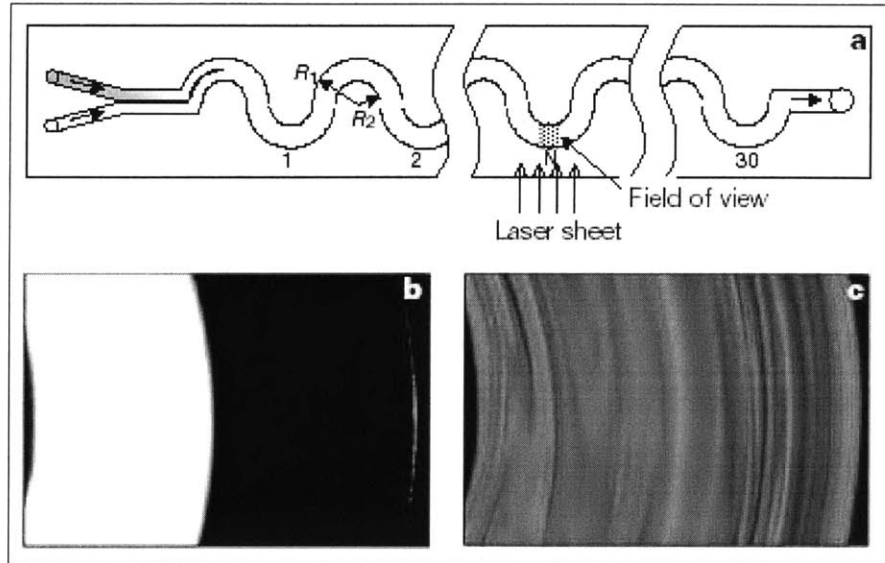
Figure 1-1. (a) Image of the mixer used by Groisman and Steinberg to enhance mixing. (b) Mixing of Newtonian solvent after passing through the mixer at low Reynolds Number (Re = 0.16). (c) Image of the polymeric solution showing extensive mixing at the same flow rate corresponding to a Deborah number of 6.7 (Groisman and Steinberg, 2001).

First, the analysis focuses on observing the mixing in smooth rounded channels, however, there is little reason that such a geometry would enhance fluid mixing. In fact, sharper and smaller geometries would enhance mixing by initializing elastic instabilities more quickly. Stress singularities develop at such corners and have been the source of elastic instabilities in many macroscale experiments (Bird et al., 1987), while rounded corners tend to suppress elastic behavior (Evans and Walters, 1986; Evans and Walters, 1989). Fluid instabilities are observed at Deborah numbers of 3.2, which is greater than unity, but little explanation was offered for the delayed onset of elastic behavior. Also, in considering concentration effects, they failed to quantify relaxation times as the concentration decreased. Thus they did not determine if the critical Deborah number for mixing was consistent with the Deborah number for the initial polymer solutions observed.

In the laboratories of Steven Quake, a great deal of research has been applied to the development of a microfluidic system which is analogous to integrated circuitry, using a fluid in the place of electrons (Unger et al., 2000; Thorsen et al., 2002). However, the difficulty in using such a system is the requirement of a separate controlling layer for

adjusting the flow of fluids in the primary layer (Unger et al., 2000). This layer is required to activate pumps and valves that can be used to transmit or store fluid as desired. A third interconnecting layer is also required for controlling such systems, and the increased complexity has made advances in this area difficult. Recent research has focused on utilizing polymeric fluids in place of this controlling layer based on their non-linear flow properties (Groisman et al., 2003; Groisman and Quake, 2004). By utilizing such fluids, the necessity for moving parts and controlling layers would be reduced, or possibly eliminated, facilitating channel fabrication.

Groisman and Quake have recently published several papers in which polymer solutions are observed in microchannels that are designed to act as control, memory, and logical elements (Groisman et al., 2003; Groisman and Quake, 2004). In their first paper, they discussed the properties of a non-linear resistor which exploits the complex rheological behavior of a polymer solution (Groisman et al., 2003). They used a 250 ppm solution of polyacrylamide (M_w = 18,000,000 g/mol) in a Newtonian solvent as the working fluid. The resistor consisted of a series of contractions and expansions which were designed to instigate flow instabilities in the fluid (see figure 1-2).
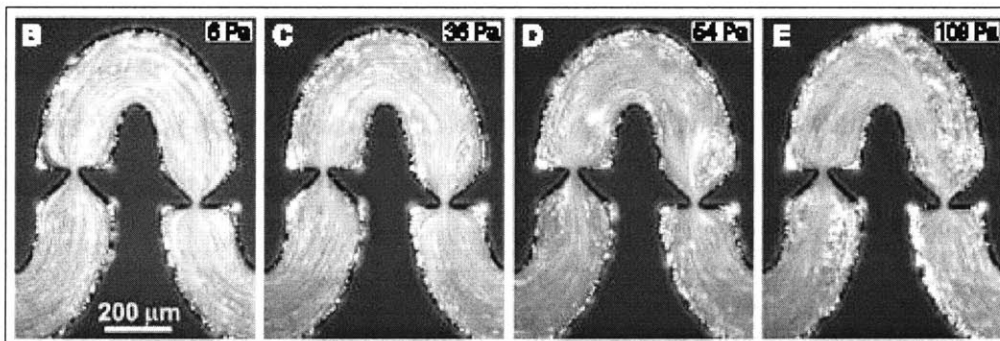
Figure 1-2. An image of the nonlinear resistor developed by Groisman et al. at varying applied pressures. Beyond a critical pressure (~30 Pa) large changes in pressure only correspond to moderate changes in flow rate (Groisman et al., 2003).

They observed that above a critical applied pressure the flow rate only increases a small amount despite gross increases in the applied pressure (see figure 1-3). This behavior corresponded with the onset of vortex behavior in the solution at a Deborah number of De = 0.8. Such vortex behavior was only observed in polymeric solutions where extensional effect inhibit the flow of the solutions through the contractions. Between a

range of applied pressures of nearly an order of magnitude (P ~ 20 – 200 Pa), fluid flow rates only increased by a small amount (~ 20%). They believed that such a microfluidic resistor could be used as a constant current device that can restrict flow rates despite a wide range of applied pressures.
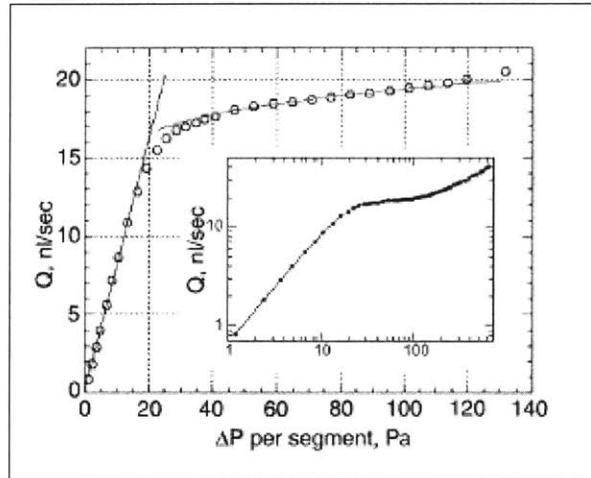
Figure 1-3. Flow rate dependence on applied pressure drop for the nonlinear resistor proposed by Groisman et al. (Groisman et al., 2003).

In this paper they also detail the mechanism of a "flip-flop" memory device based on polymeric fluid principles. They utilize the difference between the flow of extended polymers with that of relaxed polymers to modify flow patterns within the microfluidic chip. Once again they are taking advantage of the extensional behavior of polymer solutions on the small scale and the subsequent vortex behavior that dictates the flow of polymer solutions (see figure 1-4).
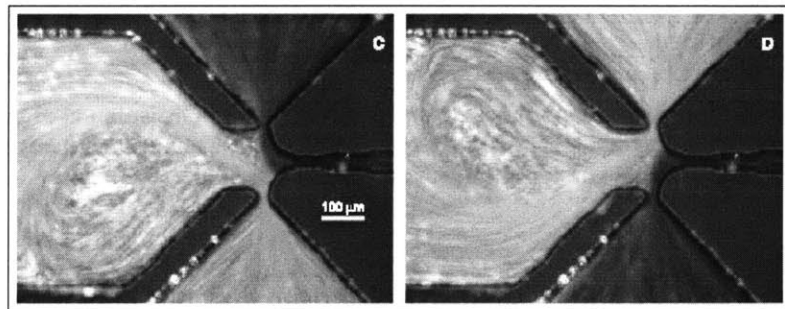
Figure 1-4. Microfluidic flip-flop used by Groisman et al. for controlling flow directions

Again for this study there is little emphasis on the rheological advantages of the fluid and geometries they have chosen. These systems are designed effectively from a functionality

standpoint, and they have used polymer concentrations that are small enough to keep fluid viscosities near that of water ($\eta \sim 1.3$ mPa-s), however they do not extensively quantify the rheological properties of their fluids. They suggest that the fluid is in the dilute to semi-dilute range of concentrations but do not determine the possible effects of molecular interaction on flow properties. They also only examine one polymer concentration, without interpreting the extensional effects of using further diluted solutions of their fluid. Also, the complicated channel geometry leads to asymmetrical vortices, which are not explained in the text. Because no other studies have been performed on similar shapes, there is no explanation for the resulting asymmetry. They also do not quantify the growth of such vortices and whether flow patterns are stable in time or space. Thus, from their results it is difficult to extract any extensive rheological parameters from the flow patterns.

The most recent paper by Groisman and Quake (2004) explains the fundamentals of microfluidic rectifier (a channel whose resistance changes based on the direction of the flow). Once again they use a solution of polyacrylamide (M_w = 18,000,000 g/mol) in a Newtonian solvent. The fluid is passed through a series of saw-toothed expansion contraction geometries. As the Deborah number grows, elastic instabilities develop and flow patterns are no longer reversible (see figure 1-5). Beyond this instability, the fluid acts differently depending on the direction of the flow (see figure 1-6). The extensional behavior is dependent on both the total Hencky strain on the fluid (see section 2.1.3) and the associated strain rate. Based on the geometry the strain should be identical and the strain rate should actually be larger in the direction of the sharper contraction. However, because of the asymmetries in the vortices in the gradual direction, the flow is less stable which translates to a larger amount of total strain in this direction. The more abrupt contraction generates symmetric vortices, which limit swelling at the prior expansion, thus the actual strain is smaller. However this effect is not thoroughly analyzed in their paper.
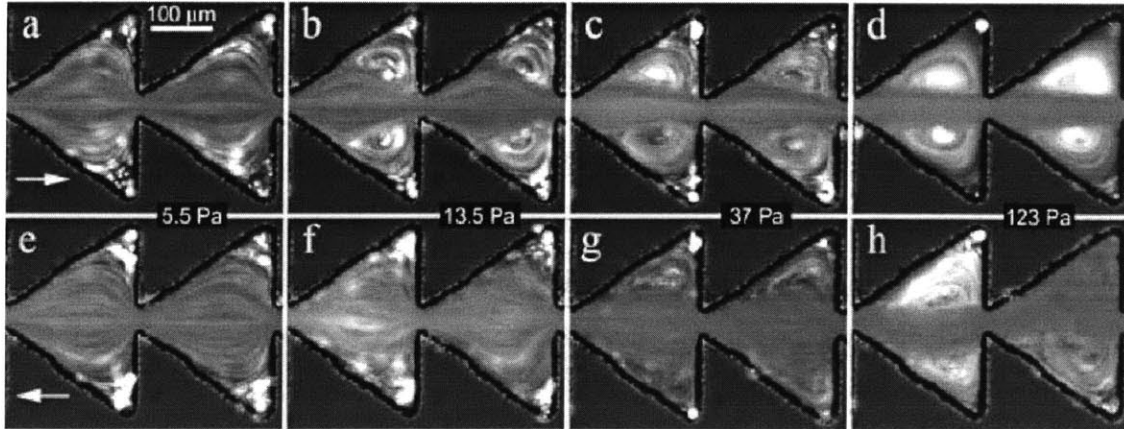
Figure 1-5. Streakline patterns for microfluidic rectifier at different applied pressures. Flow travels forward for pictures (a) - (d) and backward for pictures (e) - (h). The images show the irreversibility of the polymer solutions in microchannels caused by elastic instabilities (Groisman and Quake, 2004).
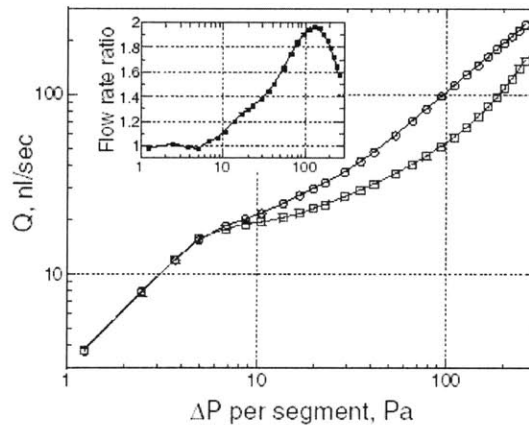
Figure 1-6. Flow rate - pressure dependence of the microfluidic rectifier. Circles indicate forward flow (left to right), while squares are backward flow (Groisman and Quake, 2004).

In this paper they accurately describe the transient nature of the vortices as they grow and note that they are steady in the abrupt expansion, but vary with time in the linear contraction. They also accurately determine the flow rate dependence on the pressure drop over a large range of applied pressures. In each of these papers, they understand the qualitative physics behind their mechanisms, however they do not analyze all the interacting rheological parameters in a quantitative sense.

For this paper on the fluidic rectifier, Groisman and Quake characterize the fluid's relaxation time based on an identical polymer concentration in a more viscous solvent, assuming the relaxation time scales with fluid viscosity. However, this estimate does not account for the polymer-solvent interactions, which can have an effect on the measured relaxation time, even in dilute solutions (Brandrup et al., 1975). They also fail to note the effects of having contraction expansion geometries within such close proximity: the chains may not be able to relax in such a small time, depending on the fluid's velocity. The relaxation times need to be considered in relation to the total residence of the fluid before the next contraction (see section 5.3.3). Because they are attempting to optimize the polymer stretching on one portion of the channel, it would be advantageous to utilize a hyperbolic contraction (see section 1.6) to generate more uniform polymer stretching. More effective rheological characterization and efficient channel design may allow for extensional effects to increase the magnitude of the nonlinearity of the flow resistance.

These few papers on complex fluids focused primarily on the nature of the flow instabilities and subsequent exploitation of these flow characteristics. From a practical standpoint, it is necessary to understand the rheological nature of such flows before being able to optimize the usage of polymeric fluids in microchannels. Understanding the underlying physics behind the evolution of such vortex behavior and the necessary rheological parameters that dictate the onset of such flow anomalies will ultimately lead to useful applications of such microfluidic devices.

1.3 Entry Flow

Based on the observations of Groisman and others, it is desired to understand the fundamentals behind the elastic nature of fluid flows in microfluidic systems. For many years, understanding and predicting entry flow behavior has been one of the classical problems of fluid mechanics. Entry flow has been a landmark challenge for the experimental, computational, and theoretical worlds (Brown and McKinley, 1994).

Entry flow has been well quantified for Newtonian fluids, and the results would not be expected to change on the microscale (see figure 1-7). However, for non-Newtonian fluids, where rheological properties change based on the lengthscales involved in the problem, the resulting behavior is not as certain. Polymer solutions are non-Newtonian fluids in which polymers chains exist on at lengthscales of tens to hundreds of nanometers. Studies have been performed attempting to understand the physics of these fluids on the macroscale (Bird et al., 1987). However, as the lengthscales of the microchannels begin to approach that of the fluid's microstructure (within an order of magnitude) it is unclear that the behavior of the fluids will continue to mimic that of the macroscale. At such small scales the channels begin to "see" the individual polymers instead of only bulk fluid.
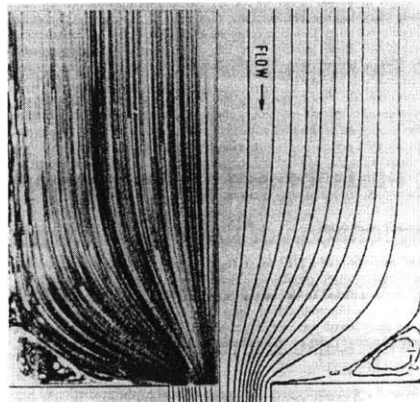
Figure 1-7. Creeping contraction flow of a Newtonian fluid: comparison of experimental results and computational simulations (Boger et al., 1986).

Entry flow is also a problem with many industrial applications from inkjet printing to microinjection molding (see figure 1-8). Inkjet printing is a high volume commercial industry, which is dependent on extensional flows of a non-Newtonian fluid on the microscale. Micromolding is a growing industry based on scaled-down version of injection molding for which small parts ($\sim 1\ \mu$m) can be fabricated by injection of a polymer into a mold through a converging geometry. Naturally, the deficiencies of injection molding on the macroscale (melt fracture and degradation) still need to be addressed on the microscale. Also, studies have been performed observing the behavior of emulsions passing through contraction for the purposes of flow focusing (see figure 1-9). Microfluidic researchers are frequently concerned with the flow of non-Newtonian

fluids (especially bio-fluids) in complicated geometries for which shear effects are insufficient in quantifying material behavior (Beebe et al., 2002). Assessing the fluid rheology also requires knowledge of the fluids interaction with stretching. The relevant parameter for characterizing the ability of the fluid to resist stretching is the extensional viscosity.
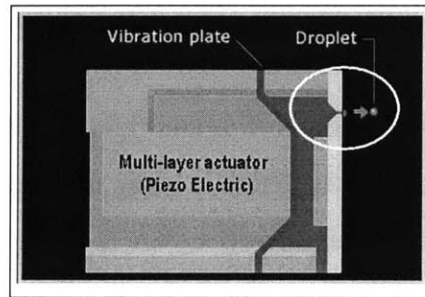
Figure 1-8. Inkjet printing cartridge: a micro-entry flow of a non-Newtonian fluid
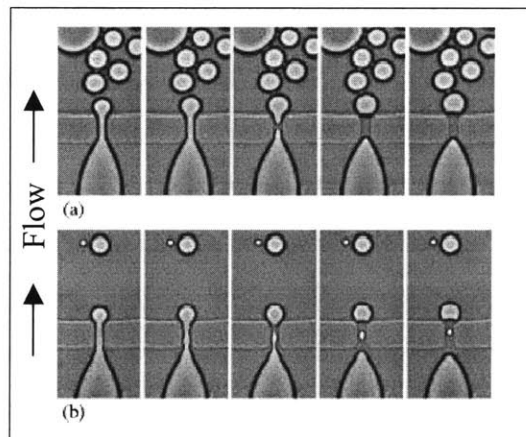
Figure 1-9. Images of a micro-contraction used for flow focusing of emulsions. The contraction is used to generate emulsion droplets (Anna et al., 2003)

1.4 Extensional Viscosity

Just as shear viscosity quantifies the ability of a fluid to resist shearing, the extensional viscosity is a measurement that quantifies the ability of a fluid to resist stretching. The behavior of Newtonian fluids in uniaxial extension is such that its extensional viscosity is three times its shear viscosity (Trouton, 1906). However, for non-Newtonian fluids there is an additional component to the extensional viscosity that frequently increases the

extensional viscosity as strain rates increase in an effect termed extensional thickening. The increase in the extensional viscosity is common to non-Newtonian fluids because of their internal microstructure. As the fluid is stretched, these internal elements, which are initially coiled in a random walk, are elongated into a string-like element. This is especially true in polymer solutions where the polymers are long chains which, when stretched fast enough, exert a large amount of force to prevent further extension.

Typically, at very low strain rates, non-Newtonian fluids act like Newtonian fluids because the fluid relaxes more quickly than it is being unraveled. However, if the fluid is stretched fast enough that the internal microstructure is unable to return to a random walk, extensional thickening takes place. The Deborah number is a comparison of the rate of stretching and the time required for the fluid's microstructure to relax:

$$\text{De} = \lambda \dot{\varepsilon} \tag{1.2}$$

where $\dot{\varepsilon}$ is the strain rate. It has been experimentally and theoretically observed that at Deborah numbers larger than unity, non-Newtonian effects become important (Bird et al., 1987). Extensional thickening refers to increases in a fluids steady-state extensional viscosity as a function of the strain rate: the onset of which is typically at a Deborah number of unity. Another extensional effect is strain hardening which refers to a transient increase in a fluid's extensional viscosity based on the total strain on the fluid. However, for entry flows, the strain rates are controlled by the flow rate, whereas the strain is dictated by the contraction ratio. Thus, the extensional behavior of the fluid is dependent on the strain rate.

Previous experiments have shown that for dilute solutions the additional extensional term can be as large as two orders of magnitude greater than the Newtonian extensional viscosity (Metzner and Metzner, 1970; Spiegelberg et al., 1996; Agarwal and Gupta, 2002; Cooper-White et al., 2002). Most of these experiments however, are limited in their range of strain rates. By working on the microscale, extensional flows can yield additional information about the fluid properties in regimes beyond what has been observed in the past. For low viscosity fluids, relaxation times are small enough that non-Newtonian extensional effects only become important at high strain rates.

Measuring extensional viscosity has been a challenge for experimentalist for many years (Macosko, 1994). For this reason, few extensional rheometers are commercially available. Several techniques are available for measuring the extensional viscosity including filament stretching and fiber wind-up. These techniques are generally restricted to low strain rates and high viscosity fluids. There are a few techniques in which it is possible to measure the extensional behavior of mobile fluids (opposed jet being the most common). Figure 1-10 shows the results of an opposed jet study on solutions of polyethylene oxide (PEO), the same polymer that will be examined in this study (however the solvent viscosities and polymer molecular weights are different). The substantial elastic behavior of these polymers significantly contributes to the extensional viscosity of the solutions. However, in these commercially available techniques, it is not possible to reach the magnitude of strain rates to be examined in this study (see section 5). Using entry flow techniques, mobile fluids can be studied and large ranges of strain rates are readily achievable.
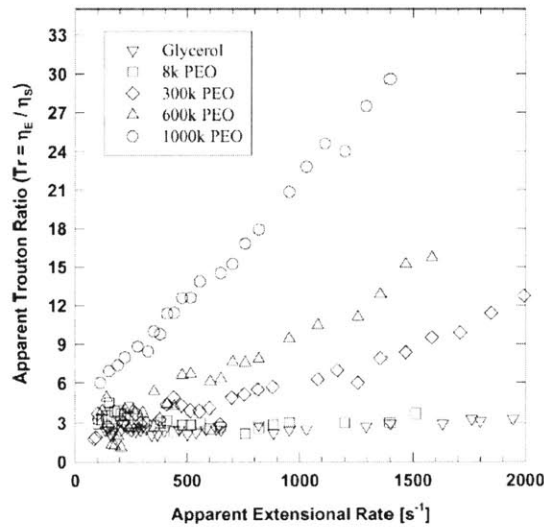
Figure 1-10. Extensional viscosity of various PEO solutions using a opposed jet rheometer

Typically extensional flow problems have been examined on the macroscale. The relevance of moving such observations to the microscale has several implications. First, reducing the size of the geometries allows high strain rates to be achieved:

$$\dot{\varepsilon} \approx \frac{\overline{v}}{L} = \frac{Q}{AL} \qquad\qquad (1.3)$$

where $\overline{v}$ is the average velocity, Q is the flow rate, A is the cross sectional area, and L is a characteristic lengthscale. Because the strain rate scales with the inverse of a length scale, at constant velocities, the strain rates in the present experimentation, at moderate flow rates, are several orders of magnitude greater than previous entry flow systems. The obtainable strain rates exceed those achievable on commercial extensional rheometers, such as the Rheometric RFX opposing-jet rheometer (Hermansky and Boger, 1995; Ng et al., 1996; Cooper-White et al., 2002). Also for previous experiments it was difficult to deal with the inertial effects associated with low viscosity fluids. In microchannels, inertial effects are much smaller, allowing for low viscosity fluids to be examined. Another benefit of using microfluidic devices is their simplicity: microfluidic geometries can be fabricated in a rapid manner and specific to the design requirements (Duffy et al., 1998; Xia and Whitesides, 1998).

One of the drawbacks of using a microfluidic device for measuring extensional properties are that only two-dimensional structures can be generated. This limits the current study to planar geometries, whereas many previous experiments have focused on uniaxial flows (see section 2.1). Another problem with microfluidic systems is that few experiments have been performed trying to make quantitative rheological measurements of these systems. As a result, there has been little emphasis on making sharp vertical sides walls, which is of critical importance to the current project. Another limitation of microchannels, especially ones fabricated using PDMS (polydimethylsiloxane), as in the rapid prototyping technique (Duffy et al., 1998), is their inability to withstand large pressures. While this is infrequently an issue with low-viscosity fluids, it does become a problem as flow rate and viscosity increase.

1.5 Applications for ISN

The Institute for Soldier Nanotechnologies (ISN) is a United States Army funded project focused on developing technology to improve the quality of soldier apparel. One aspect

of this project is focused on the development of microfluidic technologies to monitor and control various components of the soldier uniforms. Because the field of microfluidics is relatively new, understanding of many underlying physical phenomena are required for such devices to become widely used for practical applications.

A great deal of research for ISN has focused on developing field-responsive fluids. These fluids react to external applied fields and subsequently change their mechanical properties. For example, in the presence of a magnetic field, magnetorheological fluids (MR fluids) change from a mobile fluid to a yield stress fluid. Changing the magnitude of this magnetic field can change the energy absorption by larger than an order of magnitude (Deshmukh, 2003).

One goal of ISN is to produce microfluidic interconnects which will encompass the entire uniform. By integrating valves and pumping systems, these interconnects will allow fluids to travel throughout the uniform as desired to specified locations. By developing pumping schemes such as the ones discussed in section 1.2 (Groisman et al., 2003; Groisman and Quake, 2004), circulation of desired fluids to various portions of the uniform is possible. The significance of this work may allow for the energy absorbing fluids to be transported to various sections of the uniform and subsequently activated in order to protect various areas. These fluids can also be circulated to specific areas of the uniform in order to immobilize a region in the case of injury. Thus, understanding the behavior of these fluids in microchannels is required for determining the optimal configurations required for transporting these fluids.

Based on the magnitude of their energy absorbance, field responsive fluids may also be employed in microchannels to appropriately modify flow conditions. Because of their responsive properties, these non-Newtonian fluids can also be used as valves and switches for changing flow patterns within microfluidic devices. In figure 1-11 a switchable microvalve is generated using an MR fluid (5% 500-nm ferrofluid emulsions) that is able to stop the flow of fluid when a field is applied. When the field is released, fluid once again begins to flow in the channel. For this switchable device, it is possible to

halt the fluid motion completely until a minimum pressure is obtained. This behavior is different from that of the fluids used by Groisman and Quake in which the flow rate was held constant only when pressure exceeded a critical value. The MR fluid is capable of altering the motion of the fluid independently of the applied pressure. In order to use such a fluid to stop flow, it is required to pass the fluid through an extensional flow, so that the fluid can resist acceleration. Optimizing the behavior of such a flow requires an understanding of extensional nature of a non-Newtonian fluid passing through such devices. For many ISN applications, complex extensional flows of non-Newtonian fluids play an active role in the functionality of microfluidic systems.
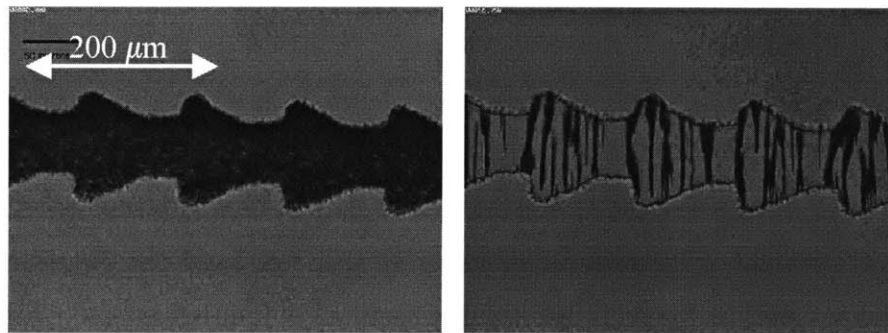
Figure 1-11. MR fluid used as a valve to stop fluid flow. Fluid initially flows through channel (left). Upon applying a magnetic field, flow is stopped (right) (image courtesy of Ramin Haghgooie).

The roughness of the geometries (figures 1-2, 1-4, 1-5, 1-9, and 1-11) in these is another factor that is an important concern in rheology (see section 3.1). Rheological measurements, especially if they are to be compared to numerical simulations, need to be performed on well-defined geometries.

1.6 Project Goal

The goals of this project are to generate extensional flows in microchannels and quantify the extensional viscosity of dilute polymer solutions. Extensional flows, or shear free flows, are characterized by converging streamlines that indicate stretching of the fluid particles. These flows can be generated through a number of different contractions and

expansions geometries. Microfabrication limits the choice of geometries to planar shapes. The velocity gradient for a planar pure extensional flow is:

$$\frac{\partial v}{\partial x} = \dot{\varepsilon} \begin{pmatrix} 1 & 0 & 0 \\ 0 & -1 & 0 \\ 0 & 0 & 0 \end{pmatrix} \tag{1.4}$$

such that the rate of strain tensor is:

$$\dot{\gamma} = \left(\nabla v + \left(\nabla v \right)^{\mathsf{T}} \right) = \dot{\varepsilon} \begin{pmatrix} 2 & 0 & 0 \\ 0 & -2 & 0 \\ 0 & 0 & 0 \end{pmatrix} \tag{1.5}$$

Solving for the flow velocities results in the following two-dimensional flow field:

$$x_1 x_2 = x_{1,0} x_{2,0} \tag{1.6}$$

where the x_1 is motion in the direction of the flow, x_2 is the motion in the secondary direction, and $x_{1,0}$ and $x_{2,0}$ are constants for a given streamline. This formula describes a hyperbolic shape for pure planar extensional flow (see figure 1-12). However, this formula also requires that there is a uniform axial velocity (direction 1) throughout each cross section of the flow. This is difficult to generate in channel flow because of the no-slip boundary condition at the walls. Attempts have been made to lubricate the walls of a hyperbolic geometry to induce slip, but these experiments have generally been unsuccessful: failing to completely eliminate shear from the flow (Macosko, 1994). Some experiments have been conducted on planar geometries with a linearly converging geometry (James and Saringer, 1982), but the majority of experiments have been run on abrupt contractions (Walters and Rawlinson, 1982; Evans and Walters, 1986; Evans and Walters, 1989; Chiba et al., 1990; Chiba et al., 1992; Quinzani et al., 1995; Purnode and Crochet, 1996; Ryssel and Brunn, 1999; Olson and Fuller, 2000; Stelter and Brenn, 2000; Nigen and Walters, 2002; Stelter et al., 2002; Mitsoulis et al., 2003). To compare with previous works done on the macroscale, abrupt contractions were chosen as the means of generating extensional flow for the present study (see figure 1-13).
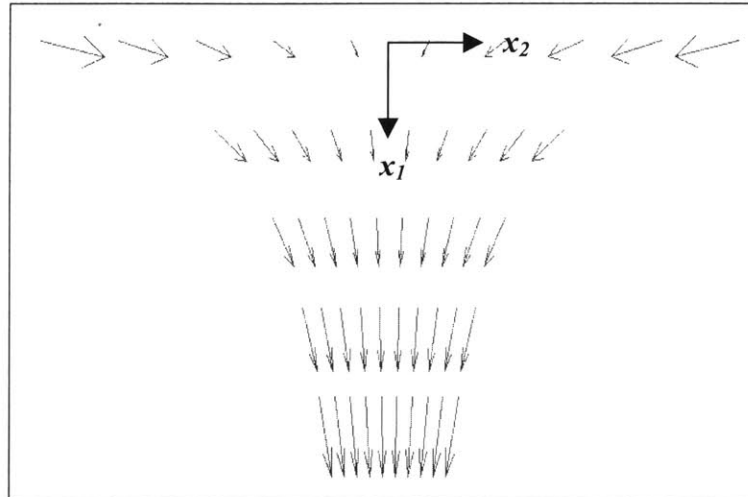
Figure 1-12. Shear-free planar flow
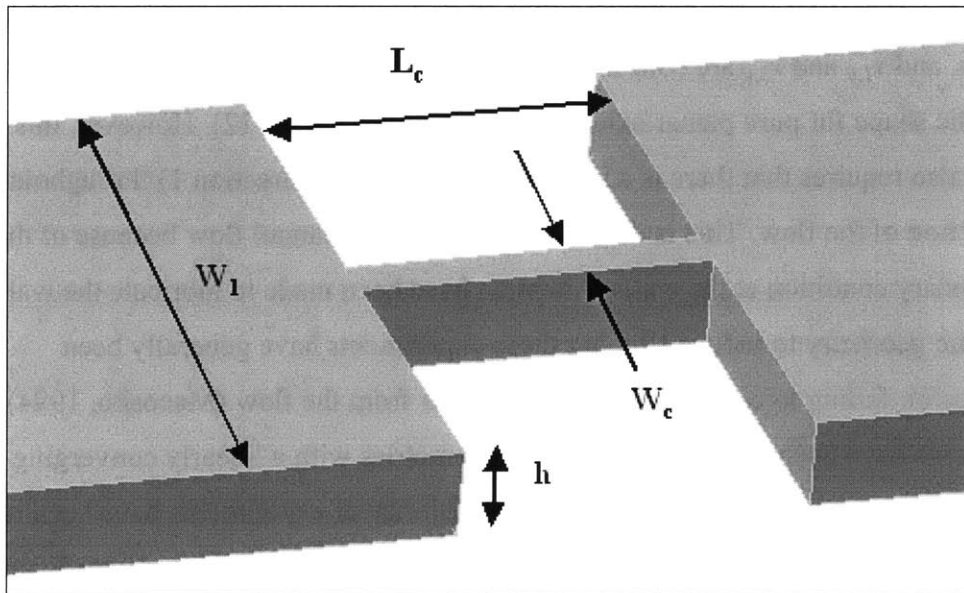
Figure 1-13. Dimensions of microchannels used in the present study

For entry flow studies, several relevant parameters define the nature of the geometry. The contraction ratio (β_P) for a planar geometry is the ratio of the upstream and contraction widths:

$$\beta_P = \frac{W_1}{W_c} = \frac{A_1}{A_c} \tag{1.7}$$

where W_I is the upstream width, W_c is the contraction width, and A_I and A_c are the cross sectional areas of the upstream and downstream contractions. And the aspect ratio (AR_P) of the planar channel is defined as:

$$AR_P = \frac{h}{W_c} \tag{1.8}$$

where h is the height of the channel in the neutral direction. These two dimensionless parameters will be important in comparing the present study with previous entry flow studies.

In the present study extensional flow properties are examined using several different techniques. The fluid motion is examined using streak image photography to observe the vortex patterns and viscoelastic effects of the extensional phenomena arising near the flow entry. Also, extensional viscosities are calculated using an analysis of the additional pressure loss accrued by the extensional motion of the fluid into the contraction. Before continuing, it is necessary to examine previous studies conducted using similar geometries and determine the specific significance of reducing the channel dimensions to the microscale.

2 Background

2.1 Contraction Experiments

2.1.1 Dimensionless Parameters

In order to compare the results from the present study to that of previous works, both axisymmetric and planar, it is necessary to establish an unambiguous means of calculating dimensionless variables. The Deborah number is a dimensionless parameter that is indicative of the relative importance of the elastic stresses of the fluid with the timescale of the system (Bird et al., 1987). The Deborah number is defined for a planar contraction geometry as:

$$\text{De}_P = \lambda \dot{\varepsilon} = \frac{2\lambda \bar{v}_c}{W_c} \tag{2.1}$$

and for axisymmetric contractions:

$$\text{De}_A = \frac{\lambda \bar{v}_c}{R_2} \tag{2.2}$$

where $\bar{v}_c$ is the average velocity in the contraction, W_c is the characteristic dimension of the planar contraction (as in figure 1-13), and R_2 is the contraction radius for an axisymmetric contraction (see figure 2-1). For Newtonian fluids the Deborah number is zero as there is essentially no relaxation time associated with the fluid. As a Newtonian fluid is deformed, the orientation of the individual molecules change, but they have no preferred orientation, so there is no time scale associated with the dissipation of stresses or relaxation of the microstructure. For polymer solutions, when the fluid is stretched or sheared, the polymer chains extend from their original orientation. However, when the motion is ceased the polymer strands are driven to return to their original random orientation as a result of entropic forces. This relaxation process takes a finite amount of time, which is based on a number of different factors depending on the specific polymer and the base solvent. The means for evaluating this quantity for the polymer solutions in this study is explained in section 4.3.
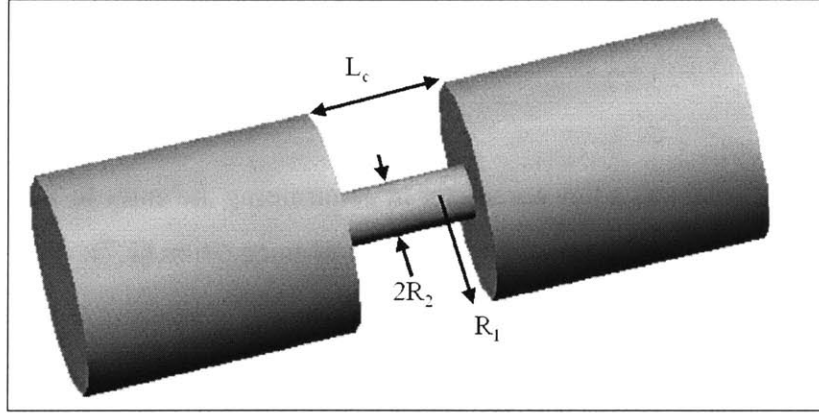
Figure 2-1. Axisymmetric contraction, as used in previous macroscale studies

Inertia also affects the dynamics of any fluid system. The Reynolds number is a comparison of the relative importance of inertial and viscous stresses in the fluid. The Reynolds number for a planar contraction system is defined as:

$$\text{Re}_P = \frac{\rho \bar{v}_c W_c}{\eta_0} \tag{2.3}$$

and for an axisymmetric contraction as:

$$\text{Re}_A = \frac{2\rho \bar{v}_c R_2}{\eta_0} \tag{2.4}$$

where ρ is the fluid density, η_0 is the zero-shear-rate viscosity.

Both the Deborah number and the Reynolds number have an associated lengthscale. Because the present study is performed on the microscale, a comparison of the Deborah number and Reynolds number is greatly affected by this lengthscale. Thus, the elasticity number (El) is used as a dimensionless representation of this comparison:

$$\text{El}_P = \frac{\text{De}_P}{\text{Re}_P} = \frac{2\lambda \eta_0}{\rho W_c^2} \tag{2.5}$$

and for an axisymmetric contraction

$$\text{El}_A = \frac{\lambda \eta_0}{2\rho R_2^2} \tag{2.6}$$

The elasticity number compares the relative importance of elastic effects in the system with inertial and viscous effects, based solely on channel geometry and fluid properties.

The magnitude of this parameter is completely independent of the velocity or shear rate of the fluid.

The contraction ratio (β_P), is a key parameter in determining the entry behavior for a planar contraction. The contraction ratio is defined as in equation (1.7):

$$\beta_P = \frac{W_1}{W_c}$$

And for an axisymmetric contraction the contraction ratio is:

$$\beta_A = \frac{R_1}{R_2} \tag{2.7}$$

where R_1 is the upstream radius.

Non-Newtonian fluids typically possess material properties (namely relaxation time and viscosity) which vary with shear rates ($\dot{\gamma}$). These fluids have been used in many similar contraction geometries, but these effects can be accounted for by considering the rheological properties to be shear rate dependant parameters (Walters and Rawlinson, 1982; Evans and Walters, 1986; Evans and Walters, 1989; Chiba et al., 1990; Chiba et al., 1992; Quinzani et al., 1995; Purnode and Crochet, 1996; Olson and Fuller, 2000; Nigen and Walters, 2002; Mitsoulis et al., 2003). Thus modified dimensionless numbers are also calculated to account for the various effects of shear-thinning and rate-dependent relaxation times. For these non-Newtonian fluids, the elasticity number is no longer independent of the fluid velocity, but the elasticity number does provide a means of comparing the present study with those performed with different fluids and different dimensions.

$$El(\dot{\gamma}) = \frac{2\lambda(\dot{\gamma})\eta(\dot{\gamma})}{W_c^2} \tag{2.8}$$

2.1.2 Entry Behavior

In entry flow problems there is a balance between a number of rheological and inertial stresses that lead to interesting physical phenomena. Various regimes of vortex patterns

develop and are suppressed based on the relative importance of elasticity and inertia. In an attempt to minimize the total energy consumed in the entry process, flow patterns depart from the simple Newtonian converging flow (see figure 2-2).
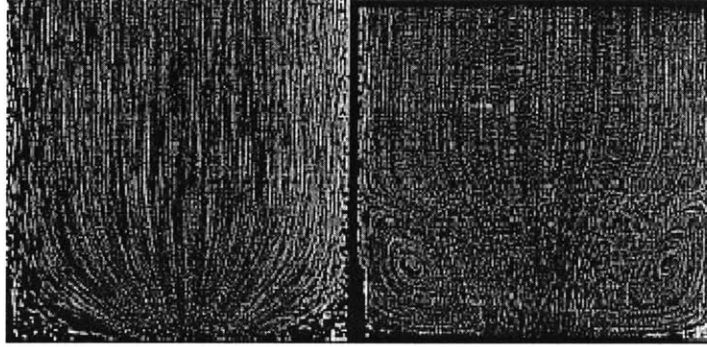
Figure 2-2. Vortex growth for a Boger fluid in an axisymmetric contraction (Rothstein and McKinley, 1998).

For the uniaxial case, a number of different regimes have been observed. At low Deborah numbers, a "Moffatt eddy" is observed in the salient corner, as in Newtonian fluids (see figure 2-3). However, for elastic fluids, as the Deborah number is increased, two different vortex patterns are observed. For some fluids, stress singularities at the re-entrant corner lead to a large steady recirculation zone termed a corner vortex (see figure 2-3). The corner vortex typically grows to the re-entrant corner, and a vortex length (L_v) is computed as the reattachment length. The dimensionless vortex length (χ) yields another means of evaluating the flow:

$$\chi = \frac{L_v}{W_1} = \frac{L_v}{\beta_P W_c} \tag{2.9}$$

At a Deborah number and Reynolds number of zero, the dimensionless vortex length approaches the value for a Moffatt eddy ($\chi_{Moffatt,A} = 0.17$ for an axisymmetric contraction and $\chi_{Moffatt,P} = 0.19$ for a planar contraction (Alves, 2004)). A second regime of fluid instabilities is termed a "lip" vortex. Here the recirculation is no longer steady in time or space and originates at the re-entrant corner. At higher Deborah numbers both of these vortex patterns become unstable, similar to the melt flow instabilities observed in injection molding of polymer melts.
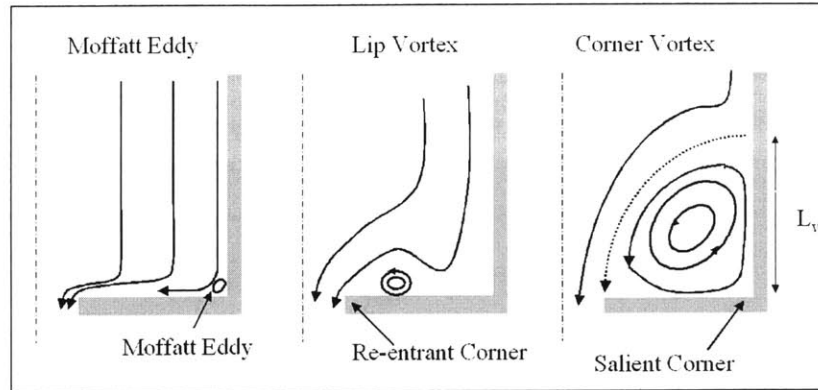
Figure 2-3. Three different vortex regimes observed in axisymmetric contractions

Experimentally, it has been show for axisymmetric contractions that little or no new information is obtained by observing contraction ratios (β_A) greater than 4. Thus, many experiments and simulations have been done at this contraction ratio for its practical and theoretical importance. Typically these experiments are also performed using Boger fluids. Boger fluids are fluids with constant viscosity, yet elastic properties. This quality makes them ideal for observing the rheological behavior of many systems.

It has been proposed that the nature of elastic behavior for creeping flow in an axisymmetric flow is dependent on the Deborah number and the contraction ratio (McKinley et al., 1991) (see figure 2-4). However this analysis fails to account for the associated inertial stresses that are present in the flow of mobile fluids, as is true for the present experiments.
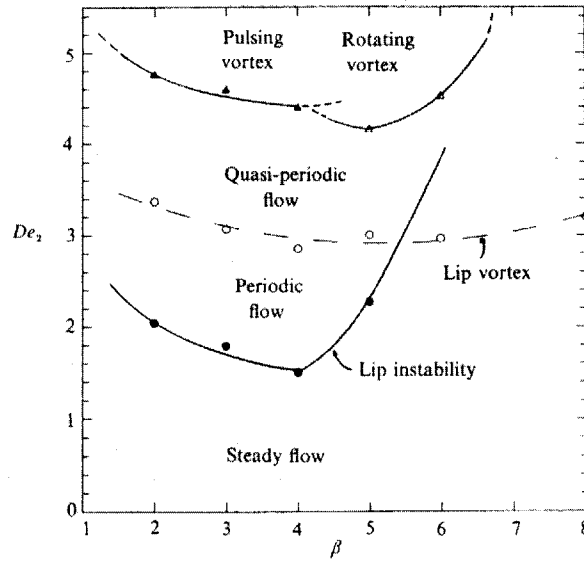
Figure 2-4. Different vortex growth regimes determined based upon contraction ratio and Deborah number (McKinley et al., 1991).

Based on previous axisymmetric experiments, it appears that the relative importance of elastic and inertial stresses determines which regime of vortex behavior occurs (especially at a fixed contraction ratio). For this reason the elasticity number is important in quantifying this and previous studies (see figure 2-5). At large elasticity numbers, vortex behavior and significant growth are observed due to elastic stresses. For elasticity numbers less than unity, inertial stresses diminish or completely suppress vortex behavior. Based on the magnitude of the elasticity number and contraction ratio, it should be possible to predict the subsequent vortex behavior. Because the magnitude of the elasticity number is inversely related to the square of a lengthscale, it is possible to generate large elasticity numbers without using fluids with high viscosity or long relaxation times.
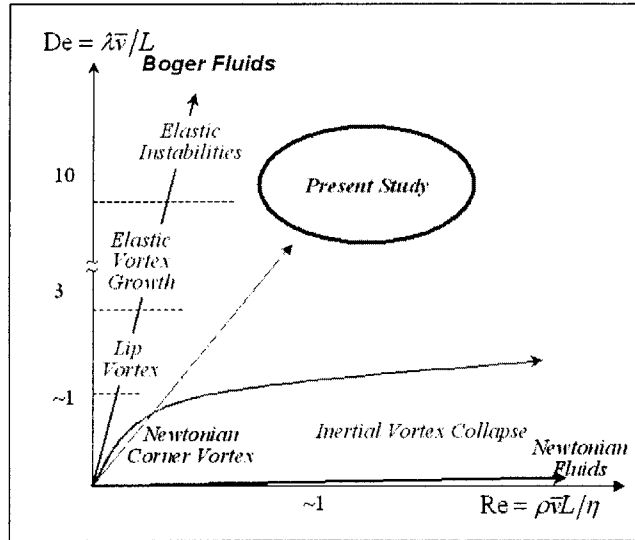
Figure 2-5. Plot of the Deborah number versus the Reynolds number and associated vortex regimes for entry flow experiments

2.1.3 Axisymmetric Studies

As noted in the previous discussions, entry flow experiments have been examined thoroughly on the macroscale. Cable and Boger published a series of papers discussing vortex behavior and giving means of quantifying vortex behavior (Cable and Boger, 1978; Cable and Boger, 1978; Cable and Boger, 1979). These papers also described the developments of divergent flow regimes with counterintuitive flow fields in the contraction region of entry flow (velocity profiles are concave as opposed to the standard parabolic flow shape.) However, all fluids in their study had rate-dependant rheological properties. The fluids studied were aqueous polyacrylamide (PAA) solutions: similar solutions would later be examined heavily in both axisymmetric and planar geometries (Evans and Walters, 1986; Evans and Walters, 1989; Chiba et al., 1990; Chiba et al., 1992).

Boger and Binnington examined the behavior of Boger fluids in contraction geometries (Boger et al., 1986). This analysis resolves that vortex patterns can be observed for constant-viscosity fluids if the elastic properties are significant. Their results suggest that for high viscosity, high elasticity fluids, vortex behavior is observed in the form of both

38

lip vortices and corner vortices which can interact and contribute to different flow patterns.

David Boger published an encompassing review of the research that had been performed on flows through contractions (Boger, 1987). He reports that the entry flow problem has been solved for Newtonian and inelastic non-Newtonian fluids, but remains unsolved for flow of viscoelastic fluids, both with and without shear-thinning properties. He concludes that the definitive property that dictates the fluid motion in entry flows is the extensional viscosity. However, because extensional viscosity is dependent on both strain and strain rate, the shape and size of geometries lead to different flow patterns. For elastic fluids, even with nearly identical shear rheological properties, fluids can have vastly different extensional viscosities, which significantly contributes to the entry flow behavior. These extensional viscosities can lead to either the development of lip vortices, corner vortex growth, or both.

McKinley et al. analyzed the effect of an entry flow at different contraction ratios in an attempt to quantify and categorize the conditions required for the onset of lip vortices (1991). They quantified the axial flow velocities using laser-Doppler velocimetry (LDV) to consider the extensional nature of the flow field. Using flow visualization, they accurately documented the onset of several different lip instabilities that were both periodic and seemingly arbitrary in nature.

Rothstein and McKinley resolved many issues that had arisen over the course of many papers on axisymmetric contractions (1998; 2000). They used pressure measurements to quantify the substantial entrance effects of Boger fluids in a contraction geometry. These papers also concludes that different elastic fluids can possess different vortex behavior, despite similar Deborah numbers (Rothstein and McKinley, 1998). This behavior is explained by a dimensionless normal stress ratio ($\aleph$) which compares the normal stresses associated with shear flow with the elastic effects of extension:

$$\aleph = \frac{N_1 / \eta_0 \dot{\gamma}}{(\tau_{zz} - \tau_{rr}) / \eta_0 \dot{\varepsilon}} = \frac{\text{Sr}(\dot{\gamma})}{\text{Tr}(\varepsilon)} \qquad (2.10)$$

where $Sr(\dot{\gamma})$ is the shear-rate-dependent stress ratio, N_1 is the first normal stress difference in shear, $\tau_{zz} - \tau_{rr}$ is the first normal stress difference in a uniaxial extension, and $Tr(\varepsilon)$ is the Trouton ratio based upon the Hencky strain (see discussion below). They concluded that if this ratio ($\aleph$) is greater than $\aleph = 0.055$, corner vortex growth is dominant flow behavior. At lower stress ratios, lip vortices were observed to dominate the flow patterns. This relationship explains why at higher Deborah numbers the corner vortex typically supplants the lip vortex: the finite extensibility of the polymer chains leads to shear-thinning and extensional effects become dominant. This result also explains why for large contraction ratios, in which total strain is larger, the extensional stresses dominate the normal stress difference and lip vortices are not observed.

While vortex behavior was consistently observed on the macroscale in axisymmetric contractions of viscoelastic fluids, planar contractions are not necessarily two-dimensional flows (based on the confinement in the neutral direction). The two-dimensional assumption simplifies the behavior in uniaxial contractions. Thus, these two different entry flow regimes do not necessarily predict identical flow behavior. Experiments which have compared the two different types of flows for identical fluids have typically found different behavior both qualitatively and quantitatively (James and Saringer, 1982; Nigen and Walters, 2002).

In a planar contraction there has not been any significant examination to determine if a contraction ratio (β_P) exists that has the same significance as a 4:1 contraction in axisymmetric geometries. The resulting Hencky strain (ϵ) on a fluid in a contraction geometry is defined as (McKinley et al., 1991):

$$\varepsilon = \int_{-\infty}^{+\infty} \dot{\varepsilon}\,dt = \int_{v_z(-\infty)}^{v_z(+\infty)} \frac{dv_z}{v_z}\,dt \tag{2.11}$$

For axisymmetric flows this simplifies to:

$$\varepsilon_A = 2\ln(\beta_A) \tag{2.12}$$

But for a planar contraction the total strain is:

$$\varepsilon_P = \ln(\beta_P) \tag{2.13}$$

The corresponding contraction ratio for the planar case to a 4:1 axisymmetric contraction, which maintains an equivalent strain and likewise an equivalent area reduction, would be $\beta_P = 16$. But experiments by Evans and Walters have shown that at higher contraction ratios new information can be obtained (1986).

The ratio of shear rates for the upstream and the downstream portions of the channels are also different for planar and axisymmetric contractions. The shear rate is found for a channel to be:

$$\dot{\gamma} = \frac{\bar{v}}{L} \tag{2.14}$$

where L is once again a characteristic length. Thus, for an axisymmetric contraction the ratio of shear rates is:

$$\frac{\dot{\gamma}_2}{\dot{\gamma}_1} = \left(\frac{Q}{\pi R_2^3}\right)\left(\frac{\pi R_1^3}{Q}\right) = \beta_A^3 \tag{2.15}$$

However for an infinite planar contraction the resulting ratio of shear rates is:

$$\frac{\dot{\gamma}_c}{\dot{\gamma}_1} = \left(\frac{Q}{hW_c^2}\right)\left(\frac{hW_1^2}{Q}\right) = \beta_P^2 \tag{2.16}$$

Thus there are clearly different conditions dictating the behavior of the fluid in a planar contraction from that of an axisymmetric contraction.

2.1.4 Planar Studies

While a great deal of attention has been paid to the uniaxial contraction flow problem, fewer studies have been performed in planar geometries. An early paper by Cogswell summarized work dealing with the planar contraction problem but did not include any experimental data (Cogswell, 1978). This paper did introduce the idea of a secondary expansion at the entrance of planar contractions and even mentioned a modification capable of suppressing the expansion for purely converging flows. This same behavior would later be observed in several experiments (Chiba et al., 1990; Chiba et al., 1992).

In the present thesis, a number of experimental results on planar contractions are examined. For each experiment, the range of calculated Deborah numbers and Reynolds numbers are computed to determine the magnitudes of these quantities in comparison to the present study. Figure 2-3 plots the relationship between these two dimensionless quantities for each planar contraction experiment.
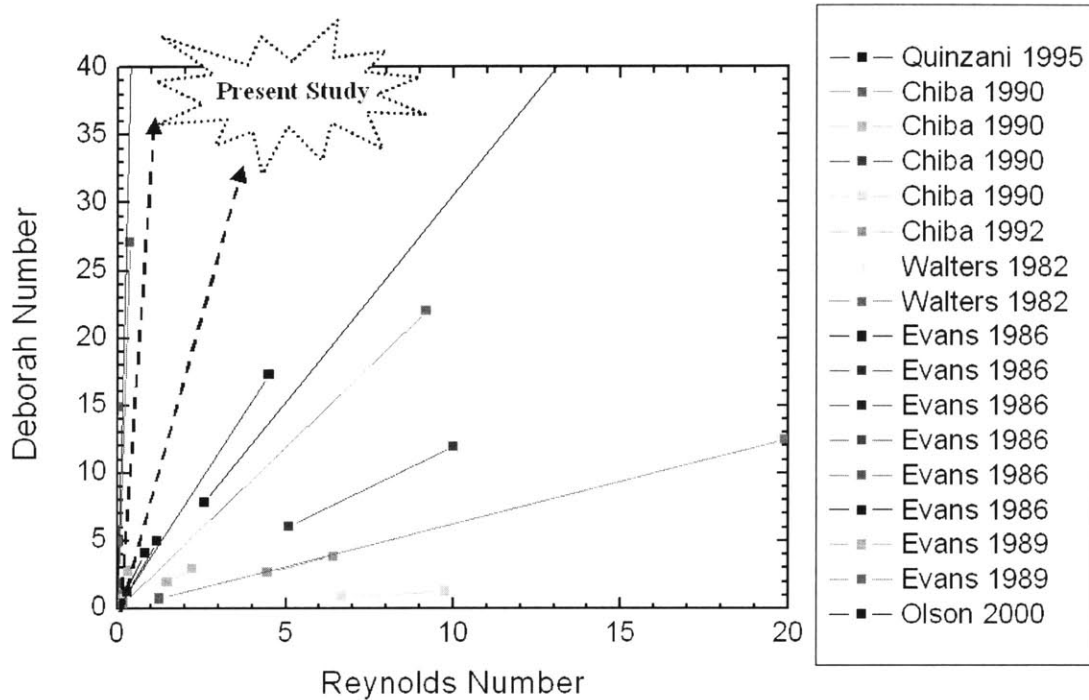
Figure 2-6. Comparison of the dimensionless flow parameters of previous planar contraction studies performed on the macroscale

Figure 2-4 reproduces the results of figure 2-3, however it accounts for the shear rate dependent effects in the fluids that were used in a number of experiments. For many of these experiments insufficient rheological data was given, especially for relaxation times. To compensate, a characteristic 'Maxwell' relaxation time was determined assuming an upper convected Maxwell-like fluid:

$$\lambda = \frac{N_1(\dot\gamma)}{2\eta(\dot\gamma)\dot\gamma^2} \tag{2.17}$$

where N_1 is the first normal stress difference. Still many of the papers did not adequately quantify their rheological parameters and associated relaxation times cannot always be determined from their results (Nigen and Walters, 2002).
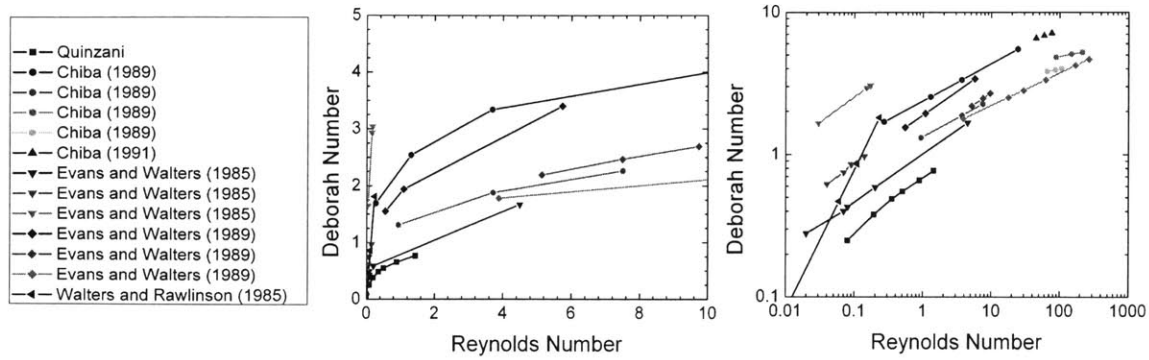
Figure 2-7. Comparison of the dimensionless flow parameters for experiments, accounting for rate-dependant rheological properties

Walters and Rawlinson examined a planar entry flow problem in 1982 and found no vortex behavior for several different Boger fluids . These fluids were similar to Boger fluids that had been used in axisymmetric studies in which vortex behavior was observed (Walters and Webster, 1982). However, they did observe asymmetric instabilities (similar to the flow instabilities seen at large Deborah numbers in axisymmetric studies) at Deborah numbers of approximately De = 15.

Evans and Walters performed a number of experiments to examine the behavior of both Boger fluids and shear-thinning PAA solutions in planar contractions (Evans and Walters, 1989). Their results suggested that elastic behavior, namely vortex enhancement, is only observed for highly shear thinning fluids ($n \sim 0.4$) (see figure 2-8). Boger fluids exhibited no vortex behavior until flow instabilities were reached. These papers also examined the effects of rounding corners on flow patterns. They determined that by rounding the re-entrant corners, vortices could be suppressed in shear thinning fluids.
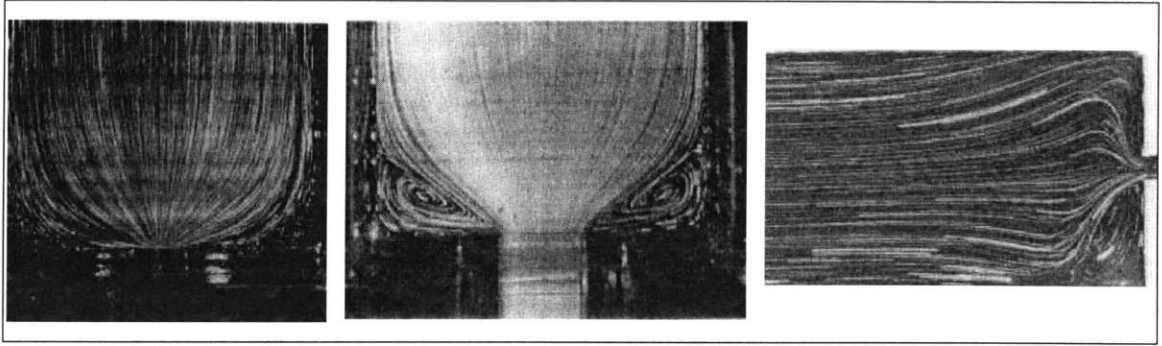
Figure 2-8. Planar contraction results for a Boger Fluid in an 80:1 contraction (left) (Evans and Walters, 1986): Re = 0.18, De = 0.10, a 0.5 % PAA solution in a 4:1 contraction (center) (Evans and Walters, 1989): Re = 7.5, De = 2.7, and a 0.1 % PAA solution in a 10:1 contraction (right) (Chiba et al., 1990): Re = 89, De = 4.6

Chiba et al. performed a number of experiments using aqueous solutions of PAA in high aspect ratio ($25 < AR_P < 75$) planar contractions (1990; 1992). It was assumed that high aspect ratios would permit a two-dimensional approximation. They observed many complex stream patterns that appeared to show the flow was diverging then converging as the fluid entered the contraction (see figure 2-8). This was similar to the secondary die-swell behavior predicted by Cogswell 10 years earlier. They determined the patterns to be a consequence of elastic effects causing streamlines to converge in the vertical plane, thus the flow was actually three-dimensional. However, they still did not observe any of the typical viscoelastic behavior associated with vortex growth observed in the axisymmetric configurations.

Quinzani et al. examined the behavior of complex concentrated polymer solutions, accounting for multiple relaxation times in a planar contraction (1995). They compared experimental results for extensional viscosity with simulations (using various constitutive equation) and found a strong correlation especially using the Phan-Thien-Tanner model. They observed extensional thickening at Deborah numbers below unity. However, they did not perform flow visualization to determine the nature of vortex behavior for their fluids.

Purnode and Crochet attempted to simulate the results of Evans and Walters for planar and axisymmetric contractions (1996). Their results matched the results of Evans and

Walters for shear thinning PAA solutions. However, due to numerical difficulties, they did not examine Boger fluids for the same contractions to determine if their simulations were still valid for constant viscosity, elastic fluids.

Nigen and Walters attempted to once again quantify the behavior of Boger fluids in planar contractions as compared with axisymmetric contractions (2002). However, in this study, they also incorporated PIV (particle imaging velocimetry) and pressure measurements. Despite their more advanced techniques, they still observed no influence of the fluid elasticity in any of the measurements in planar contractions. Pressure drops followed a linear Newtonian path (see figure 2-9) and enhanced vortex patterns were absent. However, they did not specify the range of Deborah numbers considered or sufficient rheological information about the fluids considered.
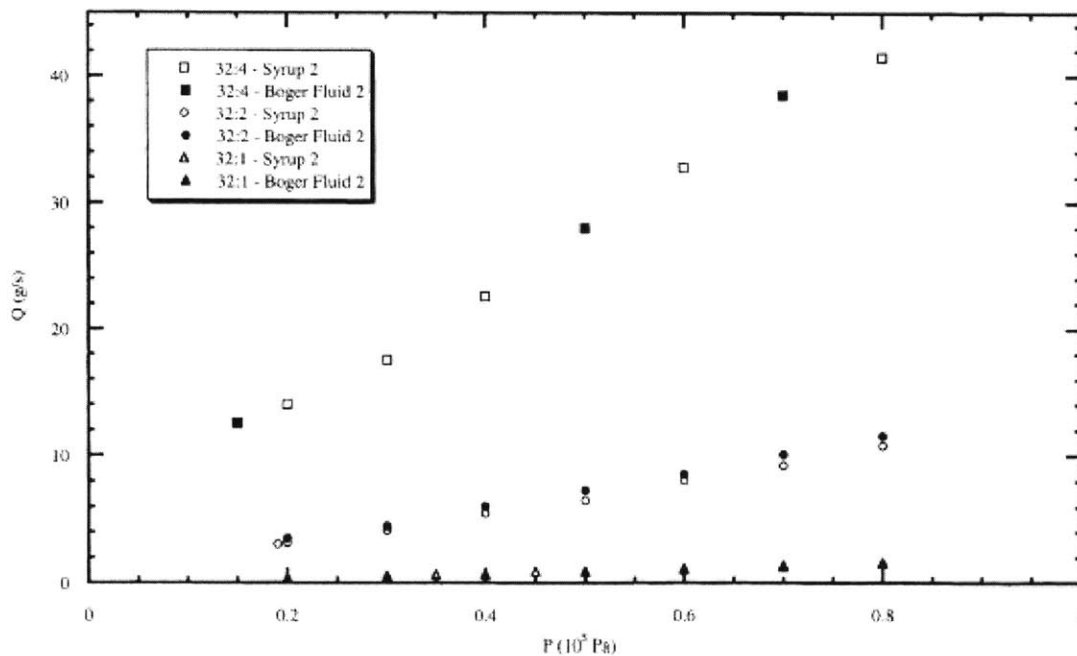
Figure 2-9. Flow rate versus applied pressure for the contraction flows of Boger fluids (Nigen and Walters, 2002).

In only a few of these experiments were measurements of extensional viscosity or entry pressure drop examined. However, several experiments have been performed previously to determine the nature of extensional viscosities in planar geometries. James and Saringer generated a planar sink flow of a dilute polymer solution in a linearly

converging die in an attempt to quantify the non-Newtonian effects (1982). For the wedge-shaped channel no pressure dependence was observed. In the same paper it was determined that for the same fluid in a conical geometry, the pressure loss was dependent on the fluid's extension rate: the pressure drop grew to nearly 4 times its Newtonian prediction at high strain rates. The only study of planar geometry in which extensional viscosities were found to be dependent on strain rates was the study by Quinzani et al. (1995).

From figures 2-3, it is clear in which regime of parameter space the present study lies in relation to previous studies in terms of dimensionless fluid and flow parameters. By using a microfluidic device the present study is able to reach new regions in parameter space. Because of the low concentration of polymer, the fluids in the current study do not show large shear rate dependence (see section 4). But because they are mobile, the experiments are not restricted to zero Reynolds number. The resulting elasticity numbers are large enough to anticipate elastic behavior similar to what has been observed in axisymmetric experiments for Boger fluids.

The problem with comparing all of these studies is the difference in the fluid and channel properties. Even though elasticity numbers may be comparable, contraction ratios are frequently different and so are aspect ratios. The elastic behavior in a contraction geometry are at least a function of the Deborah number, Reynolds number, and contraction ratio. Also, in a contraction, the shear rates vary greatly in the direction of the flow and normal to the flow, thus the behavior of shear thinning fluids can act different from Boger fluids. To appropriately relate all of these experiments, it would be necessary to account for all these factors. Appropriate analyses of these quantities would require a complicated three-dimensional viscoelastic simulation based on relevant parameters (Alves, 2004).

2.1.5 Expansion Behavior

Much less research has been performed in observing the exit behavior of fluids. The reason for this is likely because entry flow has typically been most applicable for polymer injection. At the fluid entry, instabilities must be accounted for to maintain uniform flow of polymer melts. At an expansion, the large viscoelastic forces that generate vortex behavior, work in an opposite fashion, suppressing vortex behavior (White et al., 1987; Townsend and Walters, 1994; Olson and Fuller, 2000). But it is also known that inertial forces can generate expansion vortex behavior in the limit of low elasticity (Townsend and Walters, 1994). Townsend and Walters analyzed expansion of viscoelastic and Newtonian fluids in identical channels. They found that at high Reynolds numbers Newtonian fluids generated large circulation zone, but for the same Reynolds number (Re = 10) and a low Deborah number (De = 1), the vortex exit vortex behavior was completely suppressed (Townsend and Walters, 1994).

Expansions are typically observed for high-viscosity, high-elasticity fluids, where elastic forces dominate these inertial effects (Rothstein and McKinley, 2000; Kim et al., 2001). Because the present study is aimed towards examining low viscosity fluids, it is of interest to determine if these inertial stresses will be large enough to overcome the elastic effects in expansions. For microfluidic applications understanding this exit behavior is a key component to controlling the subsequent fluid motion. In using polymeric fluids for valves and pumps, as Groisman and Quake were attempting, it is necessary to understand and control the outflow of fluid (Groisman et al., 2003; Groisman and Quake, 2004). They did not analyze the rheological aspects of this viscoelastic expansion behavior in their applications, but it was a relevant parameter for the devices they constructed.

2.2 Calculating Extensional Viscosity: Cogswell's Method

Based on the entry flow of a fluid it is possible to calculate the extensional viscosity. This calculation is based on the pressure loss accrued in the entry flow. The planar extensional viscosity of a fluid is defined as:

$$\eta_P = \frac{\tau_{11} - \tau_{22}}{\dot{\varepsilon}_0} \qquad (2.18)$$

where $\tau_{11} - \tau_{22}$ is the first normal stress difference and $\dot{\varepsilon}_0$ is a constant strain rate. From equation (1.5) it is clear that the planar extensional viscosity for a Newtonian fluid is four times the shear viscosity. In order to determined the apparent extensional viscosity for a contraction flow, it is necessary to decompose the pressure drops in the channel. Figure 2-10 illustrates the various sources of pressure loss as the fluid flows into the small contraction. Fluidic devices are typically a series of channels of varying contraction lengths (L_c). Using a Bagley Chart, the entry pressure loss (ΔP_{en}) can be determined by extrapolating to a zero contraction length (see figure 2-11). The pressure drop across the contraction is determined to be:

$$\Delta P = \Delta P_c + \Delta P_{en} \qquad (2.19)$$

where ΔP_c is the pressure loss due to fully developed channel flow (see section 5.2.1 for the calculated magnitude of these pressure drops). As the length of the channel approaches zero, this pressure loss due to channel flow approaches zero and the pressure drop across the contraction is dominated by the entry pressure loss (see figure 2-11). The magnitude of the entry pressure loss is associated with the extensional component of fluid stretching as it enters the contraction. However, decomposing the entry pressure drop into shear and extensional components is more complicated.
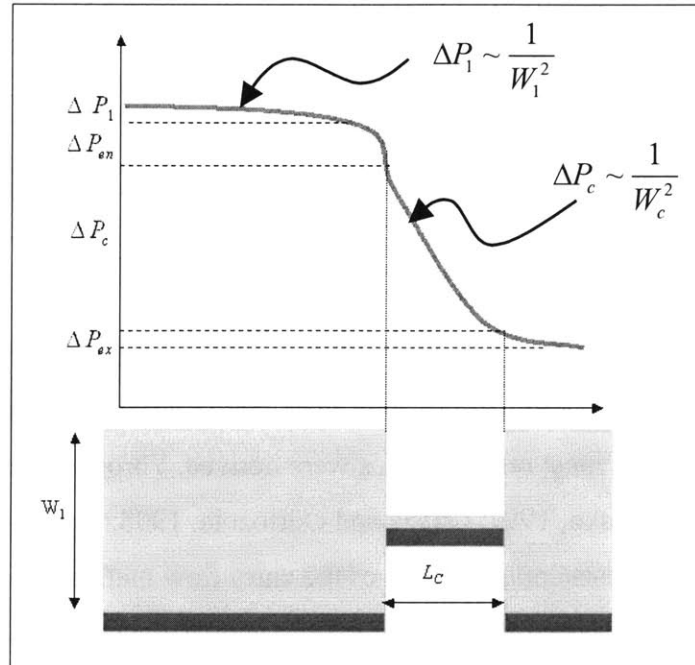
Figure 2-10. Sources of pressure loss along the microchannels
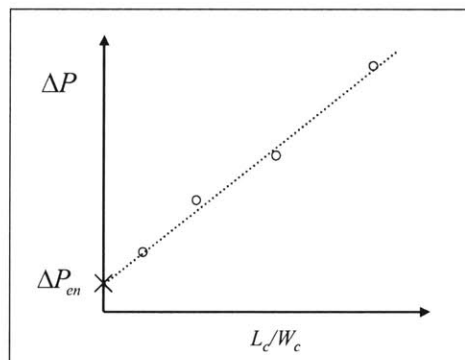
Figure 2-11. Sample Bagley plot: pressure drop is extrapolated to zero contraction length

Starting with Metzner and Metzner a number of papers have been written that propose, validate, and revise techniques for determining the extensional viscosity from entrance pressure data (1970). In the early paper of Metzner and Metzner, the contraction flow geometry was first examined as an extensional flow in an attempt to extract rheological elongational information. Their analysis assumed that the flow was completely shear-free, which leads to the following expression for the apparent extensional viscosity and the associated strain rate:

$$\eta_{P,a} = \frac{\Delta P_{en}}{\dot{\varepsilon}}$$ (2.20)

where the apparent extension rate is as in equation (1.3):

$$\dot{\varepsilon} = \frac{\overline{v}}{R_2}$$

Cogswell, in 1972, analyzed the entry flow problem incorporating the effects of shear in addition to elongation (Cogswell, 1972). This work would become the landmark for entry flow analysis from which most other theories were derived. Through many validations (Padmanabhan and Macosko, 1997; Gotsis and Odriozola, 1998; Rajagopalan, 2000), it still holds as the most consistently accurate of the entry flow methods despite its simplicity and precarious assumptions. His analysis approximated the flow to be locally fully developed in the straining region of the flow. He also assumed the flows to be converging in conical (for axisymmetric flow) or wedge-shaped (planar) patterns. The fluids are assumed to be power-law fluids, for which material properties are dependent on the shear rate. The results of his analysis lead to the following formulas for calculating planar extensional viscosity and the associated strain rates strictly from the imposed flow rate and the measured entrance pressure (ΔP_{en}):

$$\dot{\varepsilon} = \frac{\tau_w \dot{\gamma}_a}{3(\tau_{11} - \tau_{22})}$$ (2.21)

where τ_w is the shear stress at the wall and the first normal stress difference is:

$$\tau_{11} - \tau_{22} = \frac{1}{2}(n+1)\Delta P_{en}$$ (2.22)

where m is the power law coefficient and n is the power law index of the fluid such that:

$$\eta = m\dot{\gamma}_a^{n-1}$$ (2.23)

For a planar contraction, the apparent shear rate ($\dot{\gamma}_a$) is defined as:

$$\dot{\gamma}_a = \frac{8\overline{v}_c}{W_c}$$ (2.24)

and the final expression for the planar extensional viscosity is:

$$\eta_P = \frac{3(n+1)^2 \Delta P_{en}^2}{4m\dot{\gamma}_a^{n+1}}$$ (2.25)

This result is somewhat surprising because it is dependent on the square of the entrance pressure drop and the derivation of this formula is independent of the fluids vortex behavior. Cogswell's analysis assumes inertia is neglected, and that the resulting flow will always behave in a manner in which vortices are generated (Cogswell, 1972). In fact the half angle of convergence (β_0) for a fluid in a planar contraction is determined to be:

$$\beta_0 = \tan^{-1}\left(\frac{3}{2}\left(\frac{\eta}{\eta_P}\right)^{\frac{1}{2}}\right) \qquad (2.26)$$

Based on this formula, for a Newtonian fluid the half-angle of convergence would be 37°. However, for most Newtonian fluids the actual half-angle of convergence is approximately 90°. This result makes Cogswell's method incorrect for any scenario in which vortices are not observed. Despite, its inaccuracies, Cogswell's method is still used frequently and has been proven to be an effective means of calculating extensional viscosities for many fluids (Padmanabhan and Macosko, 1997; Gotsis and Odriozola, 1998; Rajagopalan, 2000).

Cogswell's analysis has been useful in industry due to its relative simplicity, but other means of extensional viscosity calculation have been proposed by Binding and later Gibson, which minimize free energy and accounted for complexities of the flow (Binding, 1988; Gibson, 1989). Binding's method proposed a power-law dependence for the extensional viscosity, and his analysis noted errant assumptions made by Cogswell on the nature of the flow fields (Cogswell's assumptions is based on a strain rate defined by a power-law fluid, however the velocity fields in his calculations are determined for Newtonian fluids) (Binding, 1988). Several authors have performed studies comparing the works of Gibson and Binding with that of Cogswell by numerical simulations and determined these methods are generally of equal accuracy to Cogswell's method, but seldom behave markedly better (Kwag and Vlachopoulos, 1991; Mackay and Astarita, 1997; Rajagopalan, 2000; Zatloukal et al., 2002). Over a large range of strain rates, and especially at high strain rates, Cogswell's analysis is still considered the best means for calculating extensional viscosity (see figure 2-12) (Kwag and Vlachopoulos, 1991; Rajagopalan, 2000).
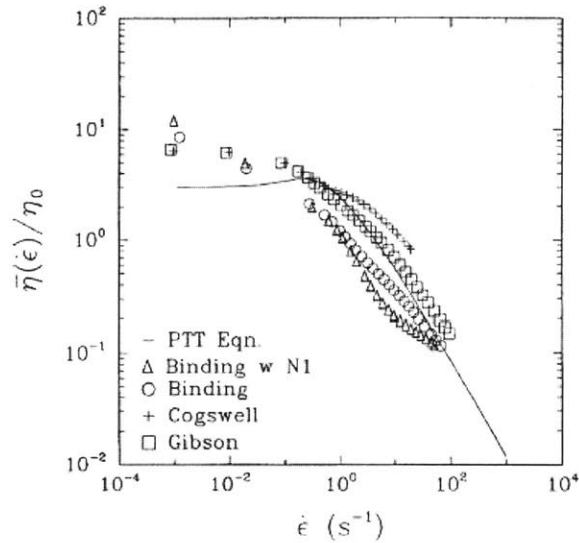
Figure 2-12. Comparison of several techniques for predicted extensional viscosity with data obtained using Phan-Thien-Tanner constitutive model at a strain of 0.5. Results show good agreement with simulations especially at high shear rates (Rajagopalan, 2000).

Mackay and Astaria later looked at the differences between the analyses of Cogswell and Binding and determined the two analyses to be equivalent given the assumption that the velocity is zero at the vortex edge (Mackay and Astarita, 1997). Combining this with other numerical simulations validating its response, lends credibility to using Cogswell's technique for rheological purposes in this paper.

However, it was noted by Rajagopalan that a common criticism of entrance flow is that the extension rate is not necessarily steady, and there is not necessarily a large enough strain in the contraction to reach the steady state, as Cogswell assumed (Rajagopalan, 2000). This may confirm the observations of Padmanhabhan and Macosko whose results agreed with the fiber wind-up results only at strains of 3 (Padmanabhan and Macosko, 1997). The maximum Hencky strain in their 12:1 axisymmetric contractions would be 5 based on the formula for maximum strain (see equation (2.11)).

It is worth noting that the majority of calculations and simulations were performed using axisymmetric contractions, whereas the present study is concerned with planar contractions. Many of the theoretical works in the area were extended to the planar condition, but they have not been validated as extensively as the axisymmetric case

52

(Cogswell, 1972; Binding, 1988; Gibson, 1989). Also, the majority of fluids that have been examined are polymer melts, not solutions. This is only important in the sense that the present study deals with fluids for which the inertial forces cannot be completely neglected. However, the resulting Deborah numbers are similar to those examined in the present study. A summary of all these experiments and simulations dealing with extensional viscosity calculation from entry pressure data is included in table 2-1.

The current study will investigate new regimes of parameter space relative to the magnitude of inertial and elastic stresses. Vortex growth behavior is expected due to the magnitude and behavior of the elasticity number ($El > 1$) in the present study. The techniques for developing the microchannels, quantifying fluid behavior, and observing the fluid motion will now be explored in detail.

Author/Year	Fluids	A/P*	Results
Metzner and Metzner 1970		A	Estimated the pressure drop to be due to only extensional effects. Their analysis is still useful in determining an apparent extensional viscosity and apparent strain rate for entry flow problems.
Cogswell 1972	Polymer Melts	A, P	Using stress balance found correlation for determining extensional viscosity from entry pressure drop in abrupt contractions. Factored in shear components of flow for both planar and uniaxial extension. Determined extensional properties by assuming conical (axisymmetric) and wedge-shaped (planar) entry flow patterns.
Cogswell 1978		A, P	Compared Cogswell technique with other contemporary analyses to determine similarity between all approaches
Binding 1988		A, P	Determined Cogswell's analysis to be incorrect because of inconsistency in the way velocity fields and shear rates were defined. Built on Cogswell's result to balance the total energy in the system. Calculated extensional viscosities, for both uniaxial and planar flows, to be power-law functions of strain rate.
Binding and Walters 1988	Aqueous PAA, Xanthum Solution, Boger Fluid	A	Used Cogswell-Binding to compare entry elongational viscosity with commercial spin line rheometer. Found good correlation for axisymmetric flow, but did not analyze planar contraction flow for Boger fluids. In planar flow, streamlines are not uniformly converging as is assumed in Cogwell's analysis.
Gibson 1989		A, P	Calculated extensional viscosity assuming power-law behavior without assuming entrance angle based on fluid properties. Calculations do not account for varying entry angles with strain rate.
Kwag and Vlachopoulos 1991	LDPE, HDPE	A	Compared Cogswell and Binding analyses with finite element results and determined both only match the slope in extensional viscosities. However, it was determined that Cogswell's technique was acceptable at high stretch rates (>10 1/s)
Mackay and Astarita 1997	LDPE, 0.05% PAA in Maltose Syrup	A	Analyzed the difference between Cogswell's and Binding's techniques and determined them to be the same given several assumptions on the kinematics of the motion. Also determined Cogswell's analysis to be adequate at high strain rates.
Padmanabhan and Macosko 1997	LDPE	A	Compared Cogswell's analysis with Fiber-windup method and determined Cogswell gives good qualitative agreement. Cogswell's analysis was comparable to fiber-windup performed at a strain of 3, even though Hencky strain ϵ = 5.
Gotsis and Odriozola 1998	PP, LDPE, VECTRA, PS	A	Compared results form Binding analysis with that of uniaxial extension. Entry flow results agreed well with uniaxial stretching at an averaged Hencky strain over the entry region.
Binding et al. 1998	PS, PMMA, PP, HDPE, LDPE	A	Used Cogswell-Binding result to determine the extensional viscosity of polymer melts at high pressures by imposing power-law dependence.
Koizumi and Usui 1998	Poly (vinylidene fluoride)	A	Used Cogswell's analysis to determine dependence of elongational properties on PVDF polymer melt.

Binding et al. 1999	Multigrade Oils	A	Used Cogswell-Binding result to analyze multigrade oils. For Newtonian fluids result predicts a Trouton ratio of approximately 5.
Rajagopalan 2000	Phan-Thien-Tanner (PTT) Model	A	Compares Cogswell, Binding, and Gibson predictions with PTT simulations. Cogswell gives good qualitative agreement (as good as all other techniques), and best correlation at high strain rates.
Zatloukal et al. 2002	White-Metzner fluid and LDPE	A	Used modified White-Metzner model to compare accuracy of Cogswell, Binding, and Gibson models for calculating extensional viscosities. Determined that all agreed qualitatively, but quantitatively Cogswell and Binding were less accurate for White-Metzner fluids especially at low strain rates.

Table 2-1. Review of Cogswell's method and its applications (A/P* - axisymmetric or planar)

3 Testing Procedure

3.1 Fabrication

Microchannels were fabricated using the soft lithography techniques pioneered in the laboratories of George Whitesides for fabrication of PDMS microchannels (Duffy et al., 1998; Xia and Whitesides, 1998; McDonald et al., 2000). In this technique a mold, from which multiple PDMS channels may be produced, is fabricated using lithography. The entire process (from concept to channel) can be accurately completed (features as small as 1 μm, fabricated to within 10 % of nominal dimensions) in approximately 48 hours; hence the label rapid-prototyping has been linked with this fabrication method. Despite its simplicity this method is still the most effective way to generate microchannels with relatively high vertical walls (depths greater than 10 microns, with tapering less than 5°). The entire fabrication process used in the present study is outlined in figure 3-1.
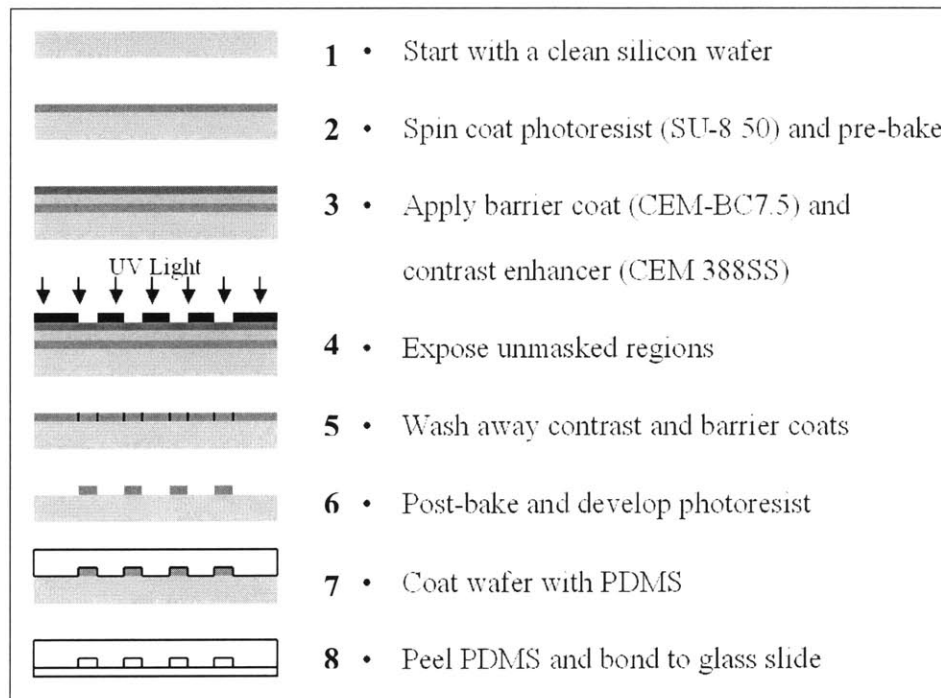
Figure 3-1. Fabrication process used in the present study

1 • Start with a clean silicon wafer

2 • Spin coat photoresist (SU-8 50) and pre-bake

3 • Apply barrier coat (CEM-BC7.5) and contrast enhancer (CEM 388SS)

4 • Expose unmasked regions

5 • Wash away contrast and barrier coats

6 • Post-bake and develop photoresist

7 • Coat wafer with PDMS

8 • Peel PDMS and bond to glass slide

3.1.1 Mold Fabrication

The first portion of the process (steps 1-6) must be done in a cleanroom to ensure that no particles can corrupt the channels. Molds were fabricated for the microchannels in the current study at MIT's Exploratory Materials Laboratory (EML), which is a subsidiary of the Microsystems Technology Laboratories (MTL). The EML is a class 1000 cleanroom, which means there are fewer than 1000 particles larger than 0.5-micron diameter per 100 cubic feet.

The process begins with a clean silicon wafer: 3-inch p-type boron-doped wafers were used in this study for economical reasons (Silicon Quest International) (step 1). The type and size of the wafer are not important to the process, but silicon is required for the clean room and works best as a base for the photoresist. The wafer is spin coated with SU-8 50 (Microchem) to achieve a uniform thickness of 50 microns (step 2). SU-8 is a brand of negative photoresists, which are well suited for microfabrication in which high-aspect ratios are required. The wafer is next soft-baked to cure the SU-8. Next two additional layers are spin-coated onto the wafer, which are required to generate vertical sidewalls. A barrier coat (Shin-Etsu MicroSi, Inc: CEM BC 7.5) is spun on top of the SU-8 and a contrast enhancer (CEM 388SS) is spun on top of the barrier coat (step 3). A chrome mask with the inverse of the desired features (channels are transparent, everything else is opaque) is placed over the wafer, and the wafer is then exposed to collimated UV light (step 4). The areas of the wafer that are exposed to the light are chemically cross-linked. The wafer is next hard baked to further solidify areas of SU-8 that were exposed. The contrast enhancer and barrier coat are removed using deionized water (step 5). Finally, the unexposed regions of photoresist are dissolved from the wafer using an SU-8 developer (step 6). The resulting product is a silicon wafer with towers of SU-8 that are the inverse of the desired microchannels.

Several aspects of this technique are altered from the original model set forth by Duffy and Whitesides (Duffy et al., 1998; Xia and Whitesides, 1998). The most notable change is the use of the contrast enhancer and barrier coat. In many microfluidics applications,

corners are rounded and walls are tapered, without many consequences on the final product. However, when performing rheological measurements, it is imperative to minimize surface roughness and achieve vertical sidewalls. As UV sources age, the light drifts away from perfect collimation and additional wavelengths can be transmitted. The contrast enhancer recollimates the light by blocking out non-perpendicular light; as a result, UV exposure times increase by a factor of two. The barrier coat is immiscible with both the SU-8 and contrast enhancer and prevents the two layers from dissolving into one another. Figure 3-2 shows the difference between a mold generated using a barrier coat to collimate the light and a mold fabricated without a barrier coat.
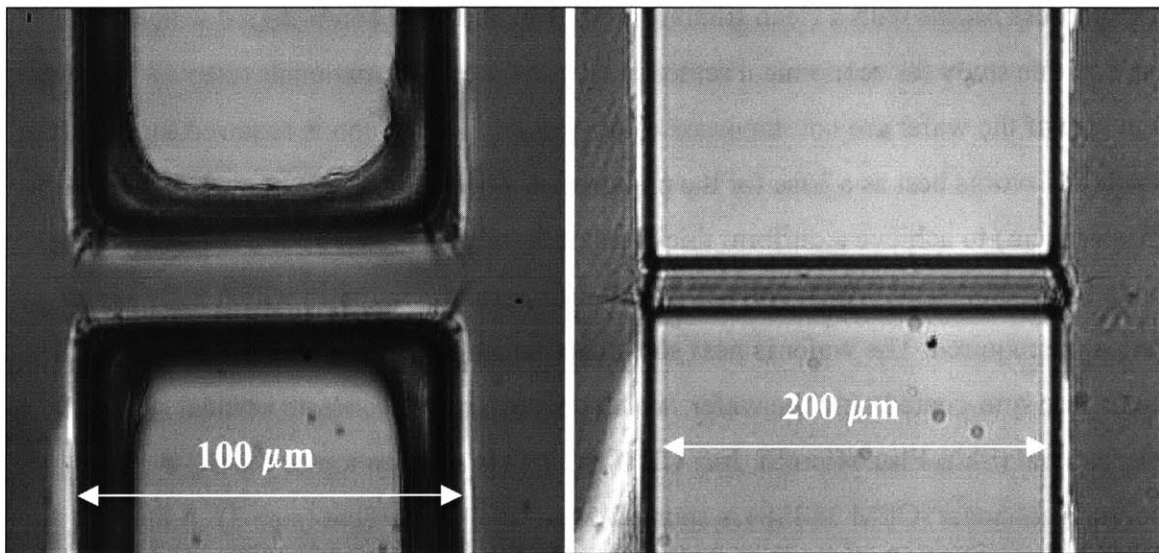
Figure 3-2. SU-8 Mold without contrast enhancer (left) compared with mold using contrast enhancer (right)

Another variation from the standard method is to use a chrome mask. It is also possible to generate molds using a high-resolution (2540 dpi) transparency. However, at this resolution features are only accurate to approximately 5 microns. Again, because rheological measurements require precise geometries, it is necessary to achieve the maximum resolution possible. Using these transparency masks, waviness was apparent in the molds and resulting microchannels. It is especially important to minimize the radius of curvature at the corners of the entry and exit of the contractions, as this can greatly affect entrance behavior (Evans and Walters, 1986; Evans and Walters, 1989). The resolution of the chrome mask is below 1 micron and features as small as 10 microns can

be generated. The differences between molds made using a transparency and chrome mask is illustrated in figure 3-3.
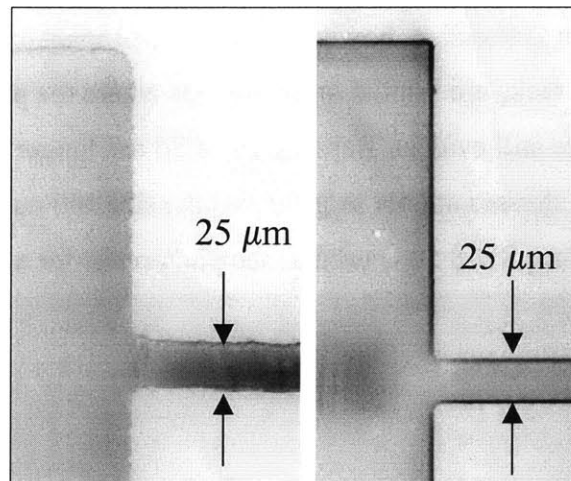
Figure 3-3. Comparison of the SU-8 mold from a transparency mask (left) and a chrome mask (right). Both were generated using the contrast enhancer.

Using photoresist, as opposed to etching into the wafers, was preferred because vertical sidewalls were desired. Using silicon wafers restricts the shapes of the channels because silicon can only be etched at defined angles based on the type of wafer (doping and crystallographic orientation) (Qu et al., 2000). Vertical sidewalls can be generated in silicon, but only at laborious extents (Dwivedi et al., 2000). Silicon channels are also more expensive and time-consuming process than building channels upward. Conversely, SU-8 is able to generate high aspect ratios ($h/W \sim 10$) and vertical walls (tapered angle, $\alpha \sim 89°$) (see section 3.3). Cross-linked SU-8 is also physically stiff (Young's Modulus, $E = 4.02 - 4.25$ GPa), making the molds able to withstand small forces, such as the ones that will be generated in forming the PDMS channels (Lorenz et al., 1997; Tay et al., 2001). However SU-8 is also brittle, so larger forces can cause the cross-linked photoresist towers to be sheared off of the silicon wafer.

Originally SU-8 2050 was to be used rather than SU-8 50, and for most applications the 2000 series is preferred (Shaw et al., 2003). The SU-8 2000 series has faster baking times and fewer impurities, minimizing the formation of bubbles on the surface of wafers. However, because a contrast enhancer is being used in the fabrication process, the baking processes generate thermal stresses on the surface of the SU-8. The stresses are generated

by the mismatch in the thermal conductivities of the three layers (the contrast enhancer, the barrier coat, and the SU-8). The surface thermal stresses generate cracks in the contrast enhancer, which is standard, however the cracks propagate and are evident in the SU-8 (see figure 3-4). Cracks are limited in the regions where the photoresist has been cross-linked, but they are still evident. Because SU-8 50 has longer baking times than SU-8 2050, the thermal stresses are not as great and the size and number of cracks is significantly reduced. Thus SU-8 50 is used as the photoresist for all of the molds.
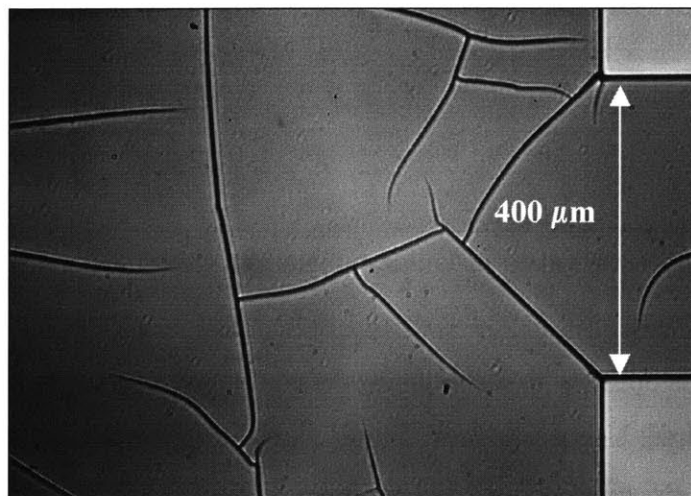
Figure 3-4. Image of cracks in SU-8 2050 mold

The cracks generated from the baking processes were originally a concern. These cracks propagate from areas where sharp corners are desired in the channels. However, SEM (scanning electron microscope) images (figure 3-5) of the resulting PDMS microchannels from these molds indicate that the size of the cracks (~ 1 μm) is modest in comparison to the size of other features in the geometries. The SEM images also have finer cracks, which do not appear on the molds or on any replications of the PDMS (figure 3-5). These cracks were in the surface of the gold coating on the surface of the PDMS. Gold has been sputter deposited (~ 1 nm) on the surface of the PDMS so as to allow PDMS to generate secondary electrons when impeded on by an incident beam from the electron gun within the SEM. A sensor in the SEM collects these secondary electrons, and these electrons collectively generate the image of the sample. Because the PDMS cast devices are elastic and the gold forms only a small layer on the surface, cracks form easily when handling the channels. However, the channels that were used for SEM imaging cannot be bonded

and are, therefore, not used for any measurements or flow visualization. These cracks do not exist on the bonded channels.
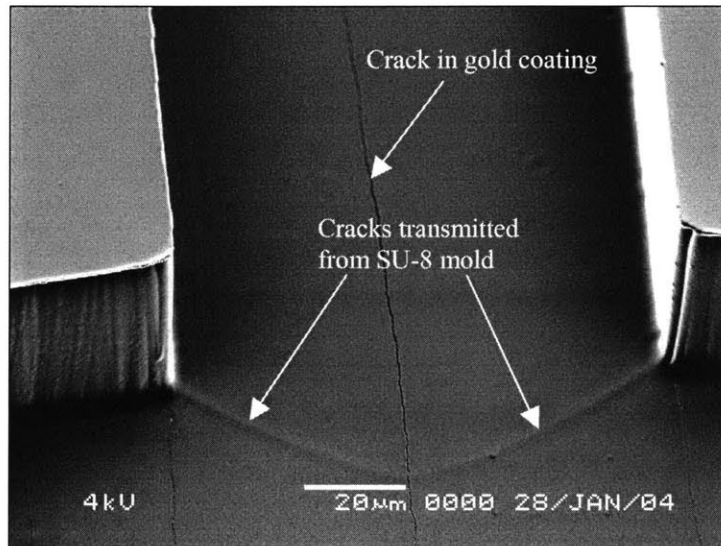
Figure 3-5. SEM image of PDMS channels and the cracks generated in the SU-8 baking processes

From figures 3-5 and 3-6, it is also possible to see ridges on the wall surfaces. These ridges are results of the photolithography process and are common in microchannels generated using the present technique (Duffy et al., 1998). However, they are small (approximately 10 μm in periodicity and 0.5 μm in amplitude) and not visible from vertical views. Mask quality also aids in reducing the size of these ridges. From figures 3-5 and 3-6 it is also possible to see the quality of the channels. They are nearly vertical ($87° < \alpha < 93°$) even for the smallest features (see section 3.3 for calculation). There is a small amount of tapering at the bottom of the channel, however this is small (10% of channel) and is indistinguishable in larger channels.
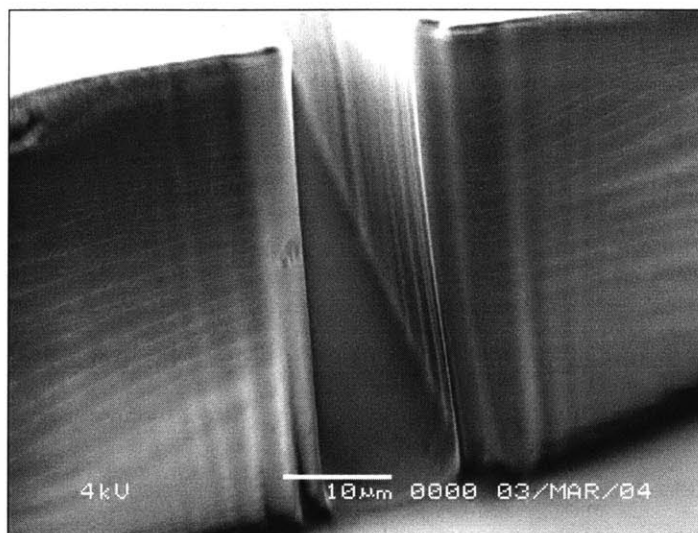
Figure 3-6. Entry of 160:10 μm channel

3.1.2 PDMS Channels

From each SU-8 mold, it is possible to repeatedly generate (approximately 20 times without noticeable degradation) PDMS microchannels without using a clean room (steps 7 and 8 in figure 3-1). First a thin layer (~ 10 nm) of tridecafluoro-1,1,2,2-tetrahydrooctyl-1-trichlosilane (United Chemical Technologies) is vapor deposited on the surface of the SU-8 mold. This chemical increases the contact angle of the PDMS on the silicon and SU-8, and the hydrophobicity of the mold facilitates the removal of the PDMS. Next a 10:1 mixture of PDMS and curing agent (Dow Corning: Sylgard 184) is degassed and poured over the mold (step 7). When pouring the PDMS over the mold, the hydrophobic nature of the silicon prevents PDMS from wetting many of the sharper geometries. To eliminate the resulting bubbles, it is necessary to vacuum the mold for several minutes until bubbles detach from the mold surface. Bubbles remaining at the PDMS surface are inconsequential to the geometry and generally disappear during the curing process. The PDMS is then cured at 80°C for approximately 25 minutes. The PDMS is then removed from the mold, and holes are punched as access ports for the inlets, outlets, and pressure ports. The holes are punched using a blunt syringe tip (BD Luer Stub Adapter 20 gauge: 0.61 mm ID, 0.91 mm OD). The syringe tip generates a high stress on the PDMS so that when the PDMS relaxes, a clean 400 μm diameter hole

has been formed. It is advantageous to punch the holes from channel side of the PDMS because inserting the syringe tip is a cleaner process then the exit. The tip can tear the PDMS when exiting, but this is unlikely when entering the surface. The PDMS channels and a microscope slide are cleaned using isopropanol, placed in a plasma asher, and exposed to gaseous plasma (air works best). The asher cleans the organic materials from the PDMS and glass, modifying surface properties so that the PDMS and the slide form an irreversible covalent bond upon contact (step 8).

PDMS is a practical material for the production of these microchannels based on its material properties and the ease of fabrication. It is liquid impermeable, but unlike silicon it is gas permeable. PDMS is an elastic polymer, so it is flexible and durable. This works well for low viscosity fluids, however as the fluid viscosity increases, pressures increase and deformation of the channel walls can be observed at higher flow rates. Stiffer polymers, such as polyurethane, would likely be a better option for systems with more viscous working fluids. The optical transparency of PDMS is critical for flow visualization and PIV measurements. The optical transparency of polyurethane is not as high as PDMS. Polyurethane also has longer curing times and has not been as widely accepted as PDMS for microfluidic applications. Because of these material properties PDMS is advantageous to silicon microchannels and other elastomers.

The problems with using PDMS are based on the difficult surface properties of the elastomer. PDMS has reportedly varying surface properties, namely the contact angle of the fluid is found to change over time (Hillborg et al., 2000). PDMS is hydrophobic, so frequently it is difficult to wet many portions of the channel and bubbles will form at salient corners. However, because PDMS is gas permeable, air bubbles slowly disappear as the air permeates through the channel walls. These surface properties also enable particles to frequently stick to the surfaces. Typically in flow visualization experiments, the fluorescent particles stick to the walls of the channels especially at sharp contractions. This however, may be due to the ridges that originated from the lithography process, which are observed in figures 3-5 and 3-6.

3.2 Experimental Setup

Once the channels have been bonded, several different experimental techniques are employed to quantify the flow properties of the microrheometry channels. For each setup, 22 gage (0.41 mm ID, 0.71 mm OD) stainless steel tubes (McMaster-Carr) are used to interconnect the microchannels to external Tygon® plastic tubes (ID 0.7 mm, OD 2.4 mm – Norton Performance Plastics) at the inlets, outlets, and pressure sensors. The PDMS hole is smaller than the outer diameter of the tubes, and therefore stretches and conforms around the stainless steel tube to form a leak-proof seal. For this setup the inlet tube is connected to a syringe, and a syringe pump (Harvard Apparatus – 11 Plus series) generates a constant flow rate for the entering fluid. The syringe pump operates on a stepper motor that moves the syringe shaft at a constant velocity. Thus to ensure that the times between steps on the motor is small enough to have a negligible effect on the flow rate in the channels a minimum velocity must be achieved. To combat this deficiency we have utilized a range of syringes with different volumes (500 µl, 1 ml, 3 ml), so the range of achievable flow rates spans several decades (0.1–15 ml/hr).

3.2.1 Pressure Measurement

Honeywell pressure sensors (26PC, differential model) were used to determine the pressure loss in the channels. Liquid was allowed to flow through the channel to the pressure tap locations and tubing was connected to the pressure tap once bleeding began. After the tubing also began to bleed, it was connected to the pressure port on the pressure sensor. This was done for two pressure tap locations in the microchannel. The microchannels were designed to measure a pressure drop across a contraction at pressure ports 3 mm upstream of the contraction and 3 mm downstream from the expansion. This is a minimum of 60 diameters away from the contraction and expansion to ensure that the pressure sensors do not interfere with the flow patterns.

Model	Maximum Presure (kPa)	Sensitivity (mV/kPa)	Resolution (mV)	Maximum Voltage (mV)	Overpressure (kPa)
26PCB	35	1.45	0.02	50	138
26PCC	100	0.97	0.03	100	310
26PCD	200	0.48	0.03	100	413

Table 3-1. Summary of pressure sensors specifications

The pressure sensors measure a differential pressure across the contraction as shown in figure 3-7. The pressure sensors consist of encasing around a piezoresistive sensor die, which outputs a voltage proportional to the pressure difference between the two ports. The voltage from the sensor is read by a data acquisition (DAQ) card (National Instruments: PCI-MIO-16XE-50). The card works with a LabVIEW program to appropriately amplify, read, and analyze the signal from the sensor. Another channel on the DAQ is also used to supply the voltage to power the sensor. The LabVIEW program allows the user to specify the voltage range over which the output from the sensor would be read. The signal is amplified appropriately to accommodate this voltage range and then translated within the program to the actual sensor value. One of three different pressure sensors were employed based on expected pressure drop with measurable pressure ranges of from zero to 35, 100, and 200 kPa.
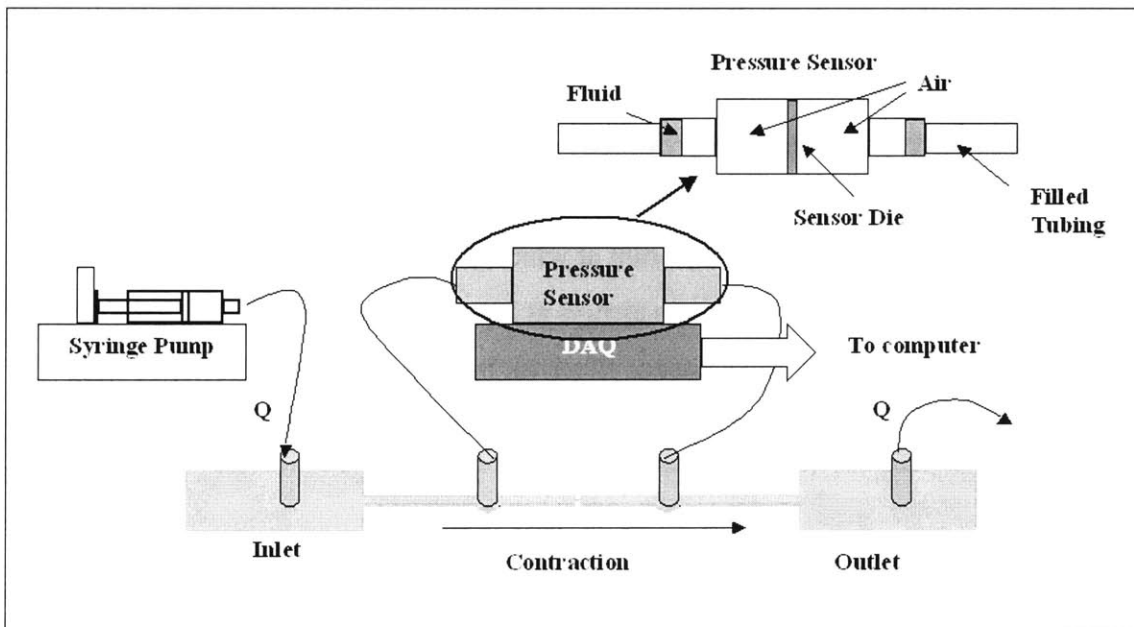
Figure 3-7. Setup of pressure measurement system

After tests have been run, the pressure sensors are calibrated using a column of water of a desired height. The measured voltage is correlated with the resulting known pressure (P = $\rho g H$, where g is the gravity, and H is the height of the column) as shown in figure 3-8.
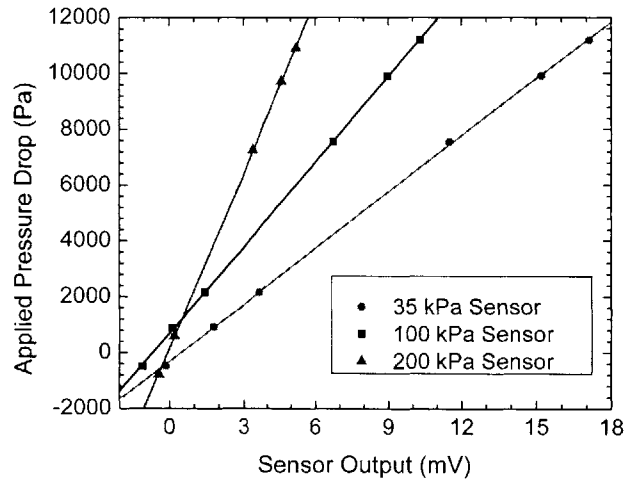
Figure 3-8. Plot of the calibration curves used for the three different pressure sensors

For the pressure measurements a lag exists between specifying the control rate and the pressure reaching its steady-state value. The time delay has been observed in pressure measurements of visco-elastic fluids (Yesilata et al., 2000). This lag is approximately 1 minute using water and at a flow rate of 1 ml/hr (see figure 3-9). However, increasing the flow rate decreases the magnitude of the lag. The fluid's viscosity has the opposite effect, causing lag to increase as has been previously observed (Yesilata et al., 2000). For most fluids the pressure data was taken over 5 minutes sampling at a rate of 20 Hz. The resulting data was averaged from the point at which the voltage reading leveled off and for the remainder of the time. This was always at least 100 seconds of data (2000 data points) (see figure 3-10). For this reason, all streak images were also performed after waiting for several minutes for flow patterns to stabilize and flow rates to reach specified values.
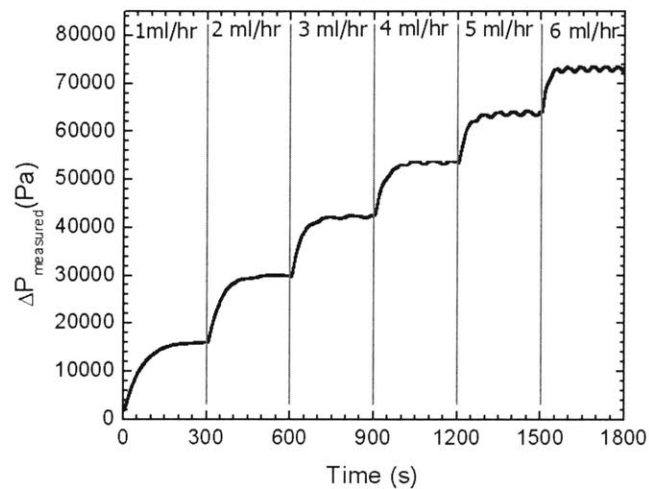
Figure 3-9. Pressure increase with time for increasing flow rates (0 ml/hr - 6 ml/hr). Flow rates are increased 1 ml/hr every 5 minutes. Data is taken using a Newtonian 55% glycerol and water mixture (η_0 = 8.59 mPa-s) in a 400:25 μm contraction. Time lag is on the on the order of 5 minutes at the lowest flow rates, but decreases as flow rate increases.
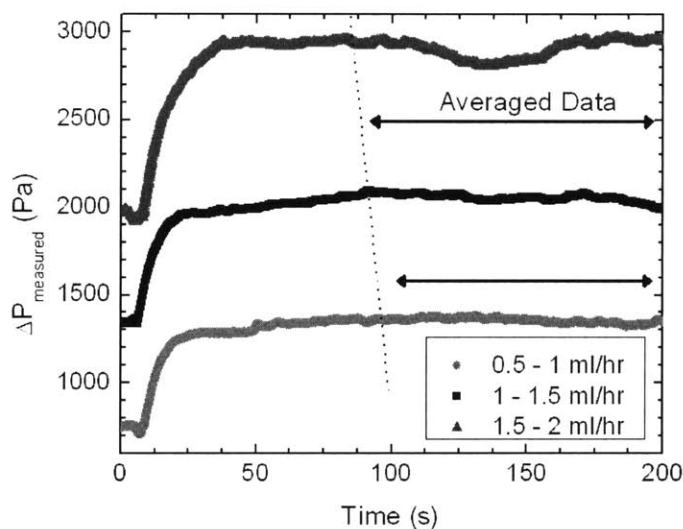
Figure 3-10. Figure shows lag times for the 0.1% polyethylene oxide solution at increasing flow rates. This figure shows the time range over which pressure measurements are averaged.

The lag is likely due to several factors. First, as the pressure sensor takes data, fluid is not directly touching the sensor die. Instead, air is trapped between the fluid in the pressure tubing and the pressure die. The pressure reading is equivalent to the pressure in the air. Thus the air must be compressed to equal the pressure in the channel. Thus a pressure

gradient is generated and the delay is caused by the amount of time is required for the liquid to compress the air to steady state in both the upstream and downstream pressure tap. However, decreasing the amount of air in the pressure ports seemed to do little to decrease the timescale of this delay. Another source of time lag is due to the elasticity of the various components of the setup. The tubing and PDMS both have elasticity, so increasing the flow rate results in increased pressure and as a result expansion of these elastic materials. As steady state is reached, the tubing and PDMS recede to an undeformed state. The last possible source of time delay is due to the speed of visco-elastic pressure waves (c_{ve}) (Kazakia and Rivlin, 1981; Yoo and Joseph, 1985):

$$c_{ve} = \left(\frac{\eta_0}{\lambda\rho}\right)^{\frac{1}{2}}$$

(3.1)

This velocity is small (~10 cm/s) but because tubing lengths are small (~20 cm) this would not account for the large time delays.

3.2.2 Video and streak imaging

Video and streak images were taken using a Zeiss microscope and attached cameras. The microscope used an air objective at a ten times magnifications. For this lens the numerical aperture is 0.25 and the associated field of depth is 38 microns. Because the depth of the channels is 50 μm, the resulting images capture most of the total channel depth. The fluid was seeded with fluorescent particles (1.1 μm diameter: 7-FN-1000 - Interfacial Dynamics Corporation) at 0.02 wt%. These particles are small enough that they do not affect the bulk motion of the fluid. The fluorescent particles are illuminated by an ion-Argon laser, at a wavelength of 532 nm. The particles are excited in this range and emit light at a wavelength of 580 nm. Optical band pass filters are used to eliminate all light outside 580 nm.

For channels to be used in any imaging processes the holes for the pressure taps were not punched in channels; otherwise the setup was the same as for the pressure measurements. Video clips were taken using a CCD (charge-coupled device) camera (Pulnix TM-200). Images are obtained at 29.97 frames per second and they are recorded to a digital video

(DV) cassette. Resulting video is stored at images sizes of 768 by 494 pixels. Digital videocassettes are converted to audio video interleaved (AVI) format, and final video resolution is 0.98 μm/pixel. CCD exposure times vary between 0.001 and 0.016 seconds, however for sufficient lighting, the maximum exposure time (0.016 s) was employed. Attempts at obtaining high-speed video (using Phantom V5.0 Camera) of flows failed due to insufficient optical attachments and lighting.

The still images were taken using an Apogee Instruments CCD camera (KX32ME) (image size: 2184 by 1472 pixels). In many previous experiments, streak images took as long as several minutes of exposure time to obtain (Evans and Walters, 1986). However, it took much less time (~ 10 ms) in this study because fluid velocities are higher ($\bar{v}$ ~ 10 cm/s) and the field of view is smaller (~ 500 μm). Exposure times varied between 0.01 and 0.03 seconds for the streaked images in the present study (see section 5.1). The images obtained were saved in the tagged image file format (TIF) at a resolution of 0.7 μm/pixel.

3.3 Geometry

The dimensions chosen for these experiments were determined based on the limitations of the chrome mask and the lithography process. The mask was limited to a resolution of 1 μm, thus, to ensure that the corners of the geometry were in fact right angles, the contraction width (W_c) was chosen as 25 μm. To compare these results with previous works in planar geometries, the contraction ratio (β) was designed as 16 to 1. (Evans and Walters, 1986; Nigen and Walters, 2002). At this ratio, the Hencky strain is the same as a 4:1 contraction in the axisymmetric case, so the elastic effects were to be compared with axisymmetric experiments on 4:1 contractions (Cable and Boger, 1978; 1978; 1979; Rothstein and McKinley, 1998). Also, the smallest feature specified for the chrome mask (Advance Reproduction Corporation)was 10 μm. Thus, another of geometries was fabricated with the contraction width, W_c = 10 μm, and the larger dimension was W_l = 160 μm to maintain the 16:1 contraction ratio. For each of these 16:1 contractions the length of the contractions (L_c) varied between L_c = 50 μm and L_c = 400 μm.

A third set of contractions were fabricated at a contraction ratio of $\beta_P = 4$. For one channel the contraction width was designed as $W_c = 50$ μm while for the second channel the contraction width was $W_c = 12.5$ μm. For these channels goal was to compare streak patterns with planar 4:1 contractions that Evans and Walters and Quinzani (Evans and Walters, 1986; Evans and Walters, 1989; Quinzani et al., 1995). However, the contraction length was only designed as $L_c = 200$ μm. Because it is unclear whether a 4:1 contraction ratio is large enough to neglect the effects of the wider channel (W_I), there was no intent to employ Cogswell's analysis to determine extensional viscosities for these contractions.

Once the channels are fabricated there were a number of methods employed to ensure that nominal dimensions were upheld in the final channels. In early attempts at fabrication (using a transparency mask and without employing the contrast enhancer) the final microchannels were not as specified in the initial drawings. Channels were significantly tapered ($\alpha \sim 70°$), and the base dimensions were oversized (as much as 15 μm). These errors were due to the poor collimation of the UV source and the mask. However, after resolving these issues, there was still concern with accurately measuring the lengthscales of final channels. A calibrated microscope was used to measure each of the relevant dimensions in the PDMS replicas. In the finalized channels nearly all of the features were within 5% of their designed sizes (figure 3-11). The only exception was the $W_c = 10$ μm contractions. These were consistently oversized by approximately 2 μm.

Channel		Designed (μm)			Measured (μm)		
		Wc	Lc	W1	Wc	Lc	W1
Chip A	Channel 1	25	50	400	23.52	49.06	394.43
	Channel 2	25	100	400	25.05	100.21	393.25
	Channel 3	25	200	400	24.01	199.37	393.05
	Channel 4	25	400	400	24.33	397.29	392.81
Chip B	Channel 1	10	50	160	11.99	49.39	160.31
	Channel 2	10	100	160	13.00	99.73	161.18
	Channel 3	10	200	160	12.48	198.96	158.64
	Channel 4	10	400	160	12.36	396.78	160.28
Chip C	Channel 1	50	200	200	50.34	198.33	198.55
	Channel 2	12.5	200	50	12.15	196.53	49.38

Table 3-2. Measured dimensions compared with specified dimensions
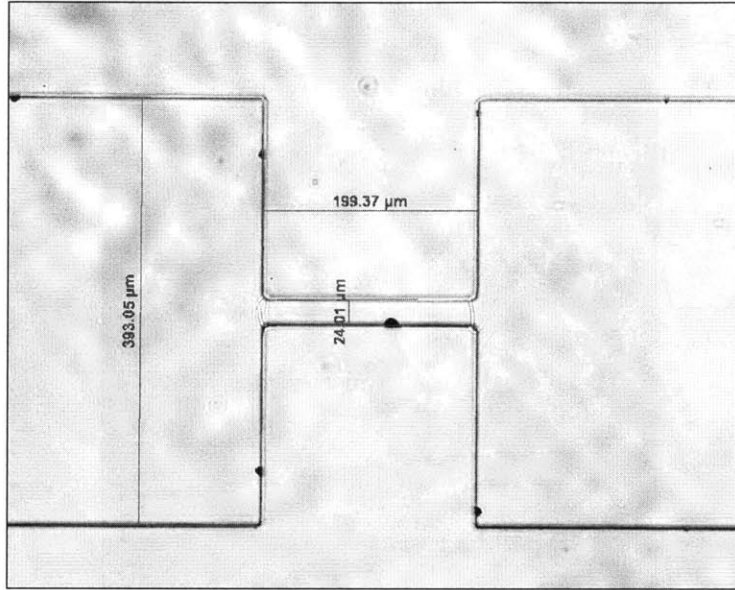
Figure 3-11. Sample PDMS channel for length measurement: nominally a 400:25 μm contraction, measured values are within 5% of the designed dimensions

Using a microscope is only accurate in measuring distances in plane. Thus to measure the height of the channel, another technique was required. The spin coating process has been highly refined, but it is still difficult to control heights to within 5% (Lorenz et al., 1997; Shaw et al., 2003). For this project all the channels were to be taken off one single wafer of uniform depth. So it was imperative that an accurate reading of the depth throughout the channel was established. Most methods of non-invasive depth measurement are typically not more viable than the 5% accuracy of the spin coating process, so a more robust approach was taken. Because only one mold was employed, it is known that each set of channels is identical. Thus one set of PDMS channels that were pulled off the master mold was sliced thinly at a specified channel location (see figure 3-12). The cross-section of the channel was placed sideways under the microscope and the lengths were measured in the same fashion as the other distances. This was performed at several different locations throughout the mold. At each location the depth was constant to within 2% of 50 μm. These same images were also used to determine the tapered angle (α) of the channels. For each channel the tapered angle was always within 3° of $\alpha = 90°$, the desired right angle.
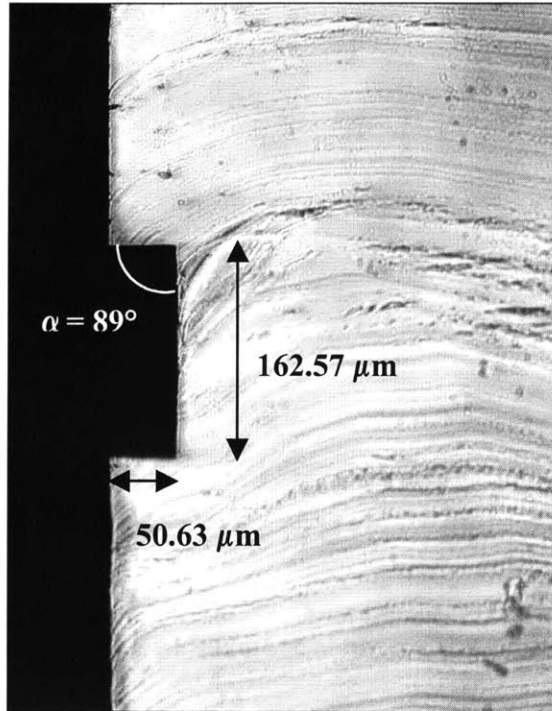
Figure 3-12. Cross section of 160 μm channel, used for measuring channel depth

SEM images were initially employed to measure lengthscales for the channels. However, these measurements were less accurate than those obtained by optical microscopy. The SEM images are able to zoom in closer and observe the channel roughness and three-dimensional features that can only be viewed from an oblique angle. So SEM images were taken of the channels, but primarily for qualitative means.

With channels fabricated very close to designed specifications and a pressure measurement setup, it is now possible to measure extensional properties fluids as set forth in the project motivation. However, it is first necessary to quantify the rheological properties of the fluids to be examined in this study.

4 Fluid Rheology

4.1 Fluid Selection

4.1.1 Polymer architecture

The dynamics of polymers in a solution is greatly influenced by the concentration relative to the critical overlap concentration (c^*). The overlap concentration is the point at which polymer molecules begin interacting. At concentrations much less than c^*, the fluid is considered dilute and the polymer chains each behave as if they are independent in the solvent. As the concentration increases ($c \sim c^*$), molecules begin overlapping in the semi-dilute range. In concentrated solutions ($c \gg c^*$) the polymer chain interactions strongly influence the behavior of the fluid. The critical concentration for polymer solutions is dependent on the properties of both the polymer and the solvent (see figure 4-1). The critical concentration can be determined based on the properties of the fluid-polymer interaction and statistical probabilities of polymers interacting.
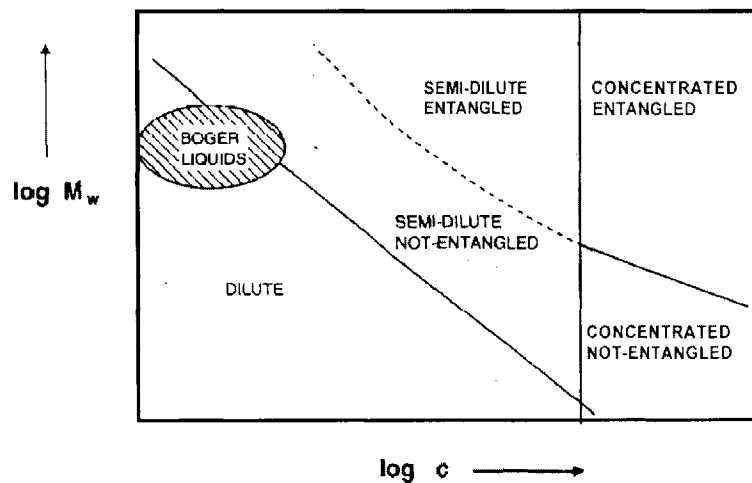
Figure 4-1. Molecular weight plotted against concentration. This figure shows the different solvent regimes based on various polymer concentrations and molecular weights. Adopted from (Dontula et al., 1998).

The critical concentration is the concentration at which the volume of the polymer coils is equal to the total volume of the fluid, thus molecules must interact in with one another. The critical concentration for a polymer solution can be approximately calculated using the formula:

$$c^* \approx \frac{M_w}{N_A \langle r^2 \rangle^{\frac{3}{2}}}$$

(4.1)

where M_w is the molecular weight, N_A is Avagadro's number, and $\langle r^2 \rangle$ is the mean square of the radius of the coiled polymer chain. Statistical probability suggests that the most likely shape for a polymer in solution is in the form of a sphere. This radius is a statistical probability determined from the random walk of the polymer. The radius of the polymer sphere can be related to the number of monomer chains in the polymer and its interaction with the surrounding fluid (McKinley and Armstrong, 2000).

$$c^* \approx \frac{M_w}{N_A \left(\alpha_s C_\infty n_m l^2 \right)^{\frac{3}{2}}}$$

(4.2)

where α_s is the swelling ratio, which is the affinity of the polymer for its solvent, C_∞ is the characteristic ratio of the polymer, indicating how freely the monomer is to rotate back upon itself, l is the average bond length, and n_m is the total number of bonds:

$$n_m = \frac{j M_w}{m_0}$$

(4.3)

where m_0 is the molecular weight of one monomer and j is a coefficient is derived from the number of bonds of length l, in each molecule. Combining this formula, with equation (4.2) it is clear that c^* decreases with increasing molecular weight ($c^* \sim M_w^{-0.5}$). This trend is illustrated in figure 4-1. Equation (4.2) serves as a basis for determining the critical concentration, however, it uses a statistical approximation of the radius, which means it is only an approximate calculation of the overlap concentration.

Each of these variables is documented for most polymer solutions in the Polymer Handbook (Brandrup et al., 1975), with the exception of the swelling ratio, which is dependent on the polymer interaction with the solvent. This variable can be calculated through the formula:

$$\alpha_s = \left[\frac{\zeta(3v)}{\zeta\left(\frac{3}{2}\right)}\right]^{\frac{1}{2}} N^{v-\frac{1}{2}} = \left[\frac{\zeta(3v)}{\zeta\left(\frac{3}{2}\right)}\right]^{\frac{1}{2}} \left(\frac{0.666 n_m}{C_\infty}\right)^{v-\frac{1}{2}} \qquad (4.4)$$

where ζ is the Reimann zeta function, N is the number of Kuhn steps (the number of freely rotating rods), and v is the solvent quality exponent determined from tabulated calculations of intrinsic viscosity measurements for the polymer in a given solution ($a = 3v-1$) (McKinley, 2002). Thus the final value of c^* can be written as:

$$c^* \approx \frac{M_w}{N_A \left(\left[\frac{\zeta(3v)}{\zeta\left(\frac{3}{2}\right)}\right]^{\frac{1}{2}} \left(\frac{0.666 n_m}{C_\infty}\right)^{v-\frac{1}{2}} C_\infty n_m l^2\right)^{\frac{3}{2}}} \qquad (4.5)$$

The finite extensibility (L_e^2) of a solution is a ratio of the maximum length of a polymer compared with a characteristic length of the polymer for a given solvent. By convention the characteristic length of the polymer is one-third the mean squared radius such that the finite extensibility is calculated as (McKinley, 2002):

$$L_e^2 = \frac{3 R_{max}^2}{r^2} = 3 \left(\frac{0.666 n_m}{C_\infty}\right)^{2(1-v)} \qquad (4.6)$$

4.1.2 Working Fluids

The purpose of using a microfluidic device to examine flows was to take advantage of the ability to generate large shear and extension rates while maintaining low Reynolds numbers. The behavior of mobile non-Newtonian fluids in microchannels was particularly of interest. Non-Newtonian fluids are characterized by complex microstructure while maintaining a homogenous appearance on the macroscale. Specifically, fluids with elastic properties were of interest, in order to generate Deborah numbers above unity (as defined in equation (2.1)).

At Deborah numbers greater than unity, elastic effects typically become important in the flow. Because strain rates are so large on the microscale, generating high Deborah numbers in this system requires only small relaxation times (~ 1 ms). The ability to obtain Deborah numbers above unity for fluids with low relaxation times makes it possible to study the non-Newtonian properties of mobile liquids (η < 10 mPa·s). However, the goal was to still keep the Reynolds number relatively small (equation (2.3)) in order to minimize inertial effects relative to elastic effects. At low viscosities, it is difficult to neglect inertial effects. Thus, while the Reynolds numbers remain small, they do exceed unity for many experiments performed.

It was also desired to keep the viscosity of the fluid approximately constant. For constant viscosity fluids, the Reynolds number is linearly related to the flow rate. In non-Newtonian fluids, the shear viscosity typically decreases as the shear rate increases. For this system there are very large shear rates at the walls, and previous studies have shown that strongly shear-thinning viscoelastic fluids show vortex growth in planar geometries (Evans and Walters, 1986; Evans and Walters, 1989). The present study was intended to investigate the behavior of constant viscosity fluids in similar geometries. Previous studies have examined such constant viscosity fluids in planar geometries previously but were unable to observe any vortex behavior (Walters and Rawlinson, 1982; Evans and Walters, 1986; Evans and Walters, 1989).

Boger fluids are fluids with substantial elastic properties, but constant shear viscosities. These fluids are, therefore, ideal for many rheological applications where elastic properties are to be examined, but viscous and inertial effects are intended to be invariant. These fluids are generally formed by dissolving small amounts of high molecular weight polymer in a high viscosity solvent (see figure 4-1).

For a dilute solution, the viscosity is a linear function of the concentration:

$$\eta_0 = \eta_s \left(1 + [\eta]c + O(c^2) \right) \tag{4.7}$$

where $[\eta]$ is the intrinsic viscosity (see section 4.3.1). By using water as the base solvent and relatively low concentrations of polymer, it is possible to generate a low viscosity solution that also exhibits significant elastic properties.

Zimm theory predicts the relaxation time associated with a dilute polymer solution (see section 4.3.1). The theory predicts that the relaxation time is linearly related to the molecular weight of the polymer and the solvent viscosity:

$$\lambda_z \sim \eta_s M_w \tag{4.8}$$

To obtain substantial relaxation times (> 0.1 ms), fairly large polymer molecular weights are required. However, by using water as the base solvent, relaxation times are measurable and viscosities remain small. For these solutions it is required that large shear rates (> 1000 s^{-1}) be used to measure rheological properties, which is very difficult to obtain without the influence of inertial forces. For this reason a microfluidic device is necessary for characterizing these fluids.

The base fluid for all these experiments was a low viscosity Newtonian fluid (either deionized (DI) water or a mixture of DI water and glycerol). The polymer used was polyethylene oxide (PEO) (Sigma Aldrich) with a molecular weight of $M_w = 2,000,000$ g/mol. PEO was used for its high molecular weight, water solubility, and mechanical properties. PEO is a flexible polymer, which lends itself to highly elastic behavior even at low concentrations. Because of these properties, this fluid has been used in several previous studies where similar fluids were desired (Dontula et al., 1998; Mun et al., 1998; Tirtaatmadja et al., 2004). In the present study PEO was mixed at concentrations of 500 ppm (0.05% weight), 1000 ppm (0.1%), and 3000 ppm (0.3%).

For PEO, each monomer has the chemical formula C_2H_4O ($m_0 = 44$ g/mol). At a molecular weight of 2,000,000 g/mol, the values for each component of the polymer architecture are listed in table 4-1.

v	n_m	C_∞	$l\ (\mathring{A})$	$\langle r^2 \rangle^{1/2}$ (nm)	L_e^2	c^* (ppm)	c^* (wt %)
0.55	1.36×10^5	4.1	1.47	165	2.44×10^4	741	0.0741%

Table 4-1. Polymer architecture for PEO ($M_W = 2,000,000$ g/mol). (Value for v from (Tirtaatmadja et al., 2004), C_∞ from (McKinley and Armstrong, 2000))

From this data, it is possible to determine that the fluids dealt with in this paper are primarily in the semi-dilute concentration region. The concentration of the 0.1% PEO is very close to the overlap concentration ($c/c^* = 1.3$) and would be expected to behave more like a dilute solution where polymer molecules act independently. Conversely, the 0.3% PEO is clearly beyond the dilute limit ($c/c^* = 4.0$) and polymer interaction would have a larger effect on its rheological properties. Only the 0.05% PEO would be within the dilute range ($c/c^* = 0.7$).

The rheological measurements in the next sections lead to characterization of these fluids in comparison to the dilute solution approximations. But for each fluid, elastic stresses are large enough in these channels to exceed the inertial stresses. This leads to relatively large elasticity numbers (see section 2.1). However, unlike many previous studies, inertia cannot be neglected, leading to interesting flow properties.

4.2 Viscosity Measurement

It was critical to determine the steady shear behavior of the fluid in order to resolve the Reynolds and elasticity numbers. To measure the viscosity a controlled stress rheometer (TA Instruments AR2000) was used in shear flow. A double gap Couette cell fixture on the AR2000 was used to characterize the viscous properties of each fluid employed in these experiments (see figure 4-2). The Couette cell consists of three concentric cylinders, and it is generally used for low viscosity fluids because this geometry increases the total wetted surface area. Fluid fills the gap between the inner stationary cylinder (stator) and the outer rotating cylinder (rotor) and also between the rotating cylinder and the outer stationary cylinder. Thus total shear stress, and therefore the measured torque, is

large enough to accurately characterize mobile fluids. The gaps between the inner and outer cylinders are set to keep the shear rates constant, even though the rotor has a higher velocity at the outside:

$$\dot{\gamma} = \frac{\Omega \bar{R}_D}{\Delta R_D} \tag{4.9}$$

where Ω is the angular velocity of the rotor, $\bar{R}_D$ is the average radius, and ΔR_D is the difference between the inner and outer radius, such that:

$$\frac{\left(R_{R,i} + R_{S,i}\right)}{2\left(R_{R,i} - R_{S,i}\right)} = \frac{\left(R_{R,o} + R_{S,o}\right)}{2\left(R_{S,o} - R_{R,o}\right)} \tag{4.10}$$

where $R_{R,i}$ (20.38 mm) and $R_{R,o}$ (21.96 mm) are the inner and outer radius of the rotor, respectively, and $R_{S,i}$ (20 mm) and $R_{S,o}$ (22.38 mm) are the inner and outer radius of the stator (see figure 4-2). Because the AR2000 is a controlled stress rheometer, it is advantageous to ramp the stress over several decades. For the present tests, the range of achievable torques was spanned (0.1 – 200,000 mN-m).
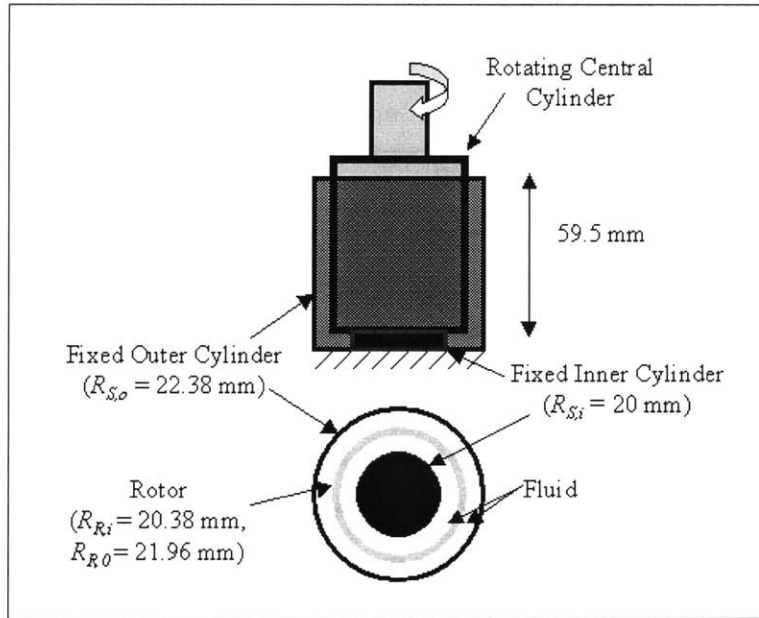
Figure 4-2. Schematic of double gap Couette cell for AR2000

To ensure the rheometer is accurately measuring the torque on the system and the Couette cells are concentrically aligned, a calibration fluid (Cannon Instrument Co.) is used. The calibration fluid is purely viscous, and shear viscosity measurements should be

independent of stress (and shear rate). The viscosity of this fluid is tabulated for 20°C to be 4.004 mPa·s. Tests on this fluid yield fluid viscosities close to the tabulated value (within 6% for all valid shear rates) confirming the accuracy of the rheometer (figure 4-3). Tests were then performed on all of the fluids to be used in this study at 20°C. The viscosity for all of these fluids is plotted as a function of shear rate in figure 4-3.
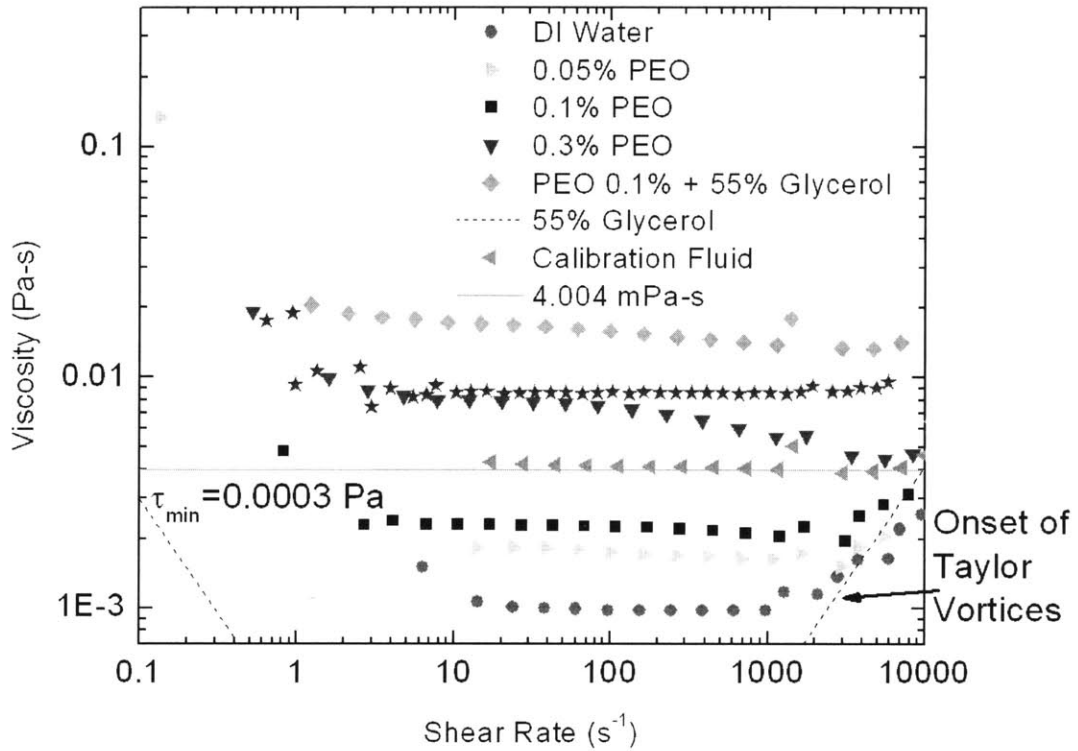
Figure 4-3. Rheological data for fluids employed in this study

At high and low shear rates the viscosity data is errant. At low shear rates, the torque required is too small to generate constant shear flow. As the shear stresses decrease toward the noise floor of the rheometer, the measured viscosity increases. This tendency is evident based on the formula for calculating the viscosity:

$$\eta = F_{Couette} \frac{T}{\dot{\gamma}} \tag{4.11}$$

where T is the applied torque and $F_{Couette}$ a factor with units of the inverse of a volume based on the geometry of the present Couette system ($F_{Couette} = 2976$ m^{-3}). For low shear rates, the applied torque is dominated by system noise, and the resulting viscosity scales

as the inverse of the shear rate. At higher shear rates, the low Reynolds number approximation is exceeded and the fluid inertia begins affecting the data. Inertial forces can generate secondary motion known as Taylor vortices when an inner cylinder is moving in a Couette cell (Macosko, 1994). Stresses are required to generate these vortices and the resulting measured torque exceeds the torque strictly associated with the viscous stresses. The onset of Taylor instabilities are reached at a critical Taylor (Ta) number, which for the present setup is defined as:

$$\text{Ta} = \frac{\rho^2 \Omega^2 \left(R_{S,o} - R_{R,o}\right)^3 R_{R,o}}{\eta^2} > 3400 \tag{4.12}$$

For a fixed geometry, the onset of Taylor vortices is only dependent on the fluid's viscosity and density. For many of the fluids examined in this study the onset of this instability is 2000 – 5000 s^{-1}, which is also where data begins to diverge for its thinning behavior (see figure 4-3). However, Macosko also reports that the onset of these instabilities is actually delayed by non-Newtonian effects (Macosko, 1994).

A turbulent instability occurs in outer cylinder rotations, which would be the inner gap for the Couette cell used in this study (Macosko, 1994). However, the condition for this instability (Re > 50,000) occurs at higher velocities than the onset of a Taylor vortex. A final instability, which would cause errant viscosity measurements, is a periodic instability dependent on a critical Deborah number (Larson, 1992). However, a critical condition for this instability is determined by the ratio of the inner and outer radius:

$$\kappa = \frac{R_{S,o}}{R_{R,o}} \tag{4.13}$$

This instability can be ignored when this ratio is greater than $\kappa = 0.95$, which is the case for the AR2000 double gap Couette cell ($\kappa = 0.98$).

Thus, the onset of a Taylor instability is the limit of the rheometer. Thus shear viscosity data is accurate for a range of shear rates from approximately 10 s^{-1} to 1000 s^{-1}. This is a large range, however shear rates generated in the microchannels are even larger than the maximum values achievable on the rheometer (section 5).

In order to perform Cogswell's analysis (section 2.2), fluid is assumed to be a power-law fluid of the form of equation (2.23). For all of the fluids observed, except the 0.3% PEO solution, a constant viscosity is a reasonable approximation (within 15% for all other fluids). But there clearly is a weak dependence on the shear rate. At high shear rates, even small amounts of shear thinning can greatly reduce the pressure loss in channel flow (Bird et al., 1987). Data is fit to power-law curves, and values for calculating the power-law behavior of each fluid, m and n, are included in table 4-2. Zero-shear-rate viscosities are also determined for each fluid at the lowest shear rate at which viscosity measurements are valid.

Fluid	η_0 (mPa·s)	m (Pa·s^n)	n	Shear Rates (s^{-1})
DI Water	1.01	0.0010	0.992	20-1000
0.05% PEO	1.84	0.0020	0.970	10-1000
0.1% PEO	2.32	0.0025	0.977	10-1000
0.3% PEO	8.31	0.0132	0.880	50-1000
0.1% PEO + 55% Glycerol	18.20	0.0192	0.956	1-800
55% Glycerol	8.59	0.0087	0.995	10-1000
Calibration Fluid	4.22	0.0045	0.985	10-1000

Table 4-2. Rheological data from double gap Couette cell

For the 0.1% PEO solution the power-law index, n, is relatively close to unity ($n = 0.977$). In fact for the calibration fluid it falsely appears that there is some dependence ($n = 0.985$) on the shear rate. One can conclude that this sets the limit on how close to a constant viscosity fluid one can measure to be within 1.5%. So one would assume that the viscosity of the 0.1% PEO fluid is slightly more dependent on shear rate than this error limit, and data is in fact due to shear-rate dependence. But for the 0.3% PEO solution n is small enough ($n = 0.880$) that it is clearly due to shear thinning of the fluid, which will be important in evaluating the resulting pressure drop in channel flow. The dependence of the power-law index on concentration is plotted in figure 4-4. Figure 4-4 also contains a plot of the zero-shear-rate viscosity against the viscosity and is compared with the prediction for dilute solutions. For the graph, it is clear that the 0.3% PEO solution is clearly beyond the dilute solution limit. However for the 0.05% and 0.1% PEO solutions, the dilute solution prediction is within 20% of the measured viscosities.
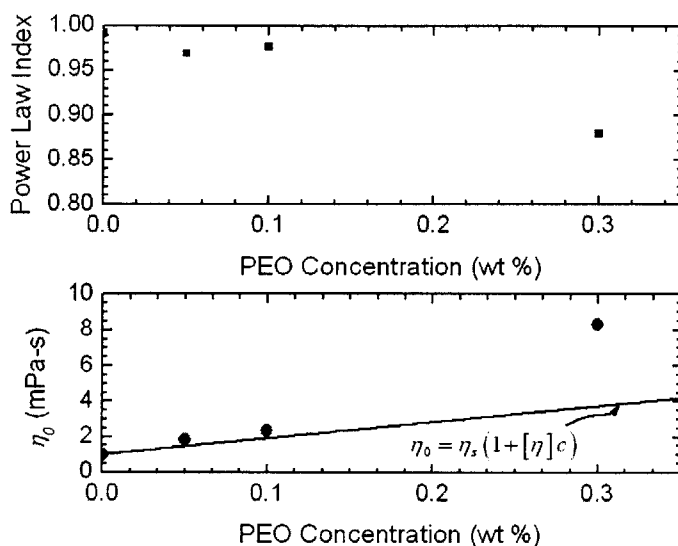
Figure 4-4. Effects of PEO concentration on power law index and zero-shear-rate viscosity. Values for zero-shear-rate viscosity are compared with dilute polymer solution prediction.

A cone and plate fixture was also used in an attempt to measure the first normal stress difference, N_1. A lightweight cone (acrylic) was used to minimize the geometry inertia, however, the values of the normal stress difference were small and inconsistent from trial to trial. The steady shear data from these experiments were used to test the accuracy of the Couette cell measurement. The cone and plate tests matched the Couette cell results to within 10% for all fluids.

Attempts were also made at measuring the storage modulus and loss modulus using small amplitude oscillatory shear (SAOS) experiments for both the Couette cell and the cone and plate rheometer. However, a linear viscoelastic region was not definitive from strain sweeps data and resulting SAOS data was not acceptable. Even in the most viscous fluid, which should have the longest relaxation times, data was not conclusive due to the small magnitude of the resulting torques. All data for the storage modulus was just system noise. With the small magnitude of the relaxation time, it is also likely that SAOS data is only relevant at large oscillatory frequencies, beyond the limits of the rheometer.

4.3 Relaxation Time

4.3.1 Dilute Solution Theory

It is useful to calculate the relaxation time for the fluids in the limit of dilute concentration even though it may be inaccurate. This value will at least provide an order of magnitude estimate of the appropriate relaxation time and a lower bound limit for the relaxation time. It also gives physical intuition as to the physico-chemical factors that affect the relaxation time of a polymer solution. Zimm theory is used to predict the longest relaxation time of a polymer solution in the limit of infinitely small concentration:

$$\lambda_1 = \frac{1}{\varsigma\left(\frac{3}{2}\right)} \frac{[\eta]\eta_s M_w}{RT} \tag{4.14}$$

where $[\eta]$ is the intrinsic viscosity, η_s is the solvent viscosity, and R is the universal gas constant. This relaxation time is for a good solvent, however, it is useful to adjust the front factor as adopted from Tirtaatmadja et al. (2004) specific to PEO in water for a solvent quality factor (v) of 0.55.

$$\lambda_1 = 0.463 \frac{[\eta]\eta_s M_w}{RT} \tag{4.15}$$

Since this theory assumes that the solution is infinitely dilute, there is no dependence of relaxation time on polymer concentration. Thus, there is no change in the predicted values of relaxation time for each water-based solution.

The intrinsic viscosity is determined from the Mark-Houwink-Sakurada equation, which estimates the intrinsic viscosity as:

$$[\eta] = KM_w^a \tag{4.16}$$

where a is the same exponent referred to in section 4.3.1 and K is a coefficient determined empirically for different polymers and solvents. From Tirtaatmadja et al., values of K and a were determined to be $K = 0.072$ ml/g^{a+1} and $a = 0.65$ for PEO in water (2004). These values were also in agreement with tabulated values from the Polymer

Handbook (Brandrup et al., 1975). The resulting relaxation time for 2,000,000 g/mol molecular weight PEO in water from Zimm theory is computed from equation (4.14) to be 0.34 ms at 20°C.

While Zimm theory may not be adequate for the dilute and semi-dilute fluids examined in this thesis, it does lend insight into how the relaxation times of the fluids vary with both molecular weight and solvent viscosity. Since the relaxation time is a linear function of solvent viscosity, solutions of PEO in glycerol and water were used as a simple means of increasing relaxation times. Despite being able to determine the effects of molecular weight and solvent viscosity, it is still necessary to find a means of measuring all relaxation times.

4.3.2 Capillary Breakup: Theory

Standard rheological tests and theoretical calculations fall short of providing an accurate measure of the relaxation time for the fluids employed in this study. Instead, another means of physically measuring the relaxation time was required. However, many standard rheological techniques require that the fluid be viscous enough to generate relatively large forces. For the low viscosity fluids employed in this study, there are a limited number of ways in which the relaxation time can be measured. Also, it is preferred to measure the relaxation time in a way that is similar to the experiments to be performed. For this case an extensional flow was desired, unlike the typical shear relaxation time obtained from SAOS experiments. In extensional flow polymer molecules are stretched, not sheared, which means the polymer molecules in solution behave differently. As a result the time required to return to the undeformed state is different, yielding a different relaxation time. Previous studies have been performed to measure relaxation time of similar PEO solutions using droplet breakup (Vance et al., 2000; Tirtaatmadja et al., 2004). For the present study, a means of balancing elastic stresses with capillary forces was employed by using a capillary breakup extensional rheometer (CABER).

The CABER experiment consists of two circular plates (radius, $R_0 = 3$ mm) between which the fluid is confined by its own surface tension at an initial gap, h_0, of 3 mm. The top plate quickly moves (50 ms) to a specified distance ($h_f = 9 - 12$ mm) away from the bottom plate (see figure 4-5). The final aspect ratio of the fluid thread is defined as:

$$\Lambda = \frac{h_f}{2R_0} \tag{4.17}$$

The fluid is allowed to thin under the capillary stresses and eventually breaks. A laser sheet is positioned at the midpoint of the final position of the two plates and measures the diameter of the fluid filament between the two plates as the fluid thins. The CABER instrument samples the fluid diameter at a rate of 1000 Hz.
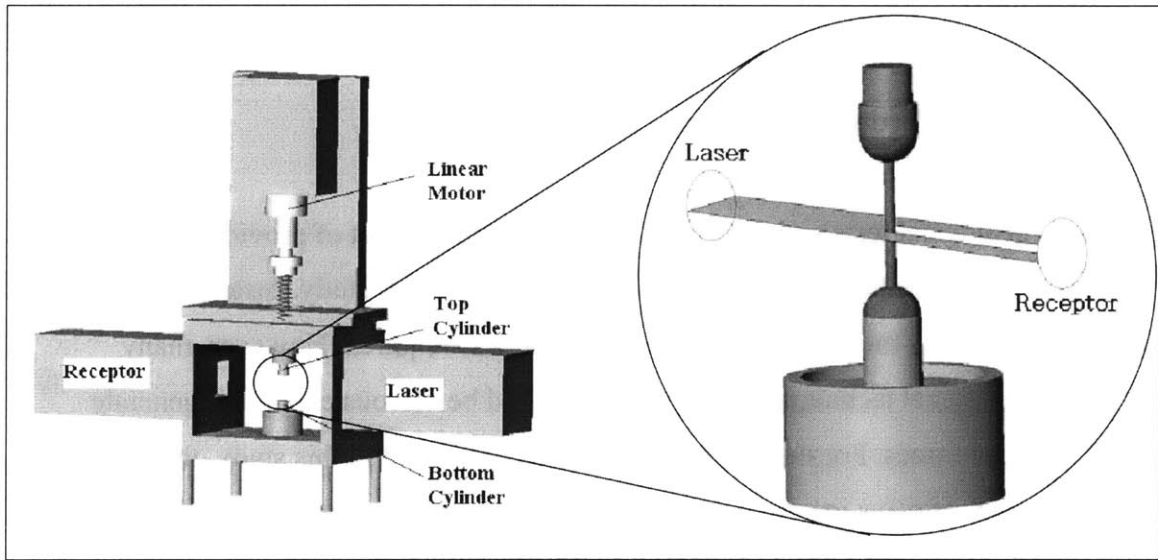
Figure 4-5. Schematic of CABER setup (picture adopted from (Verani and McKinley, 2004))

Extracting relaxation times from the CABER measurement of the midplane radius as a function of time is based on the stress balance between surface tension and elastic stresses. Calculating the relaxation time from the radius-time data is based on an extensional decay of the radius with time. In high-molecular-weight polymers with low viscosities, the capillary forces in the filament drive the flow (Bazilevskii et al., 2001). For fluids with a single relaxation time, the balance of surface tension and internal fluid elasticity reduces to the following time-dependent exponential decrease in filament radius (Entov and Hinch, 1997; Bazilevskii et al., 2001):

$$R = R_f e^{\frac{-t}{3\lambda}}$$
(4.18)

where R_f is the radius of the filament at time ($t = 0$) when the two plates are completely separated. This result is independent of any inertial effects, so aspect ratios were adjusted to eliminate inertial effects from the system.

Studies have been performed to determine if the aspect ratio in capillary thinning experiments has any effect on the calculated value of the relaxation time for polymer solutions (Stelter and Brenn, 2000). Stelter and Brenn concluded that the aspect ratio could have an effect on the measured relaxation time if the solution was beyond the semi-dilute region. However because all fluids in the present study fall within this region, relaxation times are expected to be independent of aspect ratio.

The relaxation time is also dependent on the rate at which the fluid is being stretched or sheared. The CABER generates a uniaxial extension as the filament thins. To evaluate the stretch rate of this motion it is necessary to compare the equation of motion for an extensional flow with that of the CABER. For a uniaxial extension:

$$\frac{dR}{dt} = -\frac{1}{2}\dot{\varepsilon}R$$
(4.19)

Solving this equation and equating it for (4.18) CABER experiments yields that:

$$\lambda\dot{\varepsilon} = De = \frac{2}{3}$$
(4.20)

The internal stresses of the system keep the fluid thread necking at a natural Deborah number of 2/3. Thus the actual strain rate at which the relaxation time is measured is dependent on the fluid employed.

For the preceding analysis to be valid, inertial stresses and viscous stresses should be small compared to elastic stresses. To determine the limits of this instrument, it is necessary to compare the time scales associated with the evolution of the different stresses and to compare them with the time scales of the instrument.

The time scale associated with the balance of surface tension and inertial stress is referred to as the Rayleigh time scale (t_R), which is defined as:

$$t_R \approx \sqrt{\frac{\rho R_0^3}{\sigma}}$$

(4.21)

where R_0 is the radius of the fluid droplet and σ is the surface tension of the fluid (for simplicity $\sigma \approx \sigma_s = 0.07$ N/m, where σ_s is the solvent surface tension). This time is also the inverse of the natural frequency associated with the fluid droplets. For the CABER instrument the Rayleigh time is approximately $t_R = 0.02$ s for an aqueous solution. Also the associated time scale from the balance of viscous and capillary stresses on the systems is defined as:

$$t_V \approx \frac{\eta_0 R_0}{\sigma}$$

(4.22)

Typically the CABER is used to measure the extensional viscosity of a fluid undergoing breakup, but for the CABER to be able to measure this quantity, it is necessary that the viscous time scale to be greater than the Rayleigh time. This viscous time scale is based on the viscosity of the fluid being constant. For the fluids examined in this study, the viscous time scale is approximately $t_V = 10$ ms at its largest value (for the most viscous fluid).

Because the viscosity for all fluids used in these experiments is less than those required, the inertial time scale is dominant ($t_V/t_R \approx 0.5$). To be able to measure elasticity it is necessary that the relaxation time be larger than the maximum time scale of the system, which for this case is the Rayleigh time scale. So it is required that:

$$De_0 = \frac{\lambda}{\sqrt{\frac{\rho R_0^3}{\sigma}}} > 1$$

(4.23)

Where De_0 is an intrinsic Deborah number comparing the system's elastic and inertial time scales. Based on this description, the minimum resolvable relaxation time for this system is approximately 20 ms. Adding glycerol and PEO does not significantly change the density ($\sim 15\%$) or the surface tension ($\sim 10 \%$), so this value is relatively constant for all solutions used in these experiments. However, these are only order of magnitude

values as capillary thinning can be observed even at lower timescales. This is possible because the elastic stresses grow as the filament thins, while inertial stresses are dissipated due to damping.

Using the Rayleigh time as the approximate relaxation time of the fluids studied in this examination, the extension rate is approximately $\dot{\varepsilon} = 30$ s^{-1}. This is much smaller than the expected extension rates for the microchannel contraction ($\dot{\varepsilon} > 10,000$ s^{-1}), but it is an accurate means of evaluating a relaxation time because it is an extensional flow. Other techniques, such as drop break-up, for measuring the relaxation times of dilute solutions usually are based on the same principle of fluid necking due to capillary stresses and, therefore, yield rheological data at the same natural Deborah number of 2/3 (Tirtaatmadja et al., 2004).

4.3.3 Capillary Breakup – Results

For each fluid employed in this study (even Newtonian), tests were performed to measure a relaxation time. Typical thinning and breakup behavior are included in figure 4-9. Images in figure 4-6 are taken even intervals ($\Delta t = \dfrac{t_{event}}{5}$, where t_{event} is the time until breakup of the filament) showing the thinning behavior of the various fluids until breakup at an aspect ratio of 1.61. The pictures are taken using a Phantom V5.0 high-speed camera (1000 frames per second). The sensor obtains images at 512 by 216 pixels, exposing each image for 0.214 ms. The image is magnified by a factor of 1.7 and the resolution of each image is 26.8 μm per pixel. For each trial performed, video is examined to ensure that the fluid is thinning in the appropriate exponential fashion without interference (either external or due to unexpected behavior of fluid droplets). From these images in figure 4-6, it is clear that filaments form easily without droplets interfering with data.

0.1% PEO, $\Lambda = 1.6$ $t_{event} = 50$ ms , $h_o = 3$mm

t=-50ms   t=0   t=0.2t_{event} t=0.4t_{event} t=0.6t_{event} t=0.8t_{event} t=t_{event}

0.3% PEO, $\Lambda = 1.6$ $t_{event} = 110$ ms, $h_o = 3$mm

t=-50ms   t=0   t=0.2t_{event} t=0.4t_{event} t=0.6t_{event} t=0.8t_{event} t=t_{event}
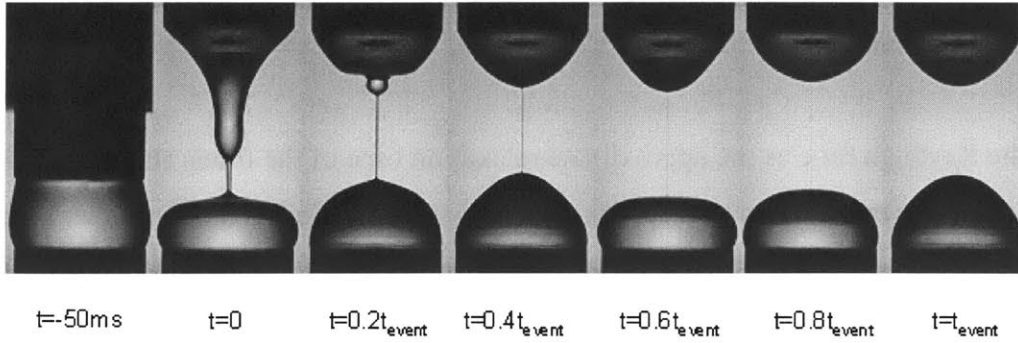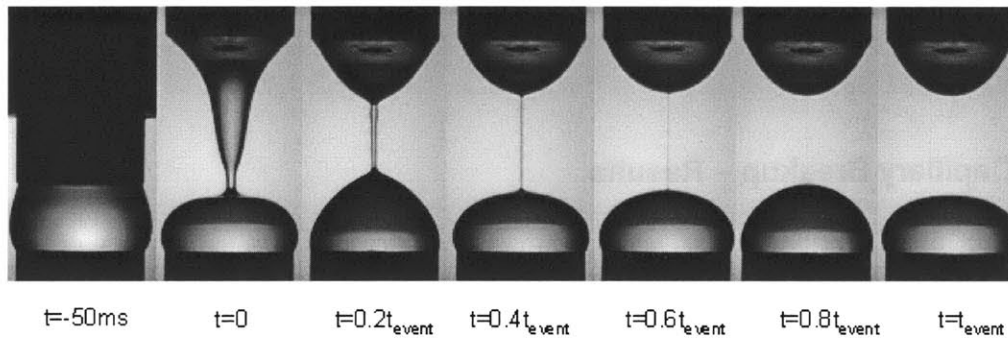
0.1% PEO in 55%wt. glycerol/water, $\Lambda = 1.6$ $t_{event} = 550$ ms, $h_o = 3$mm

t=-50ms   t=0   t=0.2t_{event} t=0.4t_{event} t=0.6t_{event} t=0.8t_{event} t=t_{event}
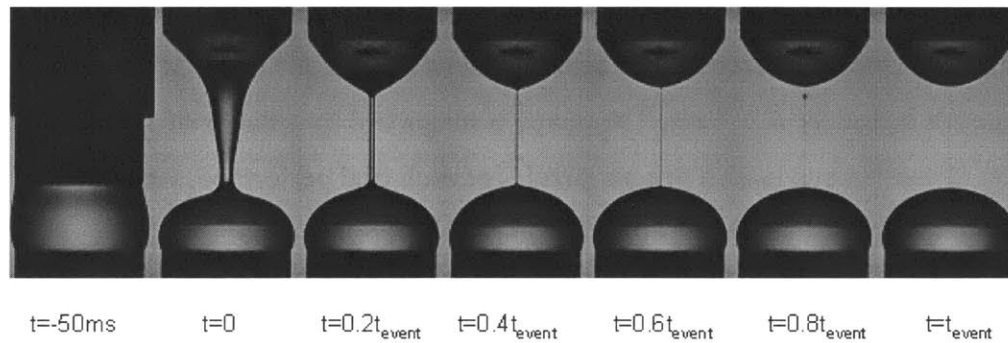
Figure 4-6. High-speed video of capillary thinning on CABER for 0.1% PEO, 0.3% PEO, and 0.1% PEO + 55% Glycerol. Images are taken at six equal intervals from when the plates are fully separated until filament break-up

Data for the CABER experiments are analyzed to determine the relaxation times. Time zero is defined as starting after the 50 ms during which the plates are still moving apart. Data from time zero onward is plotted on a semilog plot and fit to an exponential curve (figures 4-7 and 4-8) to determine the relaxation time as defined in equation (4.18). Five tests were performed for each fluid at four different aspect ratios. The resulting relaxation times are averaged for each aspect ratio and are plotted in figure 4-9. In the present study, aspect ratio effects were not significant (relaxation time is constant to within 20%) and the relaxation time was mostly independent of the aspect rate. The only effect of the aspect ratio was its impact on how smoothly the filament formed. At high aspect ratios, droplets frequently formed in low viscosity fluids, interrupting the relaxation data. At lower aspect ratios, the droplets that form on the top and bottom plate frequently oscillate into the region being measured by the laser.
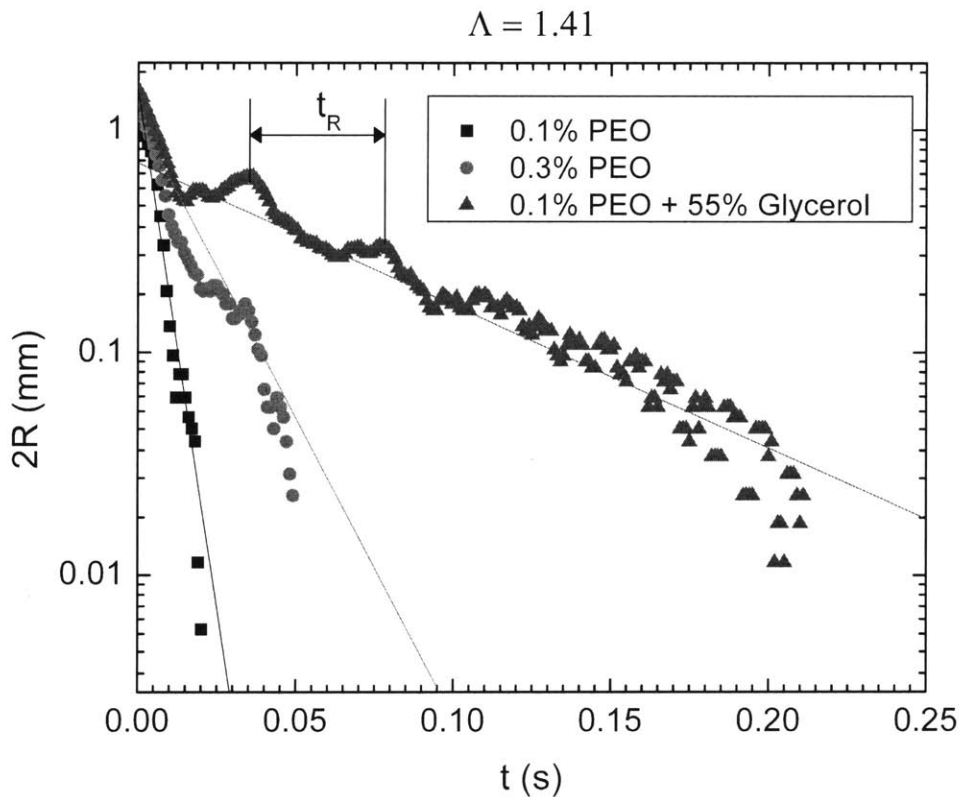
Figure 4-7. CABER results at the lowest aspect ratio ($\Lambda = 1.41$). 0.1% PEO in 55% glycerol and water data shows oscillations at the Rayleigh frequency.

$$\Lambda = 1.61$$
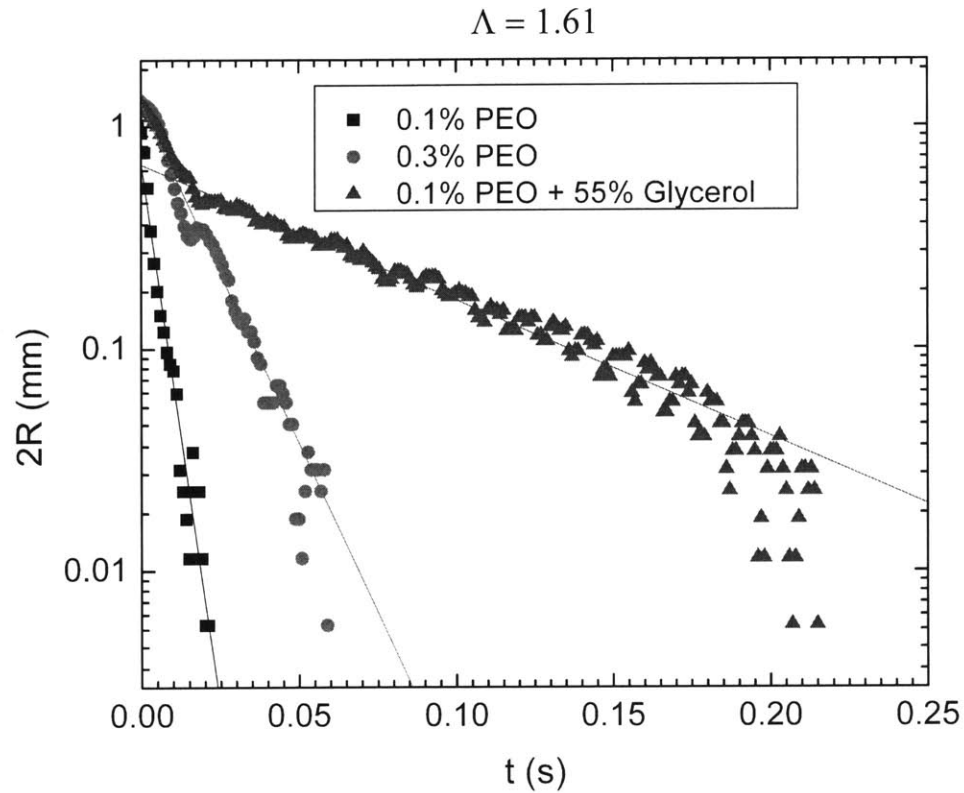
Figure 4-8. CABER results from medium aspect ratio ($\Lambda = 1.61$)
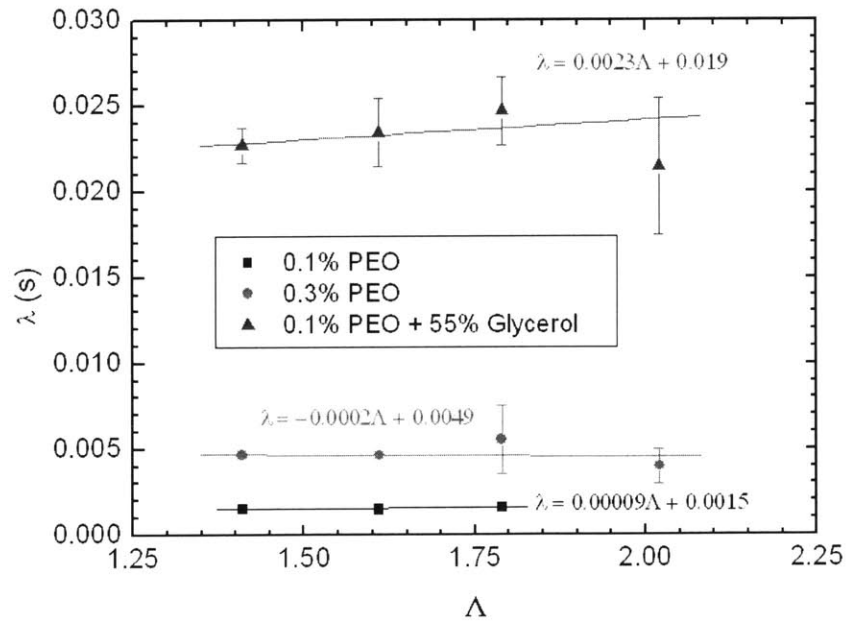
Figure 4-9. Relaxation time average over 5 trials for each aspect ratio. For each fluid, the dependence on the aspect ratio is weak and appears random. For the less viscous fluids at low aspect ratios the data was either precise (within 10%) or completely inaccurate, and therefore ignored. As a result, error bars for these fluids are small.

For most experiments the data was clean enough to determine a relaxation time. However for the less viscous fluids (the 0.3% PEO and 0.1% PEO solutions) the formation of droplets frequently interfered with the data at higher aspect ratios (figure 4-10). For these experiments data was ignored and only clean trials were incorporated in the tabulated values. At the highest aspect ratio, it is impossible to determine any significant material information about the 0.1% PEO, and no relaxation time is recorded. For the 0.1% PEO in glycerol and water, the fluid relaxation time was easily determined for each trail, as the rheological properties resulted in clean data. However, an interesting phenomenon can be determined from the data. At low aspect ratios it is possible to determine the Rayleigh time scale from the oscillating frequency of the top and bottom droplets. At the lowest aspect ratio, the droplet moves in and out of the range of the measured radius, yielding a damped periodic error at the frequency of the Rayleigh time scale (see figure 4-11). This natural oscillating time scale is evident from the 0.1% PEO in 55% glycerol and water from figure 4-7.
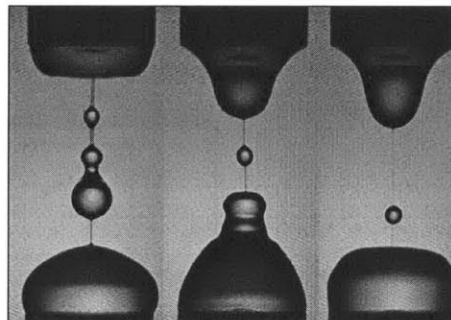
Figure 4-10. Images of droplet formations in 0.1% PEO which cause errant data at high aspect ratios ($\Lambda = 2.02$) (Image courtesy of Lucy Rodd)

t=10ms   t=26ms   t=47ms   t=66ms   t=88ms   t=110ms
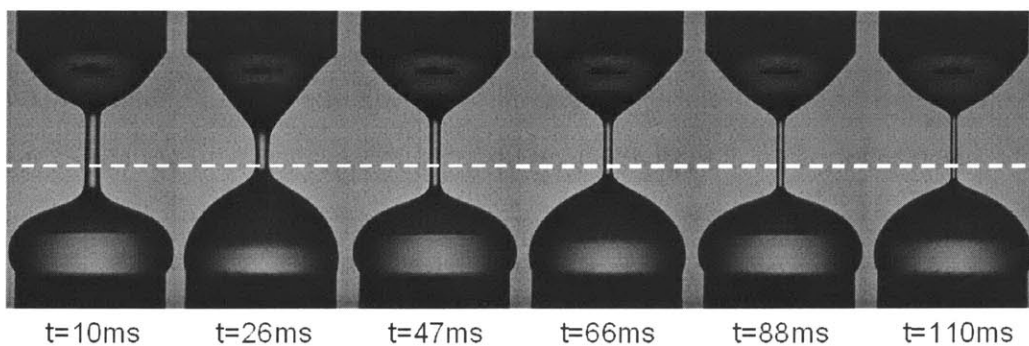
Figure 4-11. Images of the damped oscillations of the lower droplet which can interfere with CABER measurements. Images are taken for the 0.1% PEO in 55% glycerol and water solution at an aspect ratio of $\Lambda = 1.41$.

Following the initial experiments, trials were performed on a 0.05% PEO solution. This fluid was clearly approaching the limits of the accuracy of the CABER instrument as inertial effects were evident at most aspect ratios. Results resolved relaxation times at only the lowest aspect ratio ($\Lambda = 1.41$). At all higher aspect ratios droplet formations interfered with the relaxation data. The value of this relaxation time is only slightly less than that obtained for 0.1% PEO (table 4-3), indicating that the solution is below the overlap concentration c^*, which is as predicted in section 4.3.1.

Also, to demonstrate the effect of fluid elasticity on the results in this setup, figure 4-12 shows the difference in the thinning behavior of the 0.1% PEO in 55% glycerol and water and the Newtonian 55% glycerol and water solution. Clearly the elasticity of the polymer solution is responsible for the exponential decay in the midplane radius. The only data in which the Newtonian fluid formed a clean thinning behavior (no droplets) was at a ratio of 1.22. But because the aspect ratio was found to have little effect on the thinning effect, the difference in the aspect ratio for these two trials is negligible.
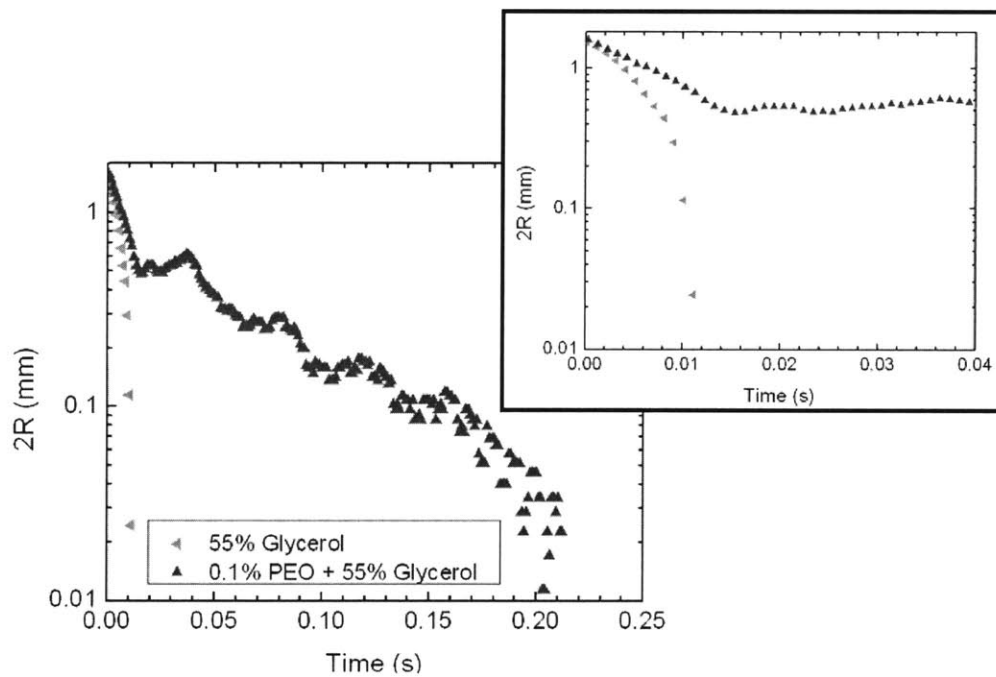
Figure 4-12. Comparison of the thinning data of a polymer solution (0.1% PEO + 55% Glycerol and Water) and a Newtonian fluid (55% Glycerol and Water). Data is taken at aspect ratios of $\Lambda = 1.41$ and $\Lambda = 1.22$, respectively.

Based on all the experiments performed and linear regression data from the plots in figure 4-9, it appears that capillary breakup behavior is independent of the aspect ratio for these dilute solutions. The values for the relaxation time are averaged over accurate result (containing no droplets) for different aspect ratios. These values are included in table 4-3. For the 0.1% and 0.3% PEO solutions the relaxation time is less than the Rayleigh timescale, however, these values are still well determined for the experiments. It is clear that the thinning data is due to elasticity, as for Newtonian fluids, the thinning behavior is not an exponential decay (see figure 4-12). CABER tests on water resulted in errant data, which resulted in a relaxation time of 0.6 ms. This value then provides a measure of the error of the system, which adds confidence to the data for low viscosity solutions.

Fluid	Relaxation Time (ms)	λ/η_s (Pa^{-1})
0.05% PEO	1.5 ± 0.4	1.49
0.1% PEO	1.6 ± 0.3	1.58
0.3% PEO	4.6 ± 1.0	4.55
0.1% PEO + 55% Glycerol	23.0 ± 2.1	2.68

Table 4-3. Relaxation times for fluids used in the present study

Relaxation time values varied by less than 2.1 ms for each trial using the 0.1% PEO in 55% glycerol and water. For the 0.1% PEO solution, the relaxation times only varied by 0.3 ms from trial to trial. For the 0.3% PEO solution, the relaxation times varied by as much as 1 ms from trial to trial. For all of these the error is less than 20%, which is within a reasonable range and indicates repeatability and validity of the measured data.

From the analysis on Zimm theory, one might expect that the relaxation time would scale with the solvent viscosity for the same concentration of PEO. However, from Table 4-3, it is clear that there is a difference between the value of the relaxation time divided by the solvent viscosity for the 0.1% PEO in water solution and the 0.1% PEO in 55% glycerol and water mixture. This discrepancy is derived from the fact that both the intrinsic viscosity and the solvent quality factor (ν) are dependent on the solvent in addition to the polymer (Brandrup et al., 1975).

4.3.4 Comparing Relaxation Times

Clearly the relaxation times measured by the CABER are significantly greater than the values determined through Zimm theory (at least 5 times). Rothstein noted that calculated relaxation times were 20 times greater than measured zero-shear-rate relaxation times determined from first normal stress coefficient ($\Psi_1 = \dfrac{-N_1}{\dot{\gamma}_{yx}^2}$) for a Boger fluid (Rothstein and McKinley, 1998):

$$\lambda_0 = \frac{\Psi_{1,0}}{2\eta_0} = 0.29\lambda_z \frac{(\eta_0 - \eta_s)}{\eta_0} \tag{4.24}$$

This relationship gives the longest relaxation time for a linear viscoelastic fluid in the limit of zero-shear-rate (Bird et al., 1987). However for the fluids in the current study, it is difficult to get any measure of the first normal stress coefficient. The magnitude of this relaxation time (λ_0) is different for each solution, depending on the zero-shear-rate viscosity (η_0), however the relaxation time will be approximately 30 times smaller than the relaxation time measured using the CABER tests. There is clearly a discrepancy between measurements and calculations for different polymer solutions. For this reason, it is unclear as to whether the critical Deborah number for these experiments will actually be unity as anticipated. From this analysis, it is best to use the measured relaxation time from the CABER results. These values are the most accurate for an extensional flow, and are therefore most appropriate for the flows considered in this experimentation. They yield results for the relaxation time which have been confirmed and validated through many experiments (Entov and Hinch, 1997; McKinley and Tripathi, 2000; Bazilevskii et al., 2001).

4.4 Density

The density of the fluids was measured using a simple pipette and a scale. A known volume of fluid is acquired by the pipette and massed. Three trials were performed for each fluid and the total density was averaged. Adding PEO to the solvent has the effect of reducing the fluid density, however this amount is small (< 2%) for the water-based

solutions. For the glycerol water mixture the contribution is larger, but still less than 5%. However, it is worth noting that the density of the water and glycerol mixture is significantly larger (15%) than that of pure water.

4.5 Fluid Summary

Based on all previous measured results the fluid properties to be considered for the present flow characterizations are summarized in table 4-4. These properties are as desired for the fluids to be studied by a microfluidic device. For the microchannels considered, the range of achievable flow rates (0.1 ml/hr – 15 ml/hr) allows the microfluidic channels to create a high Deborah number (De $\sim$ 100) with small inertial effects (Re $<$ 10) (see section 2.1). It is now possible to extend the previous rheology to quantify the associated dimensionless parameters of each fluid for thorough entry flow analysis.

Fluid	ρ (g/cm^3)	η_0 (mPa·s)	m (Pa·s^n)	n	c/c^*	λ (ms)
DI Water	0.988	1.01	--	--	0	0
0.05% PEO	0.986	1.84	0.0020	0.970	0.7	1.5
0.1% PEO	0.985	2.32	0.0025	0.977	1.3	1.6
0.3% PEO	0.971	8.31	0.0132	0.880	4	4.6
55% Glycerol + Water	1.136	8.59	--	--	0	0
0.1% PEO + 55% Glycerol	1.085	18.20	0.0192	0.956	1.3	23.0

Table 4-4. Summary of fluid properties

5 Results and Discussion

For nearly all of the results in this section, the 16:1 contractions ($W_c = 25\ \mu$m) were used as the working channels. These contractions were dimensionally the most accurate compared with the designed specifications (within 5%). The radius of curvature ($\sim 3\ \mu$m) on all features is nearly constant, thus for the smaller channels, these rounded corners are more significant with respect to the total geometry. Also, using a contraction ratio of $\beta_P = 16$ as opposed to $\beta_P = 4$ was advantageous to compare with axisymmetric experiments with equivalent Hencky strains. However, a 4:1 ($W_c = 50\ \mu$m) contraction was used in flow visualization for one trial to determine the nature of elastic instabilities.

5.1 Streak Images

Because the results of many previous papers only included streak images, these were the primary means of comparing the present experiment with those performed on the macroscale. It was desired to determine whether vortex enhancement could be generated on the microscale, as it has been observed for Boger fluids in axisymmetric contractions. From the images obtained it is possible to calculate the associated vortex lengths (L_v, see figure 2-3) and determine the Deborah numbers associated with the onset of elastic effects.

5.1.1 Deionized Water

The first fluid examined is a Newtonian fluid, as a controlled experiment. Clearly water has no associated elasticity, and no vortex enhancement would be anticipated. Spanning all flow rates with DI water as the working fluid, the contraction flows appeared laminar and reversible, as expected (see figure 5-1). It is difficult to resolve any vortex length from the upstream region, as particles approach the salient corner but never touch it completely. Since no particles enter this region, it is not possible to determine the nature of the flow, but from previous analyses, a vortex must exist in this corner (Nguyen and

Boger, 1979). However, this detachment length remains constant at approximately 20 μm for all flow rates considered.

a)

d)

b)

e)

c)

f)
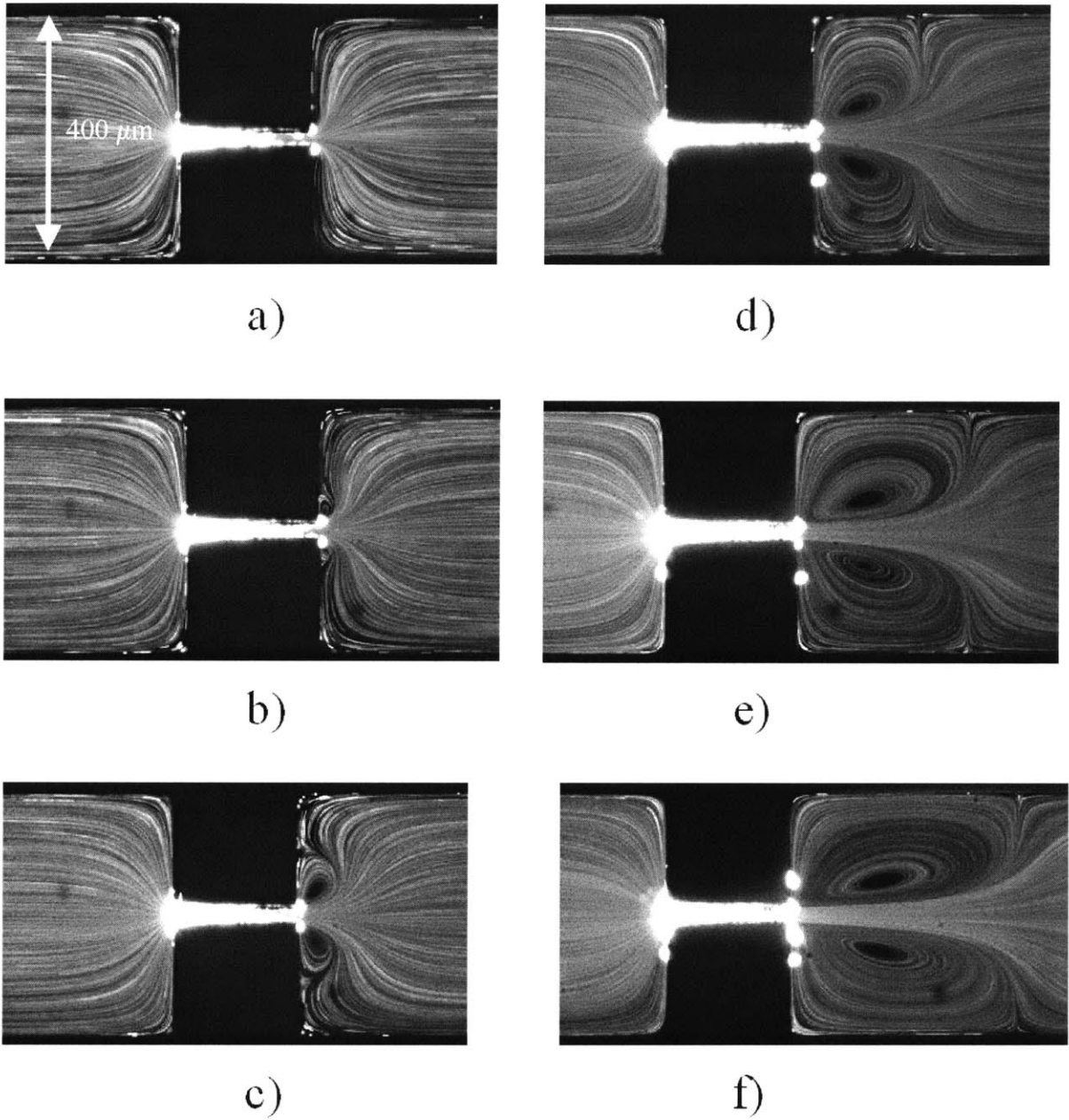
Figure 5-1. Streak images for DI water in 400:25 μm contraction showing the growth of exit vortices (a) Re = 5.5 (b) Re = 8.3 (c) Re = 14 (d) Re = 22 (e) Re = 33 (f) Re = 44

In observing the exit of the contraction, inertial vortex growth began to develop as flow rates are increased (see figure 5-1 (b – f)). These vortices originate at exit corner of the expansion at a flow rate of 1.5 ml/hr (Re = 8.3). The vortices grow toward the salient corner of the expansion and are symmetric for all flow rates. Vortices do not appear in the entry of the contraction due to the inertial forces which suppress all vortex behavior. However, in expansion flows, inertia works in the opposite fashion, enhancing secondary flows (Townsend and Walters, 1994). The vortices are symmetric for each image, indicating that the flow is stable.

5.1.2 0.1% PEO Solution (El = 11.7)

At low flow rates the behavior of the 0.1% PEO solutions also appears Newtonian: streamlines converge in laminar fashion at the contraction (see figure 5-2 (a)). However, as the Deborah number increases, the streamlines begin to depart from laminar behavior (De = 41 – 55): an indication of the onset of elastic effects. This region is marked by streamlines which appear to have pronounced curvature. As the Deborah numbers grow, elastic vortex behavior begins to appear. With increasing Deborah numbers (55 < De < 96) the flow begins to become unstable. Streamlines appear to cross one another (see figure 5-2 (c)). This is an indication of the fluids desire to begin vortex growth behavior. Closer to the top and bottom surface of the microchannel, shear stresses are larger and velocities are lower. Because the depth of focus for this microscope setup is rather large (38 μm), the images are capturing particle motion for flow close to the channel surface as well as the centerplane, giving the appearance of crossing streamlines. As Deborah numbers increase (De > 96), substantial elastic vortices appear in the corners and flow becomes unstable in time. A single vortex develops which shows preference for one side of the channel. This initial asymmetry (shown in figures 5-2 (d – e)) is resolved as Deborah numbers increase (De > 124). Corner vortices continue to grow with increasing flow rate and remain approximately symmetric for all flow rates observed (figures 5-2 (f – h)). At the highest Deborah numbers observed (De ~ 220) diverging flow is observed in the entry region (figure 5-2 (h)). This regime is marked by flow patterns in which particle

paths begin to expand toward the channel walls while approaching the corner vortex. Over the range of flow rates considered, flows never become unstable.
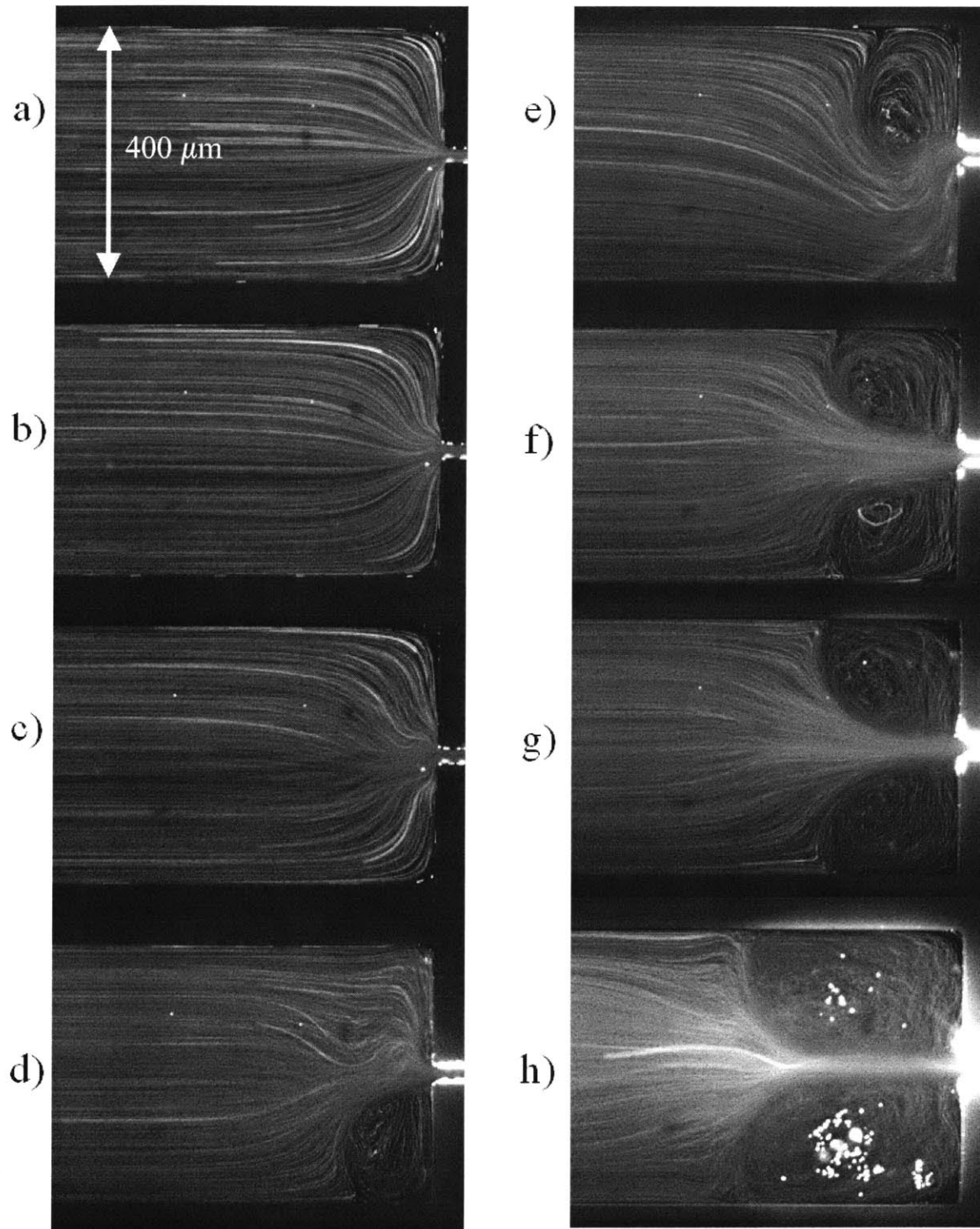
Figure 5-2. Streak images for the 0.1% PEO solution (El = 11.7). (a) De = 27.6, Re = 2.35 (b) De = 41.3, Re = 3.52 (c) De = 55.1, Re = 4.69 (d) De = 96.4, Re = 8.21 (e) De = 110, Re = 9.39 (f) De = 124, Re = 10.6 (g) De = 165, Re = 14.1 (h) De = 220, Re = 18.8

Diverging flow patterns, as seen in figure 5-2 (f – h) are typically observed when shear-thinning behavior enhances the Reynolds number in an attempt to suppress vortex growth (Cable and Boger, 1978). This diverging flow regime typically has a velocity which is maximum far away from the centerline, typically close to the walls of the channel. These flow patterns have been proven experimentally (Cable and Boger, 1978) and numerically (Duda and Vrentas, 1973), but there are few explanations for the off-center maximum velocity. It was also shown by Cable and Boger that these flow patterns are metastable: flow divergence only occurs when flow rates are increased and not when large flow rates are reduced. Because flow never became unstable, the stability of the diverging flow regime was not examined.

Vortex lengths are calculated by using other know distances in the image (channel width) and measuring the detachment length relative to this known distance (see figure 5-3). This method only serves as an approximate measurement, but because vortex lengths are not strictly defined in the flow pattern, it is impossible to measure these values with a resolution better than ± 25 μm. The upstream vortex length is non-dimensionalized and plotted in figure 5-4. The dimensionless vortex length begins at the Moffat eddy (χ = 0.19) and, at the start of instabilities, vortex length increases linearly with the Deborah number for the 0.1% PEO solution. The shaded and empty squares indicate the two different sides of the planar channel. At Deborah numbers beyond De = 150, these are both greater than the Moffat eddy. And at higher Deborah numbers (De > 300) the two vortex lengths become nearly identical.
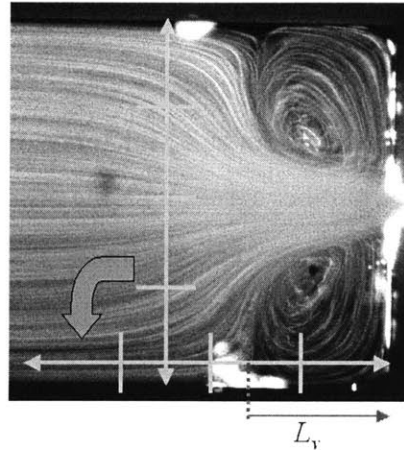
Figure 5-3. Technique used for measuring vortex lengths: upstream width is measured as W_1 = 400 μm and rotated to measure vortex length, L_v
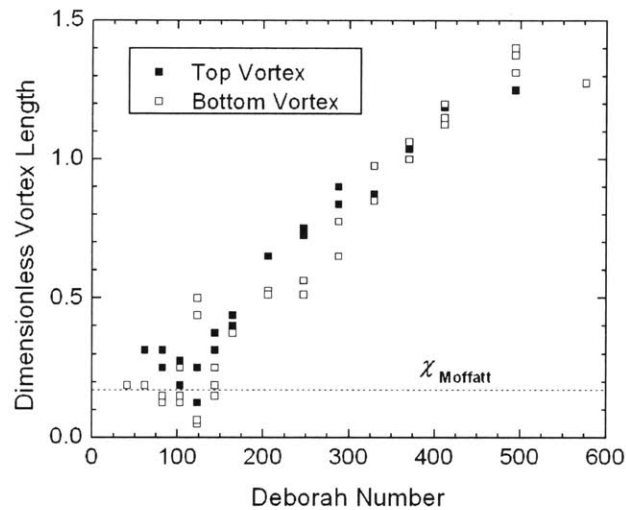
Figure 5-4. Dimensionless vortex length plotted against Deborah number for the 0.1% PEO solution

These results are not in agreement with many of the other observations of planar geometries (Walters and Rawlinson, 1982; Evans and Walters, 1986; Evans and Walters, 1989; Chiba et al., 1990; Chiba et al., 1992). The 0.1% PEO solution is low viscosity and has minimal shear thinning effects, yet vortex growth is observed in planar contraction flow. The Deborah numbers obtained in this study exceed those of other studies of Boger fluids in planar contractions by several orders of magnitude (Walters and Rawlinson, 1982; Evans and Walters, 1986). Vortex growth was not observed until large Deborah numbers (De ~ 50) were obtained, and it is quite likely that other studies failed to generate Deborah numbers which would dictate the onset of extensional effects.

The results for the 0.1% PEO solution are similar to those obtained by many axisymmetric entry flow studies (Rothstein and McKinley, 1998). The linear increase of vortex lengths with the Deborah number agrees with the observations of Rothstein and McKinley for axisymmetric contractions of Boger fluids. The onset of vortex growth, however, occurs at much higher Deborah numbers than anticipated (as compared to Rothstein). This discrepancy is likely due to the difference in means of calculating relaxation time (section 4.3.5) as well as the interplay of inertial effects on the entry flow. Plugging the Zimm relaxation time into equation (4.24):

$$\lambda_0 = \frac{\Psi_{1,0}}{2\eta_0} = 0.29\lambda_z \frac{(\eta_0 - \eta_s)}{\eta_0}$$

the resulting relaxation time would be λ_0 = 54 μs, which is a factor of 30 times smaller than the measured relaxation times. Clearly, the discrepancy between measured values and those which are obtained through the zero-shear-rate limit of the Zimm model is quite large. Rothstein and McKinley used this calculated relaxation time (λ_0) in their study, even though it differed from their measured values (1998). The other factor suppressing vortex development is the confinement of the channels. The height of the channel (h = 50 μm, see table 3-1) in the neutral flow direction is not large enough to be neglected and viscous effects from this top and bottom surface likely serve to inhibit vortex growth. However, the trends of vortex growth for axisymmetric contractions are upheld for the planar contraction in the present study.

The other type of entry flow that is frequently examined is a square/square contraction (Walters and Rawlinson, 1982; Xue et al., 1998; Alves et al., 2003). These studies have frequently found substantial vortex growth in elastic fluids, both shear thinning fluids (Alves et al., 2003) and Boger fluids (Walters and Rawlinson, 1982). However in these studies, the formation of lip vortices were noticeably absent as compared with comparable fluids in axisymmetric and planar contractions. Vortex growth in these studies was also more substantial than in the present study, likely due to the inherent three-dimensional nature of the square/square contraction, which leads to large unequal stress singularities at the entry plane.

In the present study, downstream of the contraction, the vortex behavior is again different from that of water. Instead of vortex growth, vortex suppression is observed. It has been demonstrated that elasticity and inertia have opposite effects on an expansion as they do on an entry flow (Townsend and Walters, 1994; Olson and Fuller, 2000). Inertia serves to suppress vortices in entry flow, but increases secondary flow in flow expansion. Conversely, elasticity induces vortex growth in entry flow, but suppresses vortices in expansions.

5.1.3 0.3% PEO Solution (El = 126)

For the 0.3% PEO solution it was expected to observe similar behavior to the 0.1% PEO solution. However, to ensure that the observed effects were elastic in nature (as opposed to inertial or viscous) vortex growth was expected to occur at the same Deborah number, which, because relaxation times are larger (see table 4-4), translates to a smaller flow rate. For the 0.3% PEO solution the power-law index (n = 0.88) is smaller than that for 0.1% PEO solution (n = 0.98), thus it is anticipated that shear thinning effects may also be important and slightly change entry behavior of the fluid.

At the lowest Deborah numbers, the flow was once again laminar in nature (figure 5-5 (a)). However, as the Deborah number increases (De > 61), a clear lip vortex grows from the reentrant corner (figure 5-5 (b – d)). This vortex grows slowly and moves in an unstable manner in both time and space. Clear instabilities occur as the lip vortex begins to grow outward toward both reentrant corners (figure 5-5 (d)). At Deborah numbers above 123 (2 ml/hr) the flow patterns become more stable. As the Deborah number increases, the vortices grow steadily, however the vortices are clearly asymmetric. This asymmetry is likely due to very small imperfections in the channel geometry that arise during fabrication and are amplified by fluid viscoelasticity. However, at higher Deborah numbers (De > 247), flow patterns become symmetric and diverging flow begins. At large Deborah numbers (De > 330) the flow begins to become unstable: streaklines are no longer clearly defined.
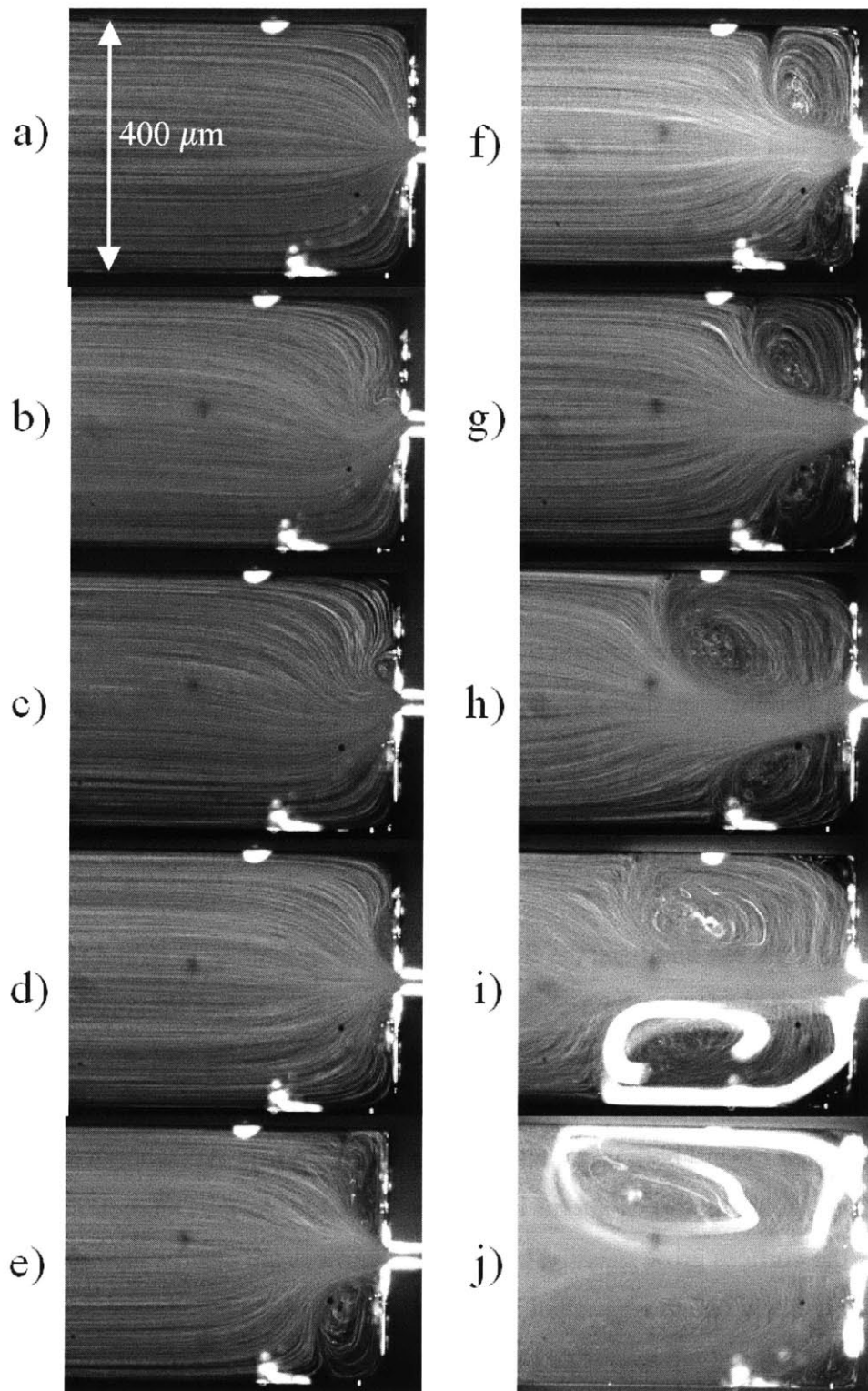
Figure 5-5. Streak images of the 0.3% PEO solution (El = 126) (a) De = 41.2, Re = 0.33 (b) De = 61.7, Re = 0.49 (c) De = 82.3, Re = 0.65 (d) De = 103, Re = 0.82 (e) De = 123, Re = 0.98 (f) De = 144, Re = 1.1 (g) De = 165, Re = 1.31 (h) De = 247, Re = 2.0 (i) De = 330, Re = 2.62 (h) De = 494, Re = 3.9

An interesting flow phenomena can be observed at the higher flow rates for the 0.3% PEO solution. At Deborah numbers greater than 330, a tertiary flow pattern is observed (figure 5-5 (i – j)). The standard corner vortex does not entirely reach the salient corner of the channel entry (see figure 5-6). In the corner, a second vortex begins to appear. This vortex rotates in an opposite fashion to the rotation of the primary vortex. This behavior is a new observation and has not been found in previous experiments where strain rates are much lower. Because the strain rates of the fluid are so large in the bulk, even the secondary velocities are large enough to create a second stress singularity in the salient corner. This singularity gives rise to this tertiary flow pattern.

Figure 5-6. Transient images of the secondary vortex for the 0.3% PEO solution in the 16:1 contraction (De = 494). Images are taken every 200 ms.

To quantitatively characterize the entry flows, the vortex behavior of the 0.1% and 0.3% PEO fluid data is compared. The vortex lengths of the two solutions are plotted as a function of the Deborah number in figure 5-7. This data indicates a strong correlation between the viscoelastic vortex growth for both fluids. The dimensionless vortex lengths start at values close to the Moffat eddy length. As the Deborah number increases, both fluids begin to diverge from the Moffat length at the same critical Deborah number (De ~ 50). Both fluids experience vortex growth in a linear manner, and the slopes of this vortex length versus Deborah number are similar ($d\chi / d$De $= 0.0026$). This figure is compared with figure 5-8, which is a plot of the dimensionless vortex lengths against the Reynolds number. In this plot, there is no correlation between the two fluids: a clear indication that vortex enhancement is an elastic effect and not inertial in origin.
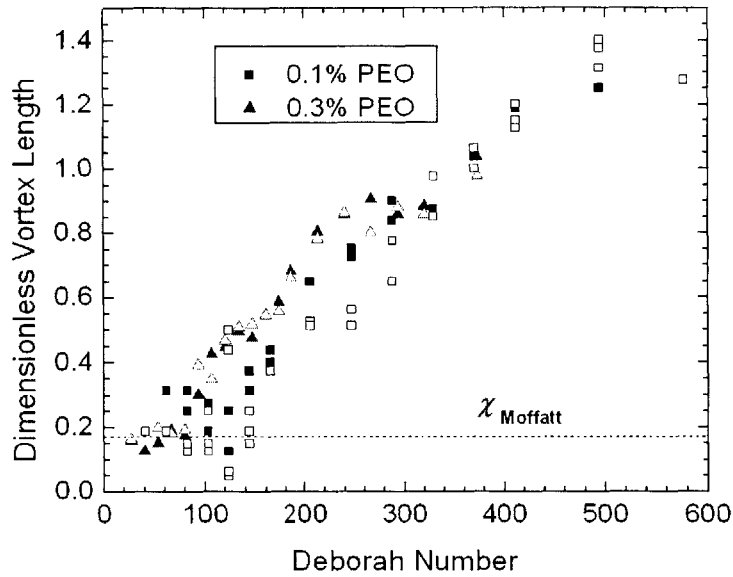
Figure 5-7. Dimensionless vortex lengths for both the 0.1% PEO and 0.3% PEO solutions. The vortex lengths of the two fluids appear to collapse onto a single line of slope 0.0026 (R^2 = 0.91)
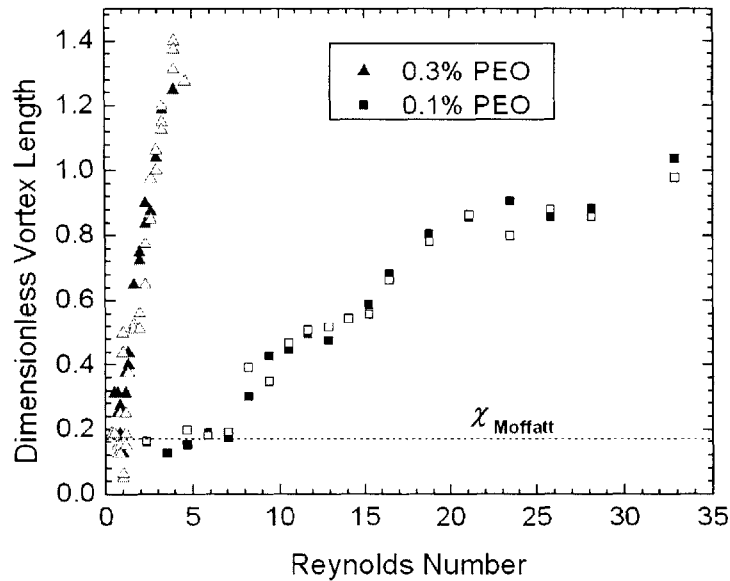
Figure 5-8. Dimensionless vortex lengths plotted against Reynolds number: no correlation is seen

The onset of non-Newtonian effects is typically marked by a departure from the simple laminar Newtonian behavior observed in the entry flow of water and similar fluids. In comparing the behavior of the 0.1% and 0.3% PEO solutions, streamlines first begin to depart from the laminar behavior at similar Deborah numbers. Vortex growth at higher

flow rates is also comparable in a qualitative nature. From these images it is possible to distinguish five distinct regimes of flow development (see section 6.1). The first region (De = 0 – 50) is defined by Newtonian-like flow convergence. Secondly, small flow divergences begin to develop (De = 50 – 60), but no vortex behavior is evident. The third region is characterized by the onset of unstable "lip" vortices (De = 60 – 125). These instabilities are only seen in the 0.3 % PEO solution, and are likely suppressed by inertial forces in the 0.1% PEO solution. In this region, for both solutions, flow patterns are unstable and give streak images the appearance that streamlines cross one another. The fourth region of flow development (De = 125 – 300) is the onset of stable corner vortex growth and eventually diverging flow. A fifth region of flow development (De > 300) is the vortex instability observed in the 0.3% PEO solutions.

5.1.4 4:1 Contraction

The 4:1 contraction (W_c = 50 μm: see table 3-1) was not used extensively in experimentation: streak images were taken for only the 0.3% PEO solution. Once again the flows began in a Newtonian fashion, however as the flow rates increased, vortex enhancement was never evident. Instead, flow instabilities began to occur that were marked by a pronounced secondary swelling (see figure 5-9) as has been seen in several previous studies (Cogswell, 1978; Chiba et al., 1990; Chiba et al., 1992). This is very similar to the diverging flow behavior in many axisymmetric studies (Cable and Boger, 1978), but the divergence occurs without the existence of a corner vortex as has typically been seen in axisymmetric flows. While no vortex behavior was observed in these channels, elastic instabilities did begin to form at the same Deborah number (De = 50) as in the 16:1 contractions despite the different geometry.
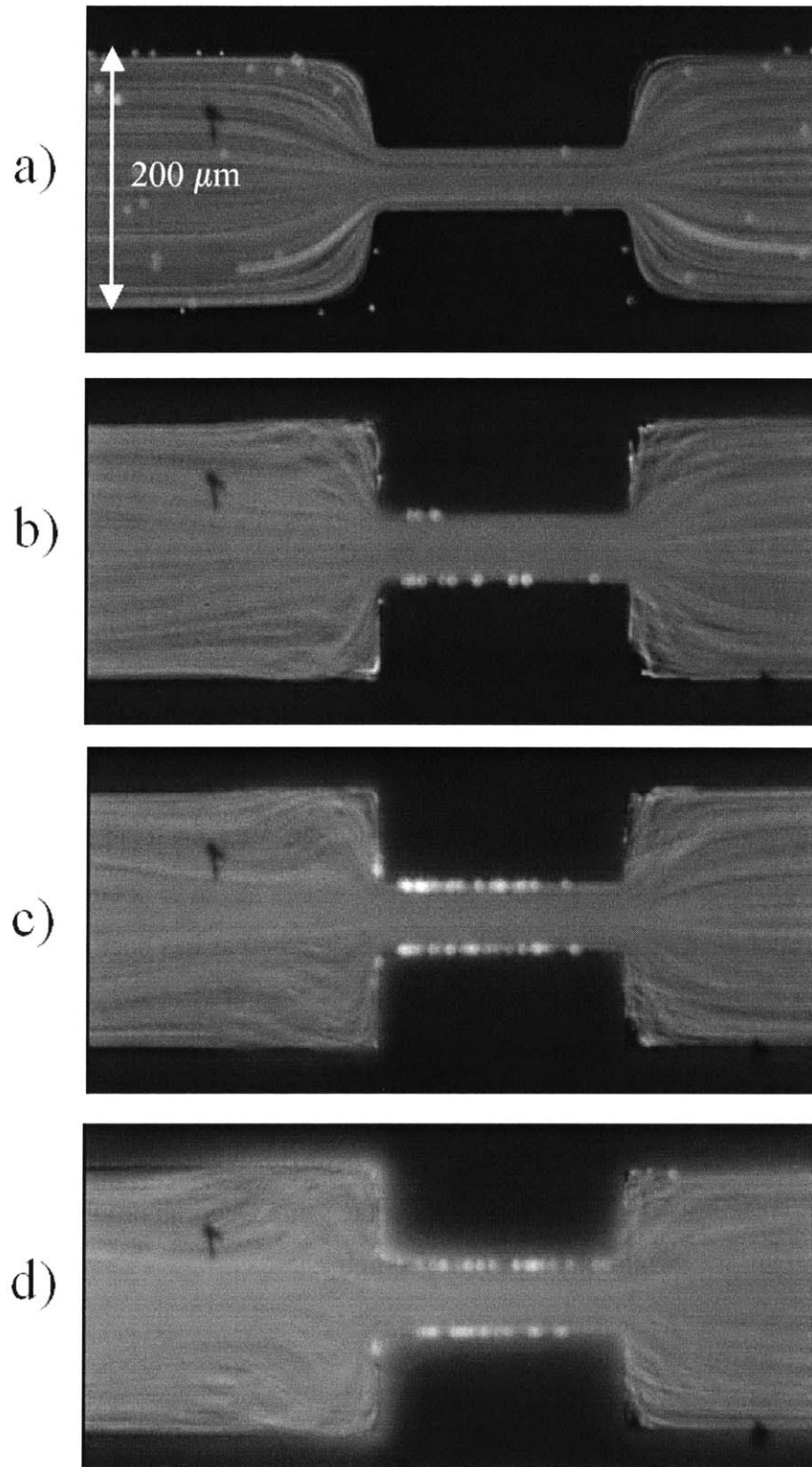
Figure 5-9. Streak images of the 0.3% PEO solution in a 4:1 contraction (200:50 μm) (El = 31.2). (a) De = 40, Re = 1.28 (b) De = 61, Re = 1.95 (c) De = 81, Re = 2.60 (d) De = 121, Re = 3.88

The elasticity number for the 0.3% PEO solution in the 4:1 contraction is El = 31. This value is larger that the associated elasticity number for the 0.1% PEO solution in the 16:1 contraction because the contraction width (W_c) is larger. The reason vortices are suppressed in this fluid is likely due to the significant effect of the upstream walls. The contraction ratio is not large enough to assume a 2-D sink flow, thus the channel walls confine the flow restricting the vortices from forming. Instead divergent flow develops in the entry region as a local response to extensional stresses near the centerline. This flow pattern seems to be a conflict between the elastic and inertial stresses, but the exact nature of the flows is unresolved.

5.2 Pressure Drop Analysis

5.2.1 Calculated Newtonian Pressure Losses

The goal of obtaining pressure measurements in the system was to determine the variation in the enhanced pressure losses caused by extensional thickening of the solutions, yielding an enhanced extensional viscosity for the fluid. To calculate the additional component of the pressure drop, it is necessary to determine the expected pressure loss for a Newtonian fluid in a rectangular channel. The pressure drop for a Newtonian fluid with the same shear viscosity as the zero-shear-rate viscosity ($\mu = \eta_0$) is calculated assuming Poiseuille flow in three rectangular channels (see figure 5-10). Two of the channels are identical (upstream and downstream of the contraction) and can be combined to give the total pressure loss:

$$\Delta P_{Newtonian} = \left(\frac{C_1 \mu Q L_1}{D_{h,1}^2 h W_1} \right) + \left(\frac{C_c \mu Q L_c}{2 D_{h,c}^2 h W_c} \right) \tag{5.1}$$

where L_1 is the length of the larger channels (3 mm each) and C_1 and C_c are shape factors for calculating additional pressure losses in rectangular channels (Fay, 1994):

$$C = f \, \mathrm{Re}_{D,h} \tag{5.2}$$

where f is the Darcy friction factor and $\mathrm{Re}_{D,h}$ is the Reynolds number using the hydraulic diameter (D_h) as the characteristic length scale:

$$D_h = \frac{4A}{P_R} \tag{5.3}$$

where P_R is the perimeter and A is the area of the channel. The shape factors, C_l and C_c, are determined to be $C_l = 82.5$ and $C_c = 61.9$ respectively from previous tabulated values (Fay, 1994). These shape factors are determined through numerical simulations for tabulation, but can be calculated for pipe flow ($C = 64$) and for an infinite plane ($C = 96$) from the Navier-Stokes equation. Clearly upstream and downstream the channels begin to approach the infinite plane limit. In the contraction region the channel is closely approximated by the circular shape factor due to the confinement of the walls.
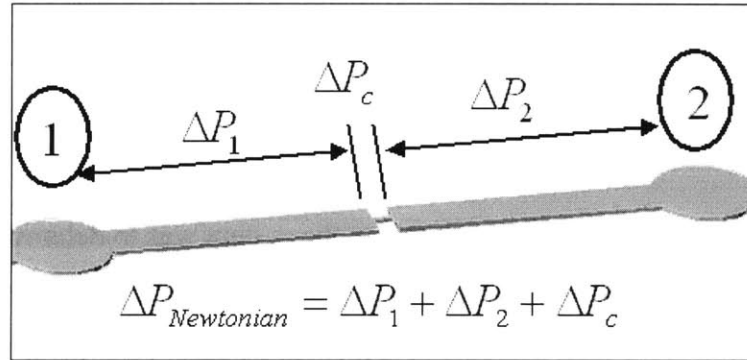
Figure 5-10. Pressure losses accrued between pressure taps

These equations are only valid if the entry length (L_e) is small compared to the length of the channel. This value was calculated by Vrentas and Duda (Vrentas and Duda, 1973) to be:

$$L_e = \frac{W_c}{2}\left(\frac{\mathrm{Re}}{9}+0.11\right) \tag{5.4}$$

This length is small ($L_e < 10\ \mu m$) compared with the contraction lengths for all fluids at low flow rates ($Q < 1.5$ m/hr). Compared to the $L_c = 400\ \mu m$ contraction, this entry length is never large ($L_e = 50\ \mu m$ for the 0.1% PEO solution at the maximum flow rate). However this could be a significant portion of the smallest contraction ($L_c = 50\ \mu m$) as flow rates increase. But for many of the non-Newtonian fluids, data shows that entrance

112

pressures dominate the pressure loss in this contraction region, making the pressure drop in the contraction negligible.

For Newtonian fluids, the additional pressure drop associated with the extensional viscosity is the Sampson pressure loss (Dagan et al., 1982), which is defined for a Newtonian fluid in an axisymmetric entrance as:

$$\Delta P_S = \frac{3\mu Q}{R_2^3} \tag{5.5}$$

In this expression the factor of 3 is derived from the extensional viscosity ($\eta_E = 3\mu$). Thus for a planar contraction the equivalent pressure loss would be:

$$\Delta P_S = \frac{8\mu Q}{W_c^2 h} \tag{5.6}$$

For all flows considered this value is small enough (see table 5-1) that the error of the pressure sensors (~5% for water) interferes with this measurement. The magnitude of this additional pressure drop is approximately 6% of the total pressure drop for the fluids considered in the smallest contraction length ($L_c = 50$ μm). Because this value is linear in viscosity and flow rate, it is a constant fraction of the total pressure loss in the system. This additional factor is not included in expected pressure because the difference between measured pressure and calculated values should equal this Sampson pressure drop, enabling the calculation of an extensional viscosity. The total pressure drop across the two pressure taps is:

$$\Delta P = \Delta P_s + \Delta P_1 + \Delta P_2 + \Delta P_c \tag{5.7}$$

L_c (μm)	$\Delta P_s / \left(\Delta P_1 + \Delta P_2 + \Delta P_c \right)$	
	16:1 (W_c = 25 μm)	4:1 (W_c = 50 μm)
50	9.55%	1.76%
100	6.75%	1.65%
200	4.25%	1.48%
400	2.44%	1.22%

Table 5-1. Sampson pressure drop as a percentage of total Poiseuille pressure drop for various channels and contraction ratios

5.2.2 Shear Thinning Effects

The effects of shear thinning on pressure losses are considered, even though the power-law index is close to unity. In this system, shear rates are extremely high and pressure losses can be greatly reduced from the Newtonian prediction (Koo and Kleinstreuer, 2003).

Pressure loses from a shear thinning fluid can be calculated only for a few well-defined shapes. Rectangular channels do not have any defined pressure loss equations, thus the system must be approximated using other shapes. For flow between two infinite planes, the pressure loss for a power-law fluid is defined as:

$$\Delta P_{PL,plane} = \left[\frac{Q(1+2n)}{2nWB^2} \right]^n \frac{mL}{B} \tag{5.8}$$

where n and m are the power law index and coefficient (see section 2.2), $2B$ is the separation of the planes, L is the length of the channels, and W is the thickness of the planes (Bird et al., 1987). For this equation to be valid, it is assumed that the width of the channel is much smaller than the height ($B \ll W$). For the microchannels in this study, the channel geometries are closer to squares than to infinite plates (especially in the contraction where the majority of the pressure loss occurs). Thus, a circular channel is considered, for which the pressure loss due to shear thinning is defined as:

$$\Delta P_{PL,pipe} = \left[\frac{Q(1+3n)}{\pi nR^3} \right]^n \frac{2mL}{R} \tag{5.9}$$

where R is radius of the pipe (Bird et al., 1987). A circular channel is useful to consider, because flow confinement in both direction is included in the calculations. For both of these approximations, the pressure loss data would not be specific to the microchannels in this study. To resolve this issue, the ratio of pressure loss that is due to shear thinning effects as compared to that of Newtonian fluids ($n = 1$) is determined. For an infinite plane channel, the resulting ratio is:

$$\frac{\Delta P_{PL,plane}}{\Delta P_{Newtonian}} = \left(\frac{\overline{v}}{B} \right)^{n-1} \left(\frac{1}{n} + 2 \right)^n \frac{m}{3\eta_0} \tag{5.10}$$

And for a circular channel the ratio of the power-law pressure loss to the Newtonian pressure drop is:

$$\frac{\Delta P_{PL,pipe}}{\Delta P_{Newtonian}} = \left(\frac{2\bar{v}}{D_h}\right)^{n-1} \left(\frac{1}{n}+3\right)^n \frac{m}{4\eta_0} \tag{5.11}$$

These ratios are multiplied by the calculated Newtonian pressure loss specific to each section of the channel (section 5.2.1). This gives an estimate of the effects of shear thinning for the channels (see figure 5-11). Both of the infinite planar cross section and the circular cross-section have the same effect on the calculated pressure losses (within 1%). Thus for convenience, and the accuracy of having flow confined, the circular estimate is used to calculate the shear thinning effects.
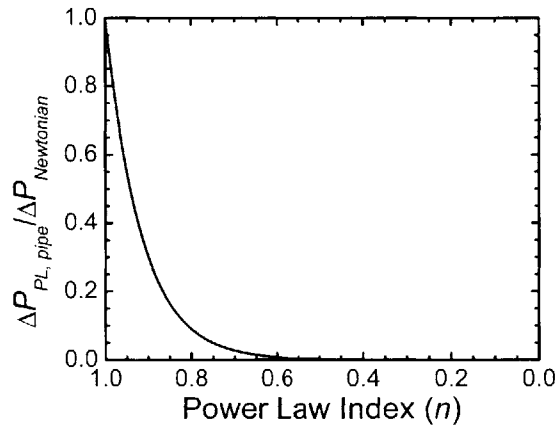
Figure 5-11. Pressure loss ratio for power-law fluid estimate compared with Newtonian fluid as a function of the power-law index (n) for channel of the same dimensions of the contraction ($W_c = 25$ μm, $h = 50$ μm).

A comparison of calculated pressure loss values for Newtonian and shear thinning fluids with the viscous properties of fluids considered in the present study (see table 4-4) are plotted in figure 5-12. Shear thinning has a large effect ($\sim 55\%$) on the expected pressure loss data for the 0.3% PEO solution for the channel with the longest contraction length ($L_c = 400$ μm), where shear thinning would have the largest effect. The effect is smaller for the 0.1% PEO solutions ($\sim 15\%$) but it is still a significant amount. While it may be somewhat inaccurate to extrapolate the power-law fluid data from rheological measurements to the shear rates considered in this geometry, it may provide a more accurate means of calculating expected pressure loss than the Newtonian estimate.
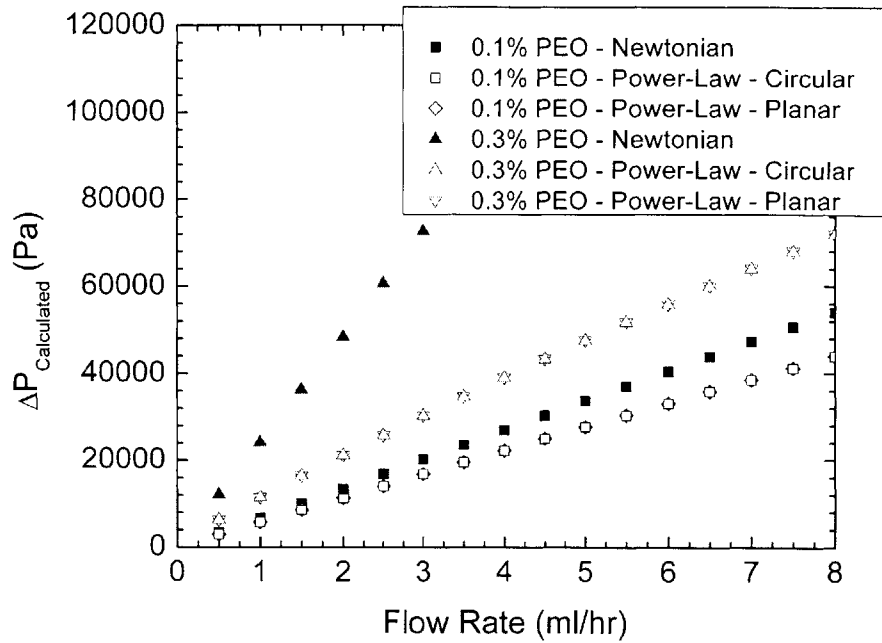
Figure 5-12. Comparison of the predicted pressure loss based on Newtonian and power-law analysis for 400:25:400 μm contraction/expansion (L_c = 400 μm) for the 0.1% and 0.3% PEO solutions. Pressure loss data for the circular and infinite planar cross section are indistinguishable.

5.2.3 Pressure Measurements

Pressure data was taken for the L_c = 50 μm, 100 μm, and 400 μm (see table 3-1) channels in the 400:25 μm contractions. The pressure measurements were taken over a range of flow rates (0 ml/hr < Q < 6 ml/hr) with a maximum measurable pressure of 200 kPa (see section 3.2.1). The mold that was used for all these channels was slightly damaged on the 200-micron contraction, so pressure data was not taken on these channels. Data for each channel was taken for water, the 0.1% PEO solution, and the 0.3% PEO solution. Experiments using these channels and the higher viscosity solution (0.1% PEO in glycerol/water solution) yielded primarily errant data, as deformation of PDMS became evident at moderate flow rates. Also with higher viscosity fluids, PDMS particles were pulled into the contractions repeatedly, clogging the contractions. As a result, a third non-Newtonian fluid was used: a solution of 0.05% PEO in water. The pressure data for this fluid was only measured for the L_c = 400 μm contraction. All of the raw pressure data is tabulated in the appendix.

For the DI water, the pressure drop was expected to increase linearly with the flow rate. In each channel the pressure drops were found to be approximately linear with flow rate (see figures 5-13 – 5-15) (see table 5-2), however the measured values are less than calculated pressure drops (see section 5.2.4 for explanation). The expected deviation due to extensional viscosity is indistinguishable for a Newtonian fluid. Thus, for Newtonian fluids, it is difficult to extract any quantitative extensional effects in the contraction.
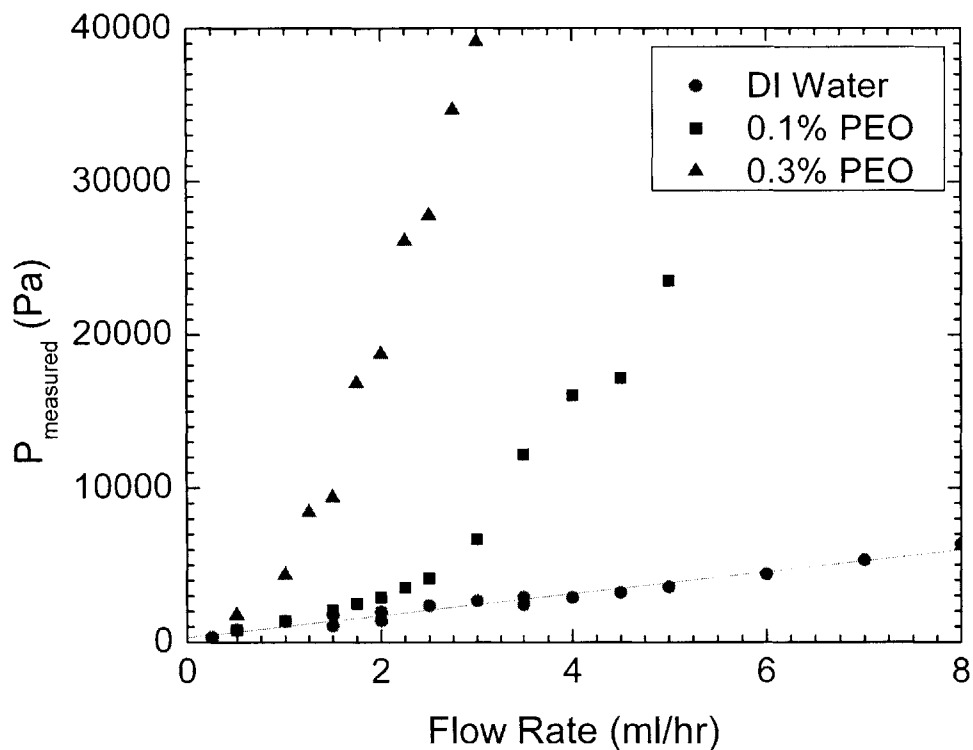
Figure 5-13. Measured pressure versus flow rate data for 400:25 μm contraction ($L_c = 50$ μm) for all fluids
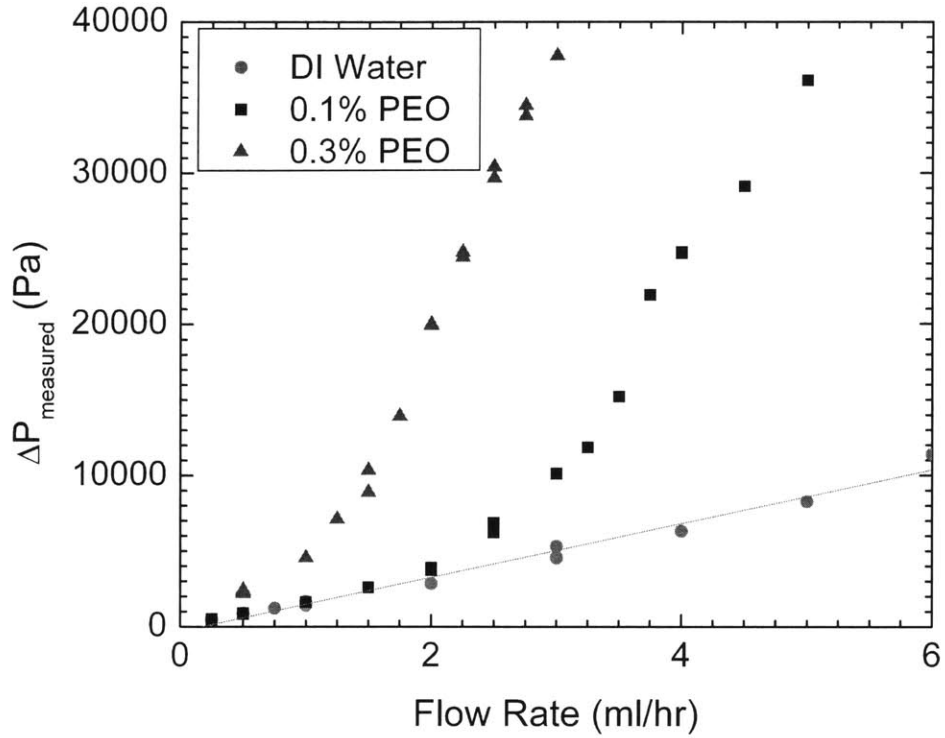
Figure 5-14. Measured pressure versus flow rate data for 400:25 μm contraction ($L_c = 100$ μm) for all fluids
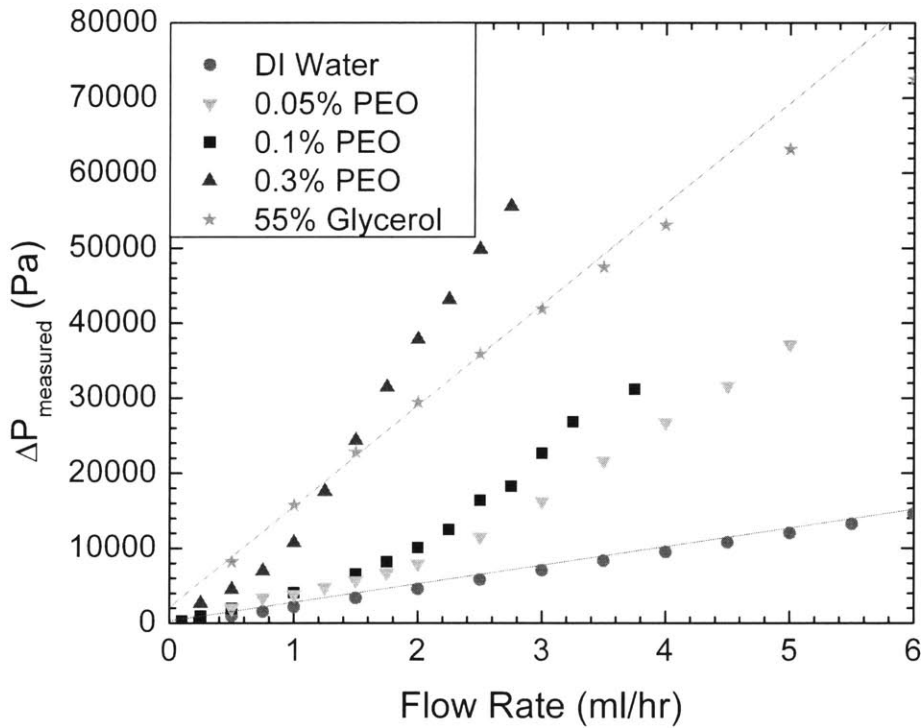
Figure 5-15. Measured pressure versus flow rate data for 400:25 μm contraction ($\underline{L_c} = 400$ μm) for all fluids

Channel	Fluid	L_c (μm)	$A \left(\dfrac{Pa \cdot hr}{ml} \right)$	B (Pa)	Range of Flow Rates (ml/hr)	R^2
16:1 (W_c = 25 μm)	Water	50	707.3	313.9	0 – 8	0.972
		100	1778.7	-302.0	0 – 6	0.981
		400	2478.3	322.2	0 – 7	1.000
	0.1% PEO	50	1356.7	63.4	0 – 1.75	0.992
		100	1651.7	48.6	0 – 1.5	0.996
		400	4451.0	210.4	0 – 1.5	0.998
	0.3% PEO	50	5237.3	-861.4	0 – 1	0.999
		100	4470.1	71.2	0 – 1	0.994
		400	8638.0	389.7	0 – 0.75	0.993
	0.05% PEO	400	3725.2	248.1	0 – 2	0.988
	55% Glycerol + Water	400	13437	2141.2	0 – 3	0.998
57 μm	Water	0	5131.0	1393	0 – 10	0.997
	0.1% PEO	0	7531.6	3058	0 – 10	0.995
	0.3% PEO	0	12970	7470	0 – 5	0.996

Table 5-2. Linear fits for pressure data across 16:1 contractions and straight channel (W_j = 57 μm)

For the elastic polymer solutions there are more interesting responses in the pressure-flow rate dependence. For the 0.1% PEO solution the pressure data is linear until a flow rate between 2 – 3 ml/hr depending on the contraction (see table 5-2). Above this flow rate the pressure drop appears to increase in a non-linear manner. This flow rate corresponds to a Deborah number of approximately De $\approx$50: the same Deborah number at which elastic effects were observed in the streamlines of the 0.1% PEO solution in the streak images. As the flow rate increases, the pressure loss grows well beyond expected Newtonian results. This is a clear sign of extensional thickening behavior in the fluid.

For the 0.3% PEO solution the behavior was very similar to that of the 0.1% PEO solution, however the onset of the extensional thickening was observed at lower flow rates, as is anticipated. The pressure drop begins to increase at a flow rates between Q = 0.5 and Q = 1 ml/hr. Once again this translates into a Deborah number of approximately De $\approx$50. The pressure drop in the 0.3% PEO solution increases more quickly than the 0.1% PEO solution when extensional thickening occurs. From the raw data, it is unclear

as to whether this effect is due to the higher shear viscosity of the fluid or due to a greater extensional viscosity.

A 0.05% PEO solution was also examined in the 400-micron contraction. Even though this solution is more dilute than the 0.1% PEO solution, the relaxation time is not significantly smaller than the 0.1% PEO solution ($\lambda = 1.5$ ms compared to $\lambda = 1.6$ ms: see table 4-4). The similar relaxation time was determined to be a result of the concentration of the 0.05% PEO solution being below the critical concentration (c^*). For this fluid the pressure loss behavior is comparable to that of the 0.1% PEO solution (figure 5-15), however the pressure increase is more gradual (as is expected due to the lower shear viscosity).

5.2.4 Pressure Measurement Validation

One of the major errors in the pressure data was the inconsistency of the acquired values. Pressure sensors were statically calibrated using columns of water (see figure 3-8), however, measured pressure drops did not agree with computed pressure drops for most of the channels observed, even for Newtonian fluids. Likely the errant pressure measurements were due to air bubbles trapped in various portions of the tubing in the pressure taps. Despite the errors, pressure values were close to predicted values (within 20% for water), however it is difficult to actually predict measured values for the non-Newtonian fluids because the shear rates ($\dot{\gamma} \sim 50,000$ s^{-1}) are beyond those measured by the rheometer ($\dot{\gamma} \sim 1000$ s^{-1}). Another source of error is from three-dimensional effects. The values of the shape factor (C) are only estimates for straight channels. In these microchannels, other effects may also distort pressure measurements (such as the large circulations zones at the expansion).

The shape factors were considered as possible sources of pressure error. The minimum shape factor ($C_{square} = 56.9$) and maximum ($C_{plane} = 96$) generate a range of possible pressure losses for such geometries. These ranges are plotted in figure 5-16 and compared with the measured pressure drop for water in each contraction length. Only the data for

the L_c = 50 μm contraction lies within the range of pressure losses, although the L_c = 100 μm and L_c = 400 μm contractions are close to the limits (within 10%). However, these do not appear to be close to the same limit: the data for the L_c = 100 μm contraction is close to the upper limit while the L_c = 400 μm contraction is close to the lower limit. Based on these observations, it would be impossible to conclude that any shape factor discrepancy is responsible for the errant pressure measurements.
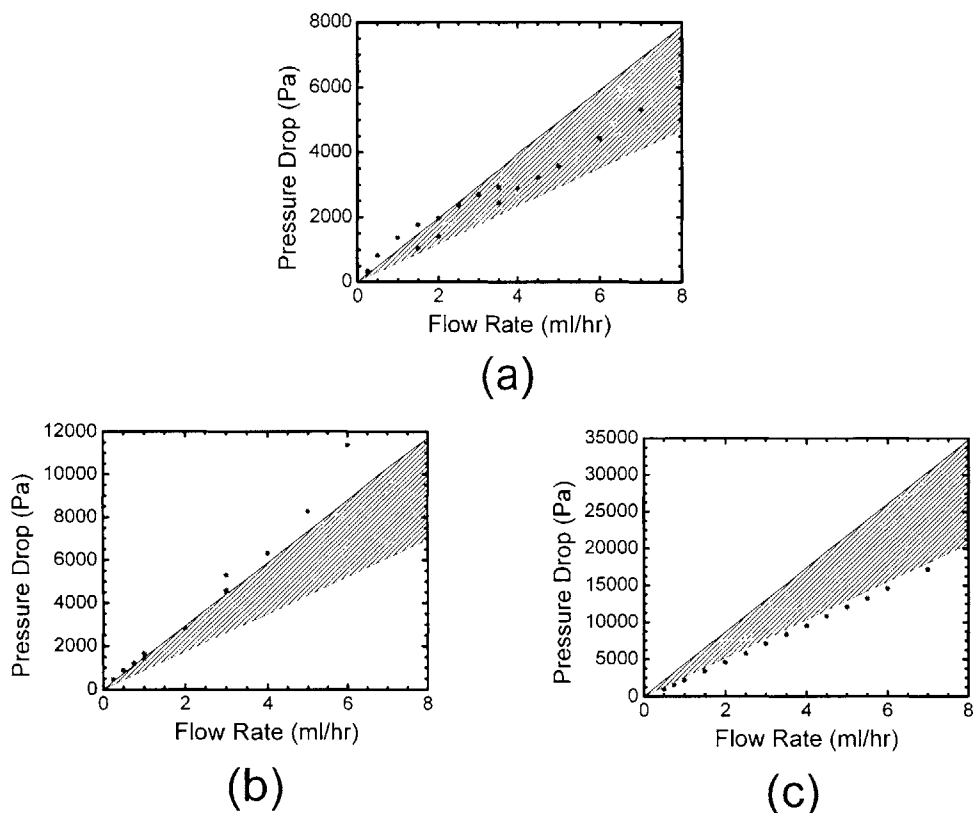
Figure 5-16. Range of pressure drops for maximum shape factor (C = 96) and minimum (C = 56.9) compared with the actual pressure loss data for DI water in each contraction (a) L_c = 50 μm (b) L_c = 100 μm (c) L_c = 400 μm

5.2.4.1 Hole Pressure Error

The possibility that hole pressure error could be effecting the pressure measurements is incorrect. Hole pressure ($P*$) is a difference between actual wall pressure and measured pressure:

$$P* = P_{1,h} - P_{1,w} \qquad (5.12)$$

where $P_{1,w}$ is the pressure measured by a flush-mounted traducer, and $P_{1,h}$ is the pressure measured by a recessed transducer (see figure 5-17). This discrepancy is derived from the normal stresses in the fluid, which cause streamlines to bend as they pass over pressure holes. The tension in the streamlines causes a tensile stress to be exerted over the holes in a channel, causing the transducers to measure a lower pressure than the actual pressure in the bulk flow. Fortunately the magnitude of this error is consistent with the size of the hole.
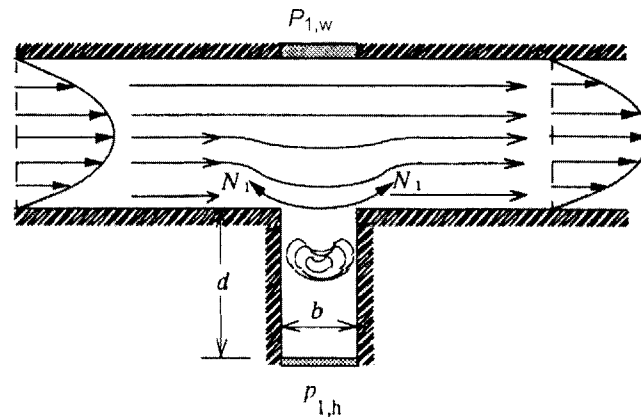
Figure 5-17. Hole pressure effect: tension in streamlines cause recessed pressure sensors ($P_{1,h}$) to read less than that of a flush mounted transducer ($P_{1,w}$) (picture source: (Macosko, 1994))

The other important factor for pressure hole measurements is inertial effects. Inertia works in an opposite manner, causing pressure sensors to read higher than the actual pressure in the channel. It has been determined (Joseph, 1990) that this viscoelastic effect is more important when:

$$d_c < \left(\frac{\lambda \left(\eta_0 - \eta_s \right)}{\rho} \right)^{\frac{1}{2}}$$

(5.13)

However, this does not necessarily translate to inertial or viscoelastic effects being large, it is only a comparison of the relative magnitude of each value.

The measured hole pressure error is related to the first and second normal stress differences (N_1 and N_2) for a circular hole (Higashitani and Pritchard, 1972):

$$P^* = -\frac{1}{3} \int_0^{\tau_w} \frac{N_1(\dot{\gamma}) - N_2(\dot{\gamma})}{\tau_{12}(\dot{\gamma})} d\tau_{12} \qquad (5.14)$$

This has been simplified in terms of the normal stress difference (Tanner and Pipkin, 1969; Tanner, 1985):

$$P^* = -\frac{N_1(\dot{\gamma})}{5} \qquad (5.15)$$

However, because the shear rates at the upstream and downstream pressure taps are equivalent, the normal stresses are equal. Thus, the hole effect cancels itself out for differential pressure measurements.

5.2.4.2 Repeatability

In order to ensure the pressure loss is repeatable, three trials were run using the 0.1% PEO solution in the $L_c = 400$ μm contraction (see figure 5-18). The pressure measurements were consistent for each trial. At low flow rates, the pressure varies by as much as 100%, but this error is due to the accuracy of the pressure sensor: this error is constant at approximately 1000 Pa (two standard deviations). At high flow rates ($1 < Q <$ 3.5), the range of measured pressures drops for each were within this 1000 Pa error. The pressure data was taken using different PDMS channels (but still off the same mold), and small-scale feature differences formed in the fabrication process (curing times, channel smoothness, and plasma exposure: see section 3.2) likely changed the onset of specific vortex behavior at higher flow rates.
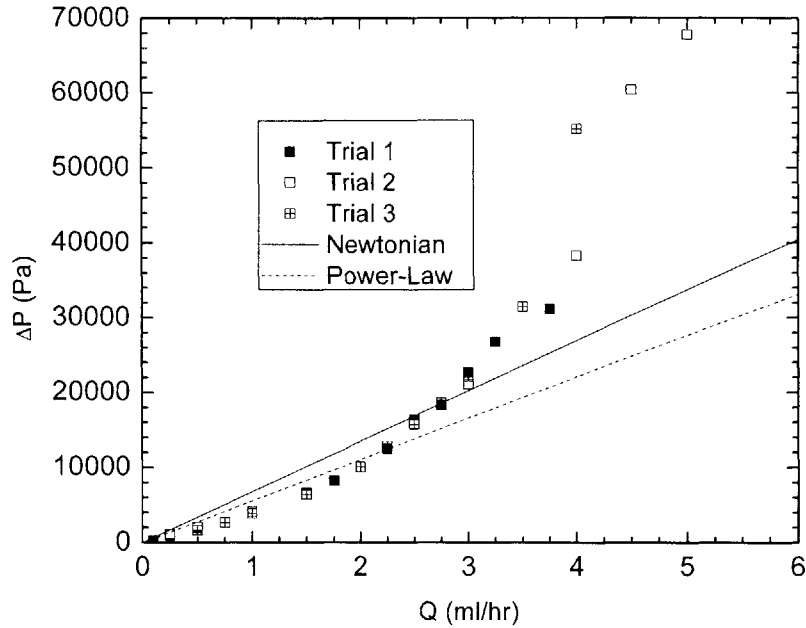
Figure 5-18. Pressure measurements are conducted on three different trials using the L_c = 400 μm contraction for the 0.1% PEO solution to show repeatability for the same fluid and geometry. Measured pressures are compared with Newtonian and power-law calculations.

5.2.4.3 Straight Channel

To verify that the source of pressure loss was actually due to the resistance to extension from the polymer solution, pressure drop measurements were made across a straight channel. The channel was 57 microns in width, 50 microns in height, and 6 millimeters in length (AR = 0.88, D_h = 52.3 μm, C = 57.5). The resulting pressure drop should be:

$$\Delta P_{Newtonian} = f\rho\left(\frac{Q}{hW_1}\right)^2\left(\frac{L_1}{D_h}\right) \quad (5.16)$$

(see section 5.2.1). Pressure data was taken across this contraction for DI water, the 0.1% PEO solution, and the 0.3% PEO solution. The pressure drop data is plotted in figure 5-19 against the flow rate. The data is compared with Newtonian estimates for the same channel and the power-law prediction for the channel. The pressure loss is approximately linear for each of the fluids as is desired; indicating that the pressure loss observed in the previous sections is clearly owed to the extensional effects associated with the entrance flow and not any wall shearing effects from the microchannels. However, the Newtonian

124

and power-law approximation do not accurately calculate the expected pressure losses for the non-Newtonian solutions.
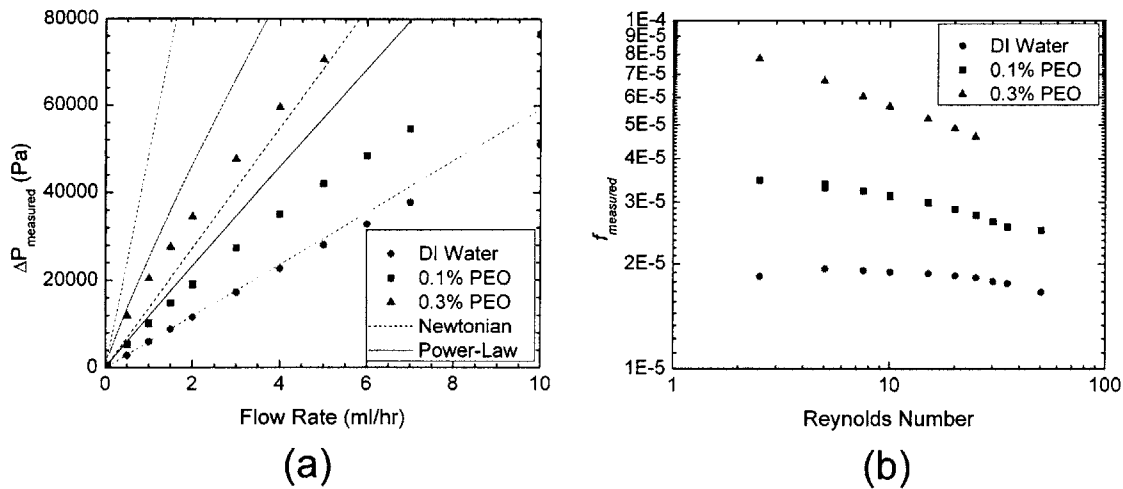
Figure 5-19. (a) Pressure loss data for a W_1 = 57 μm straight channel. Measured data is compared with Newtonian and power-law predictions for pressure drop. (b) Darcy friction factor (f) is plotted against Reynolds number

5.2.4.4 Second Newtonian Fluid

To test the accuracy of the pressure sensors, tests were run on a second Newtonian fluid (55% glycerol and water mixture). For this fluid the viscosity was 8.59 mPa·s, so one would expect that the pressure drop would increase by a factor of 8.6 from the data for water. A trial was performed for the 400-micron contraction to measure this pressure loss. The data was close to linear as is expected (see figure 5-15), but the slope of the resulting pressure-flow rate data is less than 8.6 times that of water (see table 5-2). At higher flow rates the pressure begins to diverge from the initial linear increase, however this is attributed to microchannel deformations caused by the large pressure (greater than 50 kPa) within the channels. Thus, only the initial pressure-flow rate slope (0 – 3 ml/hr) is considered: the data indicates that the slope of the glycerol-water mixture is only 5.4 times the values for the water in the same channel.

125

5.2.5 Normalized Pressure Data

By normalizing the measured pressure drop with respect to the predicted pressure drop for a Newtonian fluid, it is possible to determine the accuracy of the measurements relative to these predictions (figure 5-20). For the $L_c = 50$ μm contraction the pressure data agrees with predictions at the higher flow rates. However at the lower flow rates, the pressure drop appears to be larger than the predicted pressure loss. However, this error is magnified by the small magnitude of these pressure losses ($\sim$ 1000 Pa) compared to the error of the system ($\sim$ 1000 Pa). For the $L_c = 100$ μm contraction a similar error is observed. The measured data once again appears linear with the Reynolds number (figure 5-14) but does not agree with normalized predictions. At the longest contraction ($L_c = 100$ μm) length the pressure-flow rate dependence is nearly linear. The dimensionless pressure loss is approximately constant with the Reynolds number.
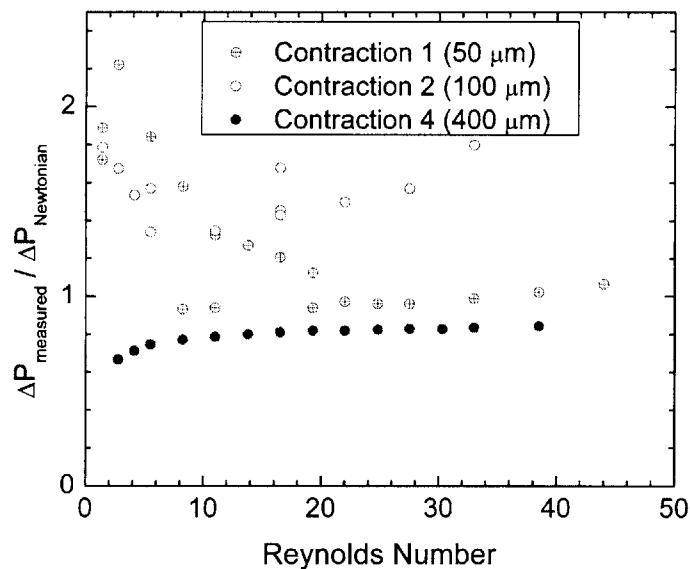
Figure 5-20. Normalized pressure data (with respect to the Newtonian prediction: equation (5.1)) for the DI water in each contraction

The normalized pressure loss data is plotted against the Deborah number in figure 5-21 for the 0.1% PEO solution. From the Newtonian normalization, it appears that the pressure loss is less than calculated by about 40%. However, it is clear from these graphs

that the onset of extensional effects occurs at the same Deborah number ($De \gtrsim 50$) for each contraction: a good indication that the vortex growth behavior is repeatable.
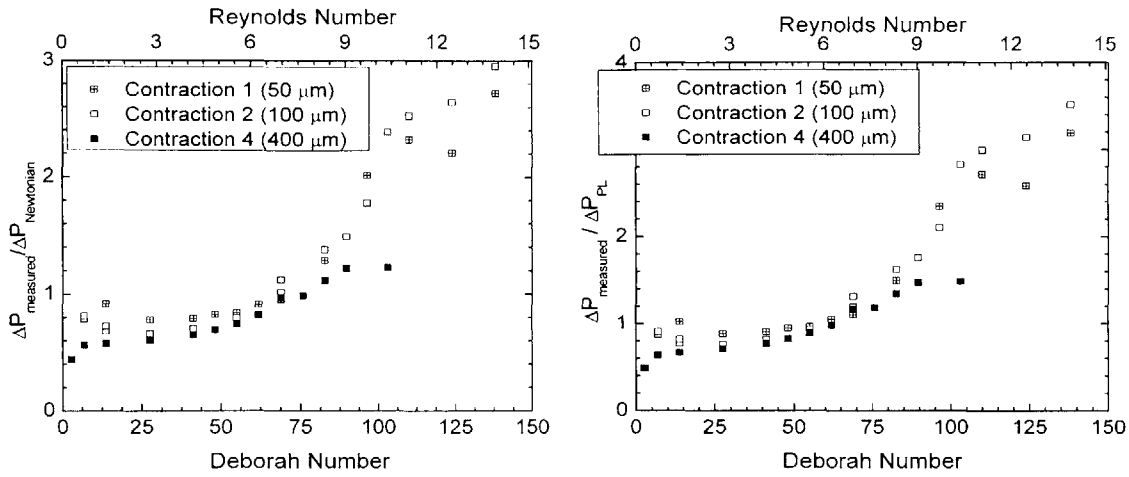
Figure 5-21. Normalized pressure data for the 0.1% PEO solution in each contraction. Pressure is normalized against the Newtonian prediction (equation (5.1)) (left) and the power-law prediction (from equation (5.10)) (right)

To compensate for the offset in the pressure loss, the shear thinning assumptions (using the values of n and m in table 4-4) were incorporated into the calculated pressure loss (equation (5.11)). Including shear-thinning effects improves the accuracy of the measured values, however error still exists at low flow rates where the normalized pressure drop should be unity. The lack of a direct correlation between predictions and measured values will become important in section 5.3 when extensional viscosities are calculated.

For the 0.3% PEO solution, again the critical Deborah number agrees with the onset of vortex behavior from the streak images (De = 50) (see figure 5-22). As the length of the contraction increases, the normalized pressure drop decreases. This is because the entrance pressure loss should be constant regardless of the length of contraction. As the contraction gets longer, the percentage of the total pressure loss that is attributed to the entry pressure loss decreases.

127
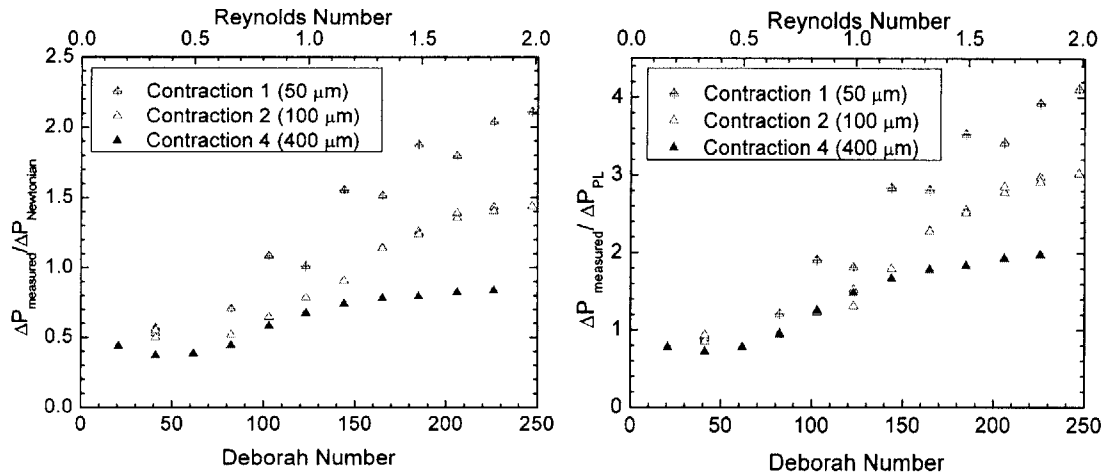
Figure 5-22. Normalized pressure data for the 0.3% PEO solution in each contraction. Pressure is normalized against the Newtonian prediction (equation (5.1)) (left) and the power-law prediction (from equation (5.10)) (right)

Once again the data was also compared with shear thinning data of a power-law fluid for the 0.3% PEO solution (figure 5-22). This normalization improved the agreement between the measured values and predicted values, and the same trends are observed as the normalized Newtonian result. The pressure increase associated with elastic effects occurs at a Deborah number that correlates with the onset of extensional thickening in the 0.1% PEO solution.

Because both the normalized pressure drop and the power-law pressure drop fail to accurately account for the pressure drop across the channel, a third technique was employed to normalize the data. The measured pressure loss, in the region in which flow was steady and pressure drop was linearly related to the flow rate, was fit to a line. The expected pressure loss is extrapolated about this initial Newtonian-like pressure loss pattern such that:

$$\Delta P_N = AQ + B \tag{5.17}$$

where A and B are variables used to linearize the pressure drop at low flow rates. The pressure data is now normalized about this initial pressure loss, as shown in figure 5-23 (see table 5-2 for tabulated values of A and B).
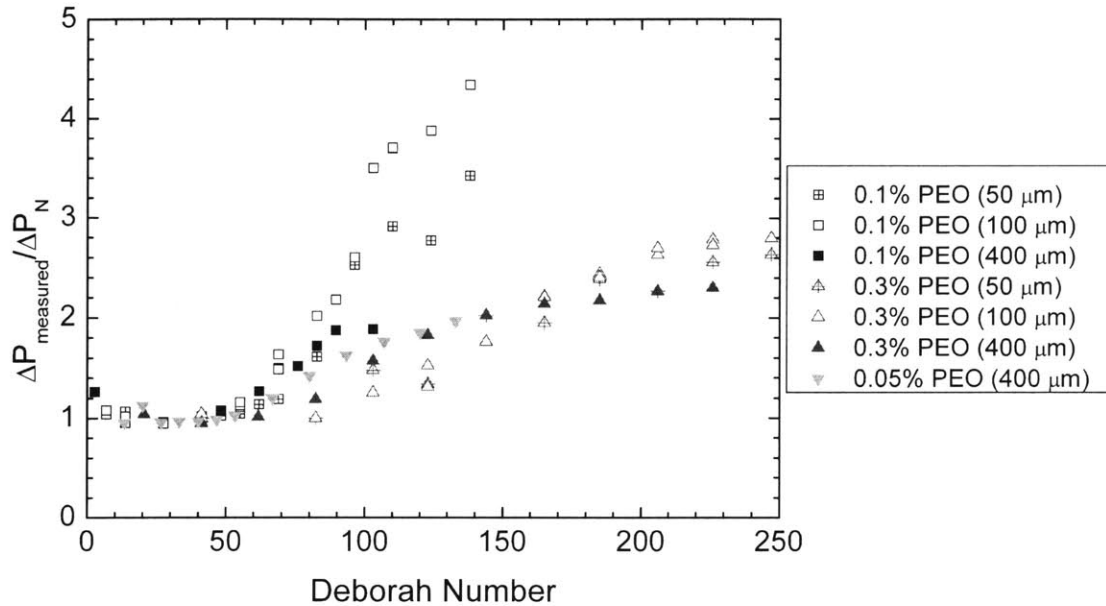
Figure 5-23. Pressure loss normalized by the tangential pressure drop from the linearly increasing region

Figure 5-23 indicates that the onset of extensional behavior occurs at comparable Deborah numbers for each viscoelastic fluid in each contraction, but the actual entrance pressure increase is not constant: it depends on the length of the contraction (L_c) and the Deborah number. Thus the extensional effects of the different fluids are not the same. Another reason why this data does not collapse onto one line is due to the inertial effects on the system. For the more viscous solutions, the Reynolds numbers are much smaller than for less concentrated solutions.

5.3 Extensional Viscosity

5.3.1 Cogswell's Analysis

For these experiment it is possible to extrapolate to a zero-length contraction to evaluate the effects of entry pressure loss (ΔP_{en}). However, there is also a component of the pressure drop that is a function of the upstream and downstream channel flow. Since the fluids are approximately Newtonian, it would be easy to factor this term out if the pressure drops were consistent with Newtonian predictions. However, since pressure

drops do not completely agree with calculated values, another means of determining the entrance pressure loss must be analyzed.

Once again the extrapolated linear pressure drop is used as the Newtonian pressure drop (ΔP_N). Additional contributions to the pressure drop are calculated from the divergence from this extrapolated pressure loss line. Based on flow visualization, it is determined that this entry pressure drop is the dominant source of pressure loss, as there are little exit effects. Thus the calculated entry pressure is:

$$\Delta P_{en} = \Delta P_{measured} - \Delta P_N \qquad (5.18)$$

From this calculation it is possible to proceed with Cogswell's analysis. However, there are still several key problems with the analysis.

For most experiments performed using Cogswell's method the working fluid has been a polymer melt, not a polymer solution. The difference is that polymer solutions typically have larger increases in extensional viscosities than polymer melts (Tirtaatmadja and Sridhar, 1993). The equation for strain rate of a fluid (equation (2.21)) using Cogswell's analysis predicts that the strain rate is dependant on the product of the wall stress ($\tau_w \sim Q^n$) and the shear rate ($\dot{\gamma} \sim Q$) divided by the entry pressure drop. Thus this predicts that the strain rate ($\dot{\varepsilon}$) will actually decrease with flow rate if the entrance pressure increases such that:

$$\Delta P_{en} > Q^{n+1} \qquad (5.19)$$

Thus, for the present system, in which the entrance pressure loss is large, the predicted strain rate would decrease as the flow rate increases.

Also a clear indication of the errant usage of Cogswell's technique in this problem is the prediction of the convergence angle for Newtonian fluids. From the images in section 5.1.1 (see figure 5-1), it is clear the convergence angle in the entry region is not 37° as predicted for Cogswell's method (see equation (2.26)). Finally, a last problem with Cogswell's analysis for this current system is that inertial effects are not negligible. Reynolds numbers are typically above unity for these flows, whereas in Cogswell's

analysis and most of its applications, the Reynolds numbers are essentially zero. As a result, another means of calculating the extensional viscosity is required.

5.3.2 Apparent Extensional Viscosity

Because Cogswell's analysis falls short of explaining the pressure loss data for these polymer solutions, it is necessary to evaluate the extensional viscosity by other means. Thus, the analysis of Metzner and Metzner was employed to try to quantify the extensional behavior (Metzner and Metzner, 1970). This analysis was originally employed to estimate the apparent extensional viscosity of dilute polymer solutions, so it is an appropriate measure for present analysis. It is only an approximation, because shear effects are neglected and strain rates are only calculated through an approximation: ($\dot{\varepsilon} = 2\overline{v}/W_c$). Their analysis also assumes that the entire pressure loss is derived from extensional effect (equation (2.20)), so the resultant values are somewhat flawed. However, the increases in entry pressure is an extensionally-dominated effect so these estimates are practical.

From the pressure data, the entrance pressure loss is determined by subtracting the tangential data at low flow rates from the measured data using equation (5.18) and the data in table 5-2. Thus for low flow rates the measured apparent extensional viscosity is only the scatter of the points about the prediction and should be ignored. However, at higher flow rates (De > 50), when the pressure drop data diverges from this tangential prediction the apparent extensional viscosity grows rapidly (see figure 5-24). It is also worth noting the magnitude of the strain rates achieved in figure 5-24. These values ($\dot{\varepsilon}$ > 50,000 s^{-1}) are larger than others have been able to achieve in entry flow problems without inertial effects dominating (Walters and Rawlinson, 1982; Evans and Walters, 1986; Chiba et al., 1990; Quinzani et al., 1995). They are also several times greater than the strain rates obtained in many opposed jet rheometers ($\dot{\varepsilon}$ ~ 20,000 s^{-1}) (Cooper-White et al., 2002).

131
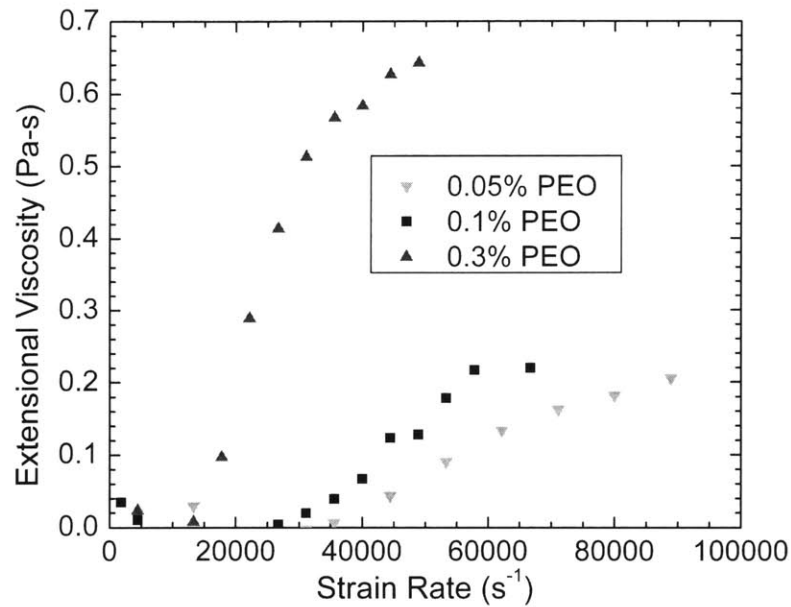
Figure 5-24. Apparent extensional viscosity plotted against strain rate for the 0.05% PEO, 0.1% PEO, and 0.3% PEO solutions as calculated for the 400-micron contraction

The apparent Trouton ratio is determined based on the zero-shear-rate viscosity of the fluids and plotted against Deborah number (figure 5-25):

$$Tr_a = \frac{\eta_{P,a}}{\eta_0} \tag{5.20}$$

The results for the 0.1% PEO and 0.05% PEO solutions agree quite well. However, the results for the 0.3% PEO solutions are somewhat different. The Trouton ratio does not reach the same magnitude as the other polymer solutions. The reason for this is most likely connected to the concentration of the solution compared to the critical concentration ($c*$). Because the 0.3% solution is about 4 times the critical concentration, the fluid is in the semi-dilute regime (see section 4.1.1). It has been well documented that the growth of the extensional viscosity of semi-dilute solutions is not as dramatic as that of dilute solutions (Tirtaatmadja and Sridhar, 1993).
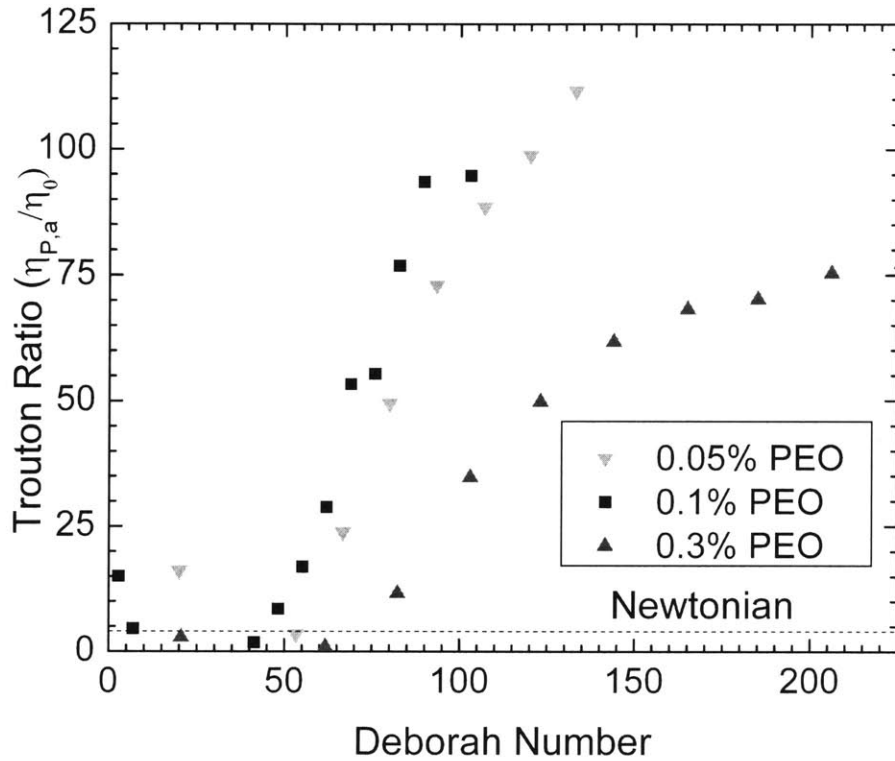
Figure 5-25. Trouton ratio plotted against Deborah number for 0.05% PEO, 0.1% PEO, and 0.3% PEO solutions as calculated for the $L_c = 400$ μm contraction

The Trouton ratio is again plotted for each contraction length based on the specific solution (figures 5-26 and 5-27). The data on these plots should superpose, as the same fluid is being used for each trial. However, the longer contraction lengths have larger apparent extensional viscosities (or Trouton ratios) than the small contraction lengths for the same Deborah number. This is true for both solutions but the phenomenon is more evident for the 0.3% PEO solution. Likely, this error is due to the small sample size used for extrapolation of the linear range of pressure drop (see table 5-2). With a greater range of data, the error would likely be reduced such that the graphs of Trouton ratio versus time would collapse onto one for each solution.
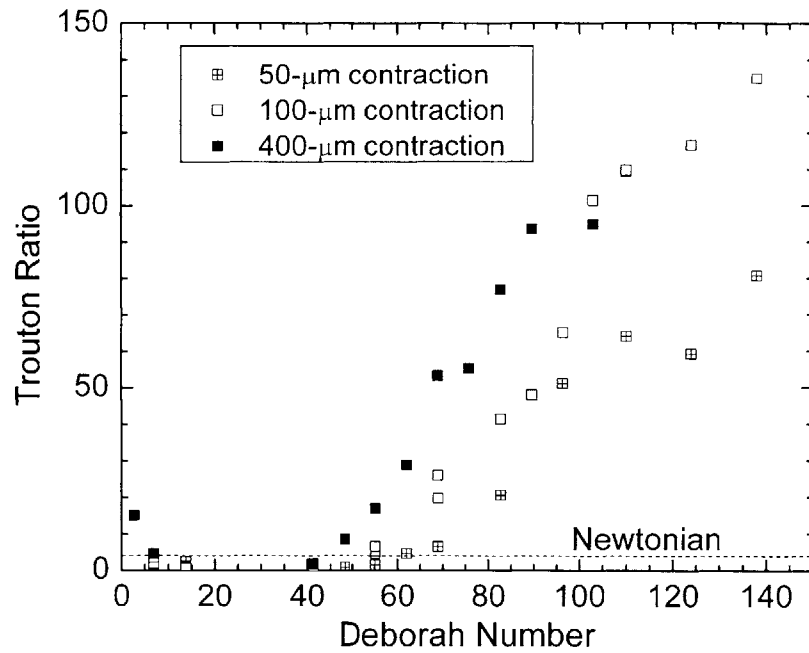
Figure 5-26. Trouton ratio plotted against Deborah number for the 0.1% PEO solution in each contraction
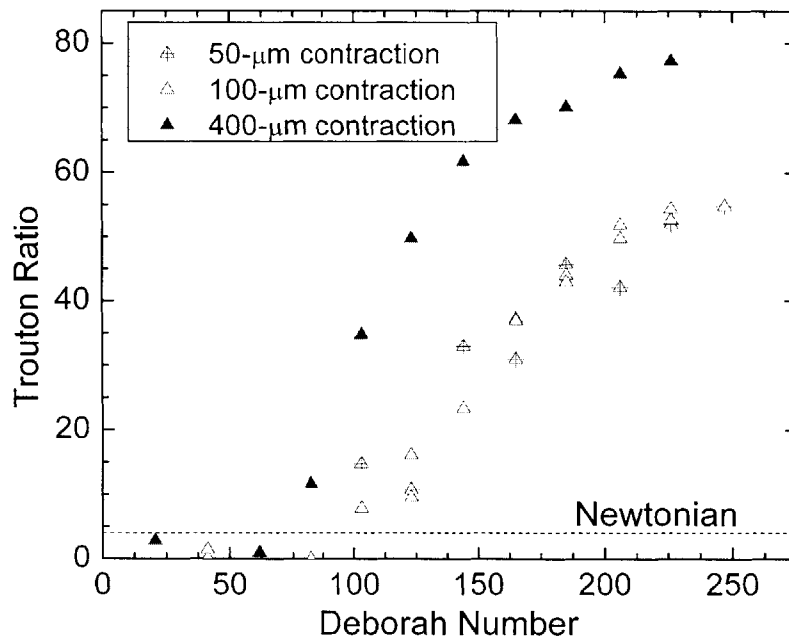
Figure 5-27. Trouton ratio plotted against Deborah number for the 0.3% PEO solution in each contraction

134

From the graphs of the apparent extensional viscosity it is possible to make several conclusions about the nature of the PEO solutions. First, each solution experiences significant extensional thickening entering the contraction. The extensional viscosities increase by nearly two orders of magnitude above the zero-shear-rate viscosities. Secondly, the concentration of the solution has a large effect on the resulting Trouton ratio. Dilute solutions of PEO experience a larger increase in the Trouton ratio than the semi-dilute solutions at comparable Deborah numbers. Also, the critical Deborah number (De = 50) for the onset of elastic behavior (both increased pressure drop and enhanced vortex behavior) in the planar contraction is larger than previous experiments had been able to generate (Walters and Rawlinson, 1982; Evans and Walters, 1986; Nigen and Walters, 2002). As a result these previous studies failed to observe vortex growth in their experiments with constant viscosity fluids. Lastly, the onset of extensional thickening corresponds with the onset of vortex behavior in the flow visualization, thus it is possible to conclude that the elasticity of the fluids is the driving force for the development of such secondary flow growth.

5.3.3 Residence Time

The total residence time of the different fluids in the contraction is examined as a source of the higher Trouton ratio in longer contractions. The residence time for the fluid in the contraction (t_c) is defined based on the average velocity:

$$t_c = \frac{L_c}{\overline{v}_c}$$

(5.21)

From this value it is possible to calculate a dimensionless measure of the total residence time. The residence Deborah number (De_r) is a comparison of the time in the contraction to the total relaxation time of the fluid:

$$De_r = \frac{\lambda}{t_c} = \frac{\lambda \overline{v}_c}{L_c} = De \frac{L_c}{W_c}$$

(5.22)

If this value is less than unity, the fluid has time to relax while it is in the contraction. However, for residence Deborah numbers greater than unity, the fluid will not have returned to its original random configuration. Whether the fluid is exiting the contraction

in its extended state or in a relaxed state could affect the pressure drop across the contraction (see figure 5-28) (Tanner, 1985). Figure 5-29 shows a plot of this residence Deborah number against the flow rate for the 0.1% PEO and 0.3% PEO solutions in the shortest and longest contractions.
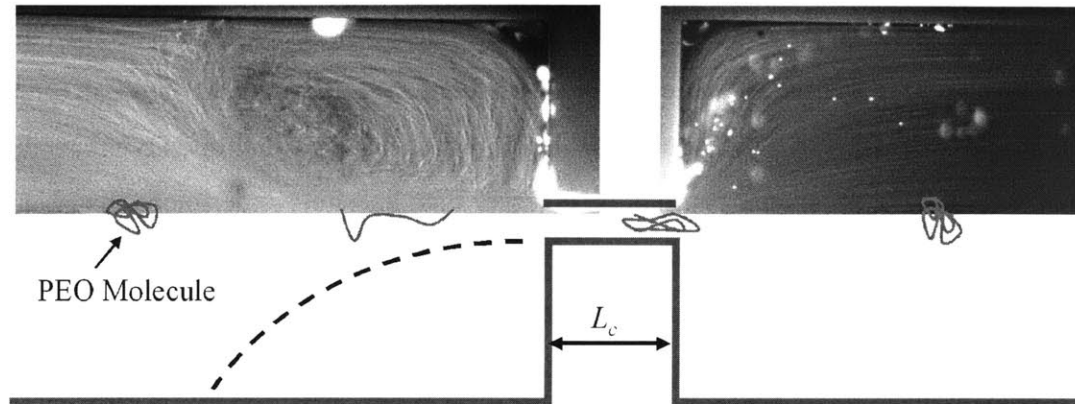
Figure 5-28. Schematic showing the extension and relaxation of a polymer across the contraction.
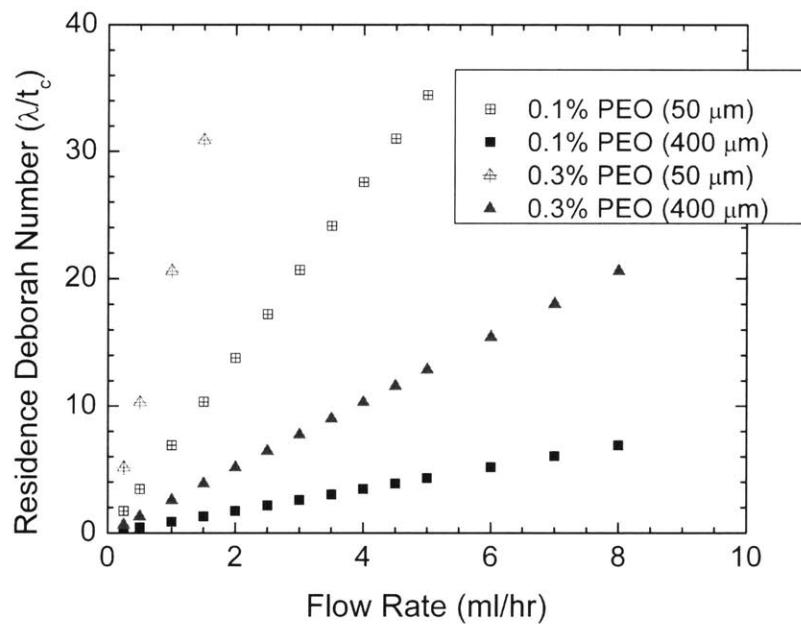
Figure 5-29. Dimensionless residence times (De$_r$) plotted against flow rate for the 0.1% PEO and 0.3% PEO solutions

From figure 5-29 it is clear that these fluids are only within the contractions for very short times ($t_r < 100 \ \mu s$), at the flow rates of interest. This is substantially smaller than the

relaxation times of these fluids ($\lambda \sim 1$ ms). Based on the Maxwell model, the time required for stresses to be dissipated is approximately five times the relaxation time (Bird et al., 1987). However, because stresses relax exponentially ($\tau \sim e^{-t/\lambda} = e^{-1/De_r}$), polymer relaxation increases significantly even at short times. Thus, while the polymer does not relax completely in either channel, the relaxation is significantly greater (because stresses are further dissipated) for the longest contraction ($L_c = 400$ μm) than the other shorter channels. The fluid in the more relaxed state would result in a different pressure drop across the contraction.

6 Conclusion

6.1 Summary

Using soft lithography, microchannels have been generated with sharp features and vertical sidewalls ($87° < \alpha < 93°$) that are accurate to design specifications (within 5%). These channels are designed to generate extensional flows that can be used to quantify rheological behavior of mobile polymer solutions. The lengthscales associated with these channels allow the present study to examine strain rates ($\dot{\varepsilon} \sim 100{,}000$ s^{-1}) which exceed those of previous entry flow experiments.

In this thesis, the flow fields of several different fluids have been observed in planar microfluidic contractions (16:1 and 4:1). The behavior of these fluids is markedly different from the observations of many other researchers on macroscale planar contractions. The resulting elastic instabilities and subsequent vortex growth more closely resembles the observed behavior of axisymmetric contractions because the obtained Deborah numbers (De ~ 300) are much greater than those previously examined (De < 50) at moderate strain. These vortex patterns are observed for two different solutions of PEO in water. The growth of vortices in these two solutions are qualitatively and quantitatively (in terms of vortex length) similar at equivalent Deborah numbers. As vortex growth continues divergent flow is observed and at high Deborah numbers (De $\sim$ 300) flows become unstable. At these large Deborah numbers, tertiary motion is observed in the salient corners. For Newtonian fluids, no such vortices are observed in contraction flows because there is no associated Deborah number. The elasticity number is determined to be the relevant fluid and system property that dictates the vortex behavior in entry flow. Based on the observations in this thesis, figure 6-1 illustrates the progression of vortex behavior that is obtained for a 16:1 planar contraction based on the associated Reynolds number and Deborah number.
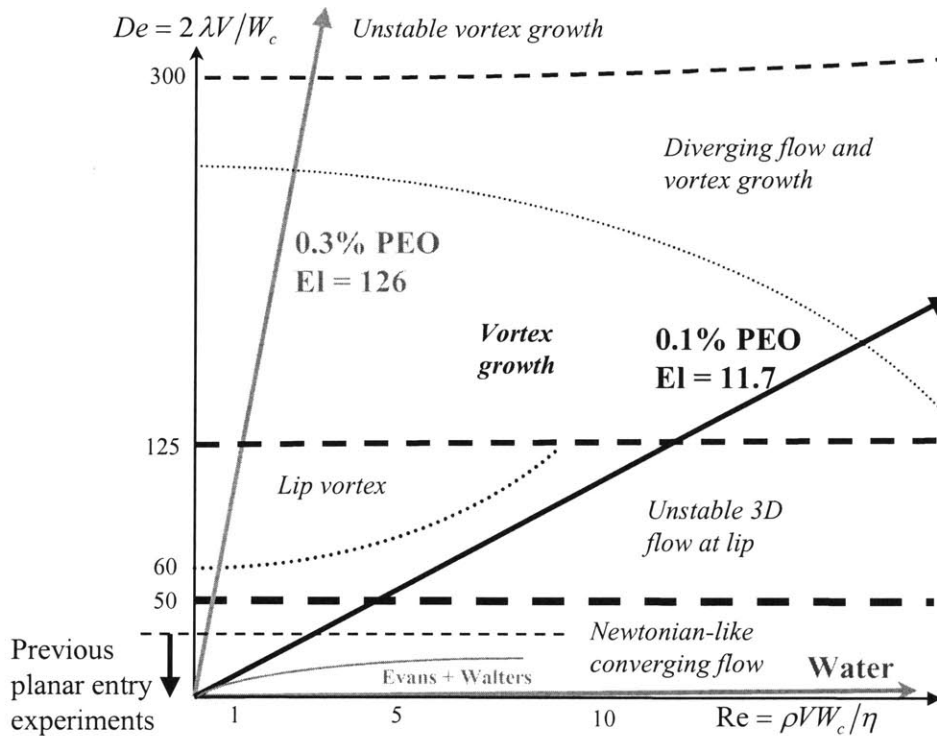
Figure 6-1. Predicted vortex regimes based on the Reynolds and Deborah number for a 16:1 planar contraction.

At abrupt expansions, vortex enhancement is evident for Newtonian fluids. The vortices are a function of inertial forces: growing with Reynolds numbers. For viscoelastic fluids, the elasticity suppresses recirculation at an expansion. Both PEO solutions show vortices at higher flow rates. However, they do not originate at the exit corner (as in Newtonian fluids); instead the vortex behavior originates from the salient corner of the expansion.

A system was also generated to measure the pressure loss for these fluids across the contraction and expansion. The pressure drop in all Newtonian fluids follows a linear path with flow rate. As non-Newtonian fluids are introduced into the system, the pressure drop initially acts in a linear manner. However, at a critical Deborah number the onset of elastic instabilities leads to a dramatic increase in the pressure drop. The onset of non-Newtonian behavior occurs at equivalent Deborah numbers for three non-Newtonian solutions examined ($De \approx 50 \pm 5$). This divergence from Newtonian behavior also corresponds well with the observed onset of elastic instabilities in flow visualization.

This increased pressure loss is associated with the resistance to extension from the polymer molecules. The magnitude of this additional pressure loss is large enough that accepted Cogswell method of evaluating extensional viscosity is unable to capture the nature of this flow. Instead, it is possible to quantify the apparent extensional viscosity of the fluids in this study. These values indicate that extensional viscosities increase by several orders of magnitude at large strain rates. The associated Trouton ratios grow large (Tr ~ 100) with increasing Deborah numbers. Thus, these polymer solutions exhibit highly non-Newtonian extensional properties.

6.2 Future Work

In the present system there is still a limit on the accuracy of measurements due to the extent of shear stress in the channels. By using a hyperbolic channel it may be possible to generate a flow that is shear-free, enabling calculation of an extensional viscosity to be specifically correlated to the entry pressure loss. This requires overcoming the no-slip boundary condition at the channel walls. PDMS is naturally hydrophobic, so it is possible to induce some slip at the walls, but different silane treatments need to be investigated to increase the hydrophobicity of the surfaces.

For the present study, extensive work was performed on the 16:1 planar contraction, however it is necessary to examine the 4:1 planar contraction. Some preliminary experimentation has been done on this geometry, but pressure measurements need to be made to determine the nature of this flow. For both the 16:1 and 4:1 geometries it is necessary to formulate an accurate means of evaluating the characteristic strain rate for the fluid in the converging region. While the Cogswell analysis failed to calculate strain rates, it may be possible to evaluate strain rates directly using micro PIV techniques. However, presently PIV systems respond in such a manner that fluid velocities near the orifice are too large to be captured by the PIV system, which has a minimum response time of approximately 10 μs. In this amount of time, the particles have moved too far for velocities to be calculated by the imaging analysis software. At smaller magnifications,

vector densities are too small to resolve useful information near the entry plane (see figure 6-2).
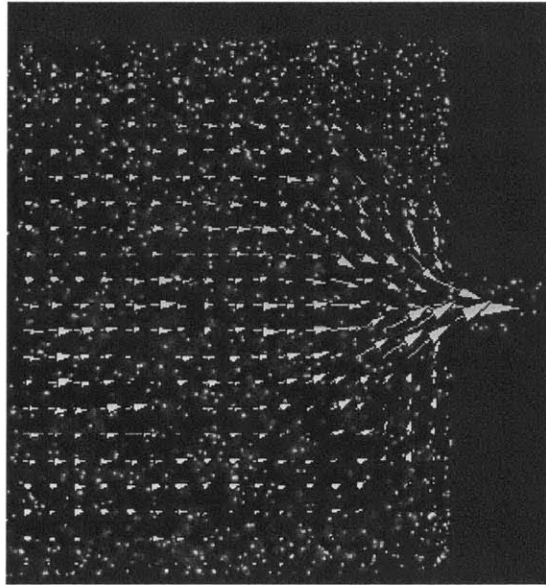
Figure 6-2. Sample micro PIV for water in 16:1 contraction. Field of view is too small to resolve velocities near the contraction.

The final goal of this experimentation is to move to smaller geometries. The natural goal of many researchers is to continuously reduce sizes from the macroscale to the microscale to the nanoscale. For this study the implications of moving to smaller sizes could be significant. At smaller lengthscales, the Deborah numbers will increase and the Reynolds numbers will decrease. Thus, it may be possible to generate significant viscoelastic vortex behavior in infinitely dilute solutions. Elasticity numbers will still be large, and extensional viscosities of such fluids may increase well beyond those measured in the present study.

Advances in technology have made possible nanopores (nanometer sized holes) which generate strain rates large enough to unravel single strands of DNA for subsequent sequencing (Meller et al., 2001; Isambert, 2002). U.S. Genomics has integrated DNA reading technology with a hyperbolic microchannel geometry for rapid analysis of DNA strands (see figure 6-3). Thus, the ability to understand the behavior of fluids in such devices is becoming a pressing requirement for many scientific fields.
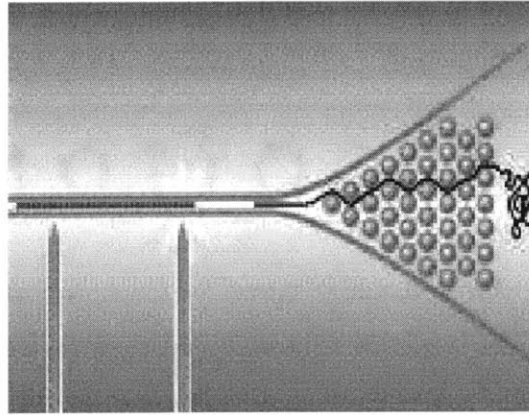
Figure 6-3. Schematic of the nanopore created by U.S. Genomics to unravel single strands of DNA (image courtesy of (Langreth, 2002))

The ultimate goal of any research on entry flow behavior is to understand the nature of the vortex growth and the associated role of extensional viscosity on the entrance pressure loss. From this study it is apparent that it is possible to generate vortices in 16:1 planar contractions, but it is difficult to do so in 4:1 contractions. The elasticity number gives an indication of vortex behavior for flows with similar contraction ratios. However, further understanding of the nonlinear interaction of the contraction ratio and the shear and extensional rheology of the fluid with the generation of elastic behavior needs to be understood. Numerical simulations with realistic viscoelastic constitutive models may prove to be useful in this regard. Using the techniques of soft lithography to manufacture microfluidic devices it is possible to test various fluids and geometries in a short amount of time. Expanding upon this work may lead to understanding definitively the interaction of each rheological factor into how elastic behavior develops in entry flows.

Appendix

	DI Water		0.1% PEO		0.3% PEO		0.05% PEO
	Q (ml/hr)	ΔP (Pa)	Q (ml/hr)	ΔP (Pa)	Q (ml/hr)	ΔP (Pa)	
	0.25	351	0.50	792	0.50	1757	
	0.25	320	1.00	1351	1.00	4376	
	0.50	827	1.50	2054	1.25	8407	
	1.00	1371	1.75	2501	1.50	9372	
	1.50	1764	2.00	2908	1.75	16814	
	1.50	1041	2.25	3549	2.00	18744	
	2.00	1971	2.50	4121	2.25	26117	
	2.00	1399	3.00	6684	2.50	27771	
	2.50	2364	3.50	12197	2.75	34663	
50 μm	3.00	2694	4.00	16056	3.00	39142	
	3.50	2929	4.50	17159			
	3.50	2446	5.00	23499			
	4.00	2894					
	4.50	3218					
	5.00	3577					
	6.00	4417					
	7.00	5327					
	8.00	6347					

	DI Water		0.1% PEO		0.3% PEO		0.05% PEO
	Q (ml/hr)	ΔP (Pa)	Q (ml/hr)	ΔP (Pa)	Q (ml/hr)	ΔP (Pa)	
	0.25	471	0.25	481	0.50	2315	
	0.50	882	0.25	498	0.50	2191	
	0.75	1213	0.50	834	0.50	2412	
	1.00	1413	0.50	889	1.00	4541	
	1.00	1654	1.00	1613	1.25	7098	
	2.00	2839	1.50	2584	1.50	8890	
	3.00	4596	2.00	3735	1.50	10337	
	3.00	4521	2.00	3783	1.75	13920	
	3.00	5306	2.00	3790	2.00	19984	
	4.00	6312	2.00	3894	2.00	19915	
100 μm	5.00	8269	2.50	6216	2.25	24739	
	6.00	11370	2.50	6857	2.25	24395	
			3.00	10130	2.50	29632	
			3.25	11853	2.50	30390	
			3.50	15229	2.75	34456	
			3.75	21914	2.75	33767	
			4.00	24670	3.00	37764	
			4.00	24739			
			4.50	29081			
			5.00	36110			

	DI Water		0.1% PEO		0.3% PEO		0.05% PEO	
	Trial 1							
	Q (ml/hr)	ΔP (Pa)	Q (ml/hr)	ΔP (Pa)	Q (ml/hr)	ΔP (Pa)	Q (ml/hr)	ΔP (Pa)
	0.00	-211	0.10	297	0.25	2653	0.50	2019
	0.50	971	0.25	949	0.50	4500	0.75	3439
	0.75	1553	0.50	1946	0.75	6972	1.00	3818
	1.00	2171	1.00	4087	1.00	10748	1.25	4762
	1.50	3364	1.50	6579	1.25	17601	1.50	5685
	2.00	4579	1.75	8194	1.50	24372	1.75	6684
	2.50	5814	2.00	10089	1.75	31450	2.00	7925
	3.00	7071	2.25	12476	2.00	37811	2.50	11508
	3.50	8334	2.50	16407	2.25	43145	3.00	16263
	4.00	9528	2.75	18302	2.50	49814	3.50	21638
	4.50	10791	3.00	22654	2.75	55559	4.00	26738
	5.00	12055	3.25	26796			4.50	31561
	5.50	13248	3.75	31148			5.00	37143
	6.00	14582						
	7.00	17179						
400 μm			**Trial 2**					
			Q (ml/hr)	ΔP (Pa)				
			0.25	1105				
			0.50	2089				
			1.00	4100				
			1.50	6439				
			2.00	9999				
			2.50	15857				
			3.00	21089				
			4.00	38221				
			4.50	60278				
			5.00	67767				
			6.00	85207				
			Trial 3					
			Q (ml/hr)	ΔP (Pa)				
			0.50	1623				
			0.75	2677				
			1.00	3845				
			1.50	6367				
			2.00	10047				
			2.25	12818				
			2.50	15712				
			2.75	18606				
			3.00	22121				
			3.50	31424				

Works Cited

Agarwal, S. and K. K. Gupta (2002). "An innovative extensional viscometer for low-viscosity and low-elasticity liquids." *Rheologica Acta* **41**(5): 456-460.

Alves, M. A., D. Torres, M. P. Goncalves, P. J. Oliveira and F. T. Pinho (2003). "Visualization Studies of Viscoelastic Flow in a 4:1 Square/Square Contraction." *17th International Congress of Mechanical Engineering.*

Alves, M. A. M. (2004). Laminar flow of viscoelastic fluids: Numerical, theoretical and experimental analysis. Chemical Engineering. Porto, Portugal, University of Porto: 367.

Anna, S. L., N. Bontoux and H. A. Stone (2003). "Formation of dispersions using "flow focusing" in microchannels." *Applied Physics Letters* **82**(3): 364-366.

Bazilevskii, A. V., V. M. Entov and A. N. Rozhkov (2001). "Breakup of an Oldroyd liquid bridge as a method for testing the rheological properties of polymer solutions." *Polymer Science Series A* **43**(7): 716-726.

Beebe, D. J., G. A. Mensing and G. M. Walker (2002). "Physics and applications of microfluidics in biology." *Annual Review of Biomedical Engineering* **4**: 261-286.

Binding, D. M. (1988). "An Approximate Analysis for Contraction and Converging Flows." *Journal of Non-Newtonian Fluid Mechanics* **27**(2): 173-189.

Binding, D. M., M. A. Couch and K. Walters (1998). "The pressure dependence of the shear and elongational properties of polymer melts." *Journal of Non-Newtonian Fluid Mechanics* **79**(2-3): 137-155.

Binding, D. M., M. A. Couch and K. Walters (1999). "The rheology of multigrade oils at elevated pressures." *Journal of Non-Newtonian Fluid Mechanics* **87**(2-3): 155-164.

Binding, D. M. and K. Walters (1988). "On the Use of Flow through a Contraction in Estimating the Extensional Viscosity of Mobile Polymer-Solutions." *Journal of Non-Newtonian Fluid Mechanics* **30**(2-3): 233-250.

Bird, R. B., R. C. Armstrong and O. Hassager (1987). *Dynamics of Polymer Liquids - Volume 1: Fluid Mechanics.* New York, Wiley-Interscience.

Boger, D. V. (1987). "Viscoelastic Flows through Contractions." *Annual Review of Fluid Mechanics* **19**: 157-182.

Boger, D. V., D. U. Hur and R. J. Binnington (1986). "Further Observations of Elastic Effects in Tubular Entry Flows." *Journal of Non-Newtonian Fluid Mechanics* **20**: 31-49.

Brandrup, J., E. H. Immergut and W. McDowell, Eds. (1975). *Polymer Handbook*. New York, Wiley.

Brown, R. A. and G. H. McKinley (1994). "Report on the Viiith Int Workshop on Numerical-Methods in Viscoelastic Flows." *Journal of Non-Newtonian Fluid Mechanics* **52**(3): 407-413.

Cable, P. J. and D. V. Boger (1978). "Comprehensive Experimental Investigation of Tubular Entry Flow of Viscoelastic Fluids .1. Vortex Characteristics in Stable Flow." *Aiche Journal* **24**(5): 869-879.

Cable, P. J. and D. V. Boger (1978). "Comprehensive Experimental Investigation of Tubular Entry Flow of Viscoelastic Fluids .2. Velocity-Field in Stable Flow." *Aiche Journal* **24**(6): 992-999.

Cable, P. J. and D. V. Boger (1979). "Comprehensive Experimental Investigation of Tubular Entry Flow of Viscoelastic Fluids .3. Unstable Flow." *Aiche Journal* **25**(1): 152-159.

Chiba, K., T. Sakatani and K. Nakamura (1990). "Anomalous Flow Patterns in Viscoelastic Entry Flow through a Planar Contraction." *Journal of Non-Newtonian Fluid Mechanics* **36**: 193-203.

Chiba, K., S. Tanaka and K. Nakamura (1992). "The Structure of Anomalous Entry Flow Patterns through a Planar Contraction." *Journal of Non-Newtonian Fluid Mechanics* **42**(3): 315-322.

Chou, H. P., C. Spence, A. Scherer and S. Quake (1999). "A microfabricated device for sizing and sorting DNA molecules." *Proceedings of the National Academy of Sciences of the United States of America* **96**(1): 11-13.

Cogswell, F. N. (1972). "Converging Flow of Polymer Melts in Extrusion Dies." *Polymer Engineering and Science* **12**(1): 64-73.

Cogswell, F. N. (1978). "Converging Flow and Stretching Flow - Compilation." *Journal of Non-Newtonian Fluid Mechanics* **4**(1-2): 23-38.

Cooper-White, J. J., J. E. Fagan, V. Tirtaatmadja, D. R. Lester and D. V. Boger (2002). "Drop formation dynamics of constant low-viscosity, elastic fluids." *Journal of Non-Newtonian Fluid Mechanics* **106**(1): 29-59.

Dagan, Z., S. Weinbaum and R. Pfeffer (1982). "Creeping motion through an orifice." *Journal of Fluid Mechanics* **115**: 505-523.

Delamarche, E., A. Bernard, H. Schmid, B. Michel and H. Biebuyck (1997). "Patterned delivery of immunoglobulins to surfaces using microfluidic networks." *Science* **276**(5313): 779-781.

Deshmukh, S. (2003). Field-Responsive ('Smart') Fluids for Advanced Automotive Applications. Mechanical Engineering. Cambridge, MA, Massachusetts Institute of Technology: 129.

Dontula, P., C. W. Macosko and L. E. Scriven (1998). "Model elastic liquids with water-soluble polymers." *Aiche Journal* **44**(6): 1247-1255.

Duda, J. L. and J. S. Vrentas (1973). "Inviscid Flow Through a Sudden Contraction." *Industrial & Engineering Chemistry Fundamentals* **11**(4): 590-593.

Duffy, D. C., J. C. McDonald, O. J. A. Schueller and G. M. Whitesides (1998). "Rapid prototyping of microfluidic systems in poly(dimethylsiloxane)." *Analytical Chemistry* **70**(23): 4974-4984.

Dwivedi, V. K., R. Gopal and S. Ahmad (2000). "Fabrication of very smooth walls and bottoms of silicon microchannels for heat dissipation of semiconductor devices." *Microelectronics Journal* **31**(6): 405-410.

Effenhauser, C. S., G. J. M. Bruin, A. Paulus and M. Ehrat (1997). "Integrated capillary electrophoresis on flexible silicone microdevices: Analysis of DNA restriction fragments and detection of single DNA molecules on microchips." *Analytical Chemistry* **69**(17): 3451-3457.

Entov, V. M. and E. J. Hinch (1997). "Effect of a spectrum of relaxation times on the capillary thinning of a filament of elastic liquid." *Journal of Non-Newtonian Fluid Mechanics* **72**(1): 31-53.

Evans, R. E. and K. Walters (1986). "Flow Characteristics Associated with Abrupt Changes in Geometry in the Case of Highly Elastic Liquids." *Journal of Non-Newtonian Fluid Mechanics* **20**: 11-29.

Evans, R. E. and K. Walters (1989). "Further Remarks on the Lip-Vortex Mechanism of Vortex Enhancement in Planar-Contraction Flows." *Journal of Non-Newtonian Fluid Mechanics* 32(1): 95-105.

Fay, J. A. (1994). *Introduction to Fluid Mechanics*. Cambridge, Massachusetts, MIT Press.

Fu, A. Y., C. Spence, A. Scherer, F. H. Arnold and S. R. Quake (1999). "A microfabricated fluorescence-activated cell sorter." *Nature Biotechnology* 17(11): 1109-1111.

Gibson, A. G. (1989). "Die Entry Flow of Reinforced Polymers." *Composites* 20(1): 57-64.

Gotsis, A. D. and A. Odriozola (1998). "The relevance of entry flow measurements for the estimation of extensional viscosity of polymer melts." *Rheologica Acta* 37(5): 430-437.

Groisman, A., M. Enzelberger and S. R. Quake (2003). "Microfluidic memory and control devices." *Science* 300(5621): 955-958.

Groisman, A. and S. R. Quake (2004). "A microfluidic rectifier: Anisotropic flow resistance at low Reynolds numbers." *Physical Review Letters* 92(9).

Groisman, A. and V. Steinberg (2000). "Elastic turbulence in a polymer solution flow." *Nature* 405(6782): 53-55.

Groisman, A. and V. Steinberg (2001). "Efficient mixing at low Reynolds numbers using polymer additives." *Nature* 410(6831): 905-908.

Hermansky, C. G. and D. V. Boger (1995). "Opposing-Jet Viscometry of Fluids with Viscosity Approaching That of Water." *Journal of Non-Newtonian Fluid Mechanics* 56(1): 1-14.

Higashitani, K. and W. Pritchard (1972). "Kinematic Calculation of Intrinsic Errors in Pressure Measurements Made with Holes." *Transactions of the Society of Rheology* 16(4): 687-696.

Hillborg, H., J. F. Ankner, U. W. Gedde, G. D. Smith, H. K. Yasuda and K. Wikstrom (2000). "Crosslinked polydimethylsiloxane exposed to oxygen plasma studied by neutron reflectometry and other surface specific techniques." *Polymer* 41(18): 6851-6863.

Isambert, H. (2002). "Voltage addressable nanomemories in DNA?" *Comptes Rendus Physique* **3**(3): 391-396.

James, D. F. and J. H. Saringer (1982). "Planar Sink Flow of a Dilute Polymer-Solution." *Journal of Rheology* **26**(3): 321-325.

Joseph, D. D. (1990). *Fluid Dynamics of Viscoelastic Liquids*. New York.

Karlsson, R., A. Michaelsson and L. Mattsson (1991). "Kinetic-Analysis of Monoclonal Antibody-Antigen Interactions with a New Biosensor Based Analytical System." *Journal of Immunological Methods* **145**(1-2): 229-240.

Kazakia, J. Y. and R. S. Rivlin (1981). "Run-up and Spin-up in a Viscoelastic Fluid .1." *Rheologica Acta* **20**(2): 111-127.

Kim, J. H., A. Oztekin and S. Neti (2001). "Non-linear dynamics of viscoelastic flows in axisymmetric conduits with abrupt changes." *Journal of Non-Newtonian Fluid Mechanics* **97**(2-3): 169-193.

Koizumi, T. and S. Usui (1999). "The dependence of shear and elongational viscosity on the molecular weight of poly(vinylidene fluoride)." *Journal of Applied Polymer Science* **71**(14): 2381-2384.

Koo, J. M. and C. Kleinstreuer (2003). "Liquid flow in microchannels: experimental observations and computational analyses of microfluidics effects." *Journal of Micromechanics and Microengineering* **13**(5): 568-579.

Kwag, C. and J. Vlachopoulos (1991). "An Assessment of Cogswell's Method for Measurement of Extensional Viscosity." *Polymer Engineering and Science* **31**(14): 1015-1021.

Langreth, R. (2002). Speed Reader. Forbes Magazine. **2004**.

Larson, R. G. (1992). "Instabilities in Viscoelastic Flows." *Rheologica Acta* **31**(3): 213-263.

Lorenz, H., M. Despont, N. Fahrni, N. LaBianca, P. Renaud and P. Vettiger (1997). "SU-8: a low-cost negative resist for MEMS." *Journal of Micromechanics and Microengineering* **7**(3): 121-124.

Mackay, M. E. and G. Astarita (1997). "Analysis of entry flow to determine elongation flow properties revisited." *Journal of Non-Newtonian Fluid Mechanics* **70**(3): 219-235.

Macosko, C. W. (1994). *Rheology: Principles, Measurements, and Applications*. New York, Wiley-VCH, Inc.

McDonald, J. C., D. C. Duffy, J. R. Anderson, D. T. Chiu, H. K. Wu, O. J. A. Schueller and G. M. Whitesides (2000). "Fabrication of microfluidic systems in poly(dimethylsiloxane)." *Electrophoresis* 21(1): 27-40.

McKinley, G. H. (2002). Summary of Kuhn Chain Formulae, Massachusetts Institute of Technology.

McKinley, G. H. and R. C. Armstrong (2000). "Rheological Behavior of Polymeric Fluids."

McKinley, G. H., W. P. Raiford, R. A. Brown and R. C. Armstrong (1991). "Nonlinear Dynamics of Viscoelastic Flow in Axisymmetrical Abrupt Contractions." *Journal of Fluid Mechanics* 223: 411-456.

McKinley, G. H. and A. Tripathi (2000). "How to extract the Newtonian viscosity from capillary breakup measurements in a filament rheometer." *Journal of Rheology* 44(3): 653-670.

Meller, A., L. Nivon and D. Branton (2001). "Voltage-driven DNA translocations through a nanopore." *Physical Review Letters* 86(15): 3435-3438.

Metzner, A. B. and A. P. Metzner (1970). "Stress levels in rapid extensional flows of polymeric fluids." *Rheologica Acta* 9: 174-181.

Mitsoulis, E., M. Schwetz and H. Munstedt (2003). "Entry flow of LDPE melts in a planar contraction." *Journal of Non-Newtonian Fluid Mechanics* 111(1): 41-61.

Mun, R. P., J. A. Byars and D. V. Boger (1998). "The effects of polymer concentration and molecular weight on the breakup of laminar capillary jets." *Journal of Non-Newtonian Fluid Mechanics* 74(1-3): 285-297.

Ng, S. L., R. P. Mun, D. V. Boger and D. F. James (1996). "Extensional viscosity measurements of dilute solutions of various polymers." *Journal of Non-Newtonian Fluid Mechanics* 65: 291-298.

Nguyen, H. and D. V. Boger (1979). "Kinematics and Stability of Die Entry Flows." *Journal of Non-Newtonian Fluid Mechanics* 5(APR): 353-368.

Nigen, S. and K. Walters (2002). "Viscoelastic contraction flows: comparison of axisymmetric and planar configurations." *Journal of Non-Newtonian Fluid Mechanics* **102**(2): 343-359.

Olson, D. J. and G. G. Fuller (2000). "Contraction and expansion flows of Langmuir monolayers." *Journal of Non-Newtonian Fluid Mechanics* **89**(1-2): 187-207.

Padmanabhan, M. and C. W. Macosko (1997). "Extensional viscosity from entrance pressure drop measurements." *Rheologica Acta* **36**(2): 144-151.

Purnode, B. and M. J. Crochet (1996). "Flows of polymer solutions through contractions .1. Flows of polyacrylamide solutions through planar contractions." *Journal of Non-Newtonian Fluid Mechanics* **65**(2-3): 269-289.

Qu, W. L., G. M. Mala and D. Q. Li (2000). "Pressure-driven water flows in trapezoidal silicon microchannels." *International Journal of Heat and Mass Transfer* **43**(3): 353-364.

Quake, S. R. and A. Scherer (2000). "From micro- to nanofabrication with soft materials." *Science* **290**(5496): 1536-1540.

Quinzani, L. M., R. C. Armstrong and R. A. Brown (1995). "Use of Coupled Birefringence and Ldv Studies of Flow-through a Planar Contraction to Test Constitutive-Equations for Concentrated Polymer-Solutions." *Journal of Rheology* **39**(6): 1201-1228.

Rajagopalan, D. (2000). "Computational analysis of techniques to determine extensional viscosity from entrance flows." *Rheologica Acta* **39**(2): 138-151.

Rothstein, J. P. and G. H. McKinley (1998). "Extensional flow of a polystyrene Boger fluid through a 4:1:4 axisymmetric contraction/expansion." *Journal of Non-Newtonian Fluid Mechanics* **86**: 61-88.

Rothstein, J. P. and G. H. McKinley (2000). "The axisymmetric contraction-expansion: the role of extensional rheology on vortex growth dynamics and the enhanced pressure drop." *Journal of Non-Newtonian Fluid Mechanics* **98**: 33-63.

Ryssel, E. and P. O. Brunn (1999). "Flow of a quasi-Newtonian fluid through a planar contraction." *Journal of Non-Newtonian Fluid Mechanics* **85**(1): 11-27.

Shaw, M., D. Nawrocki, R. Hurditch and D. Johnson (2003). "Improving the process capability of SU-8." *Microsystem Technologies-Micro-and Nanosystems-Information Storage and Processing Systems* **10**(1): 1-6.

Spiegelberg, S. H., D. C. Ables and G. H. McKinley (1996). "The role of end-effects on measurements of extensional viscosity in filament stretching rheometers." *Journal of Non-Newtonian Fluid Mechanics* **64**(2-3): 229-267.

Stelter, M. and G. Brenn (2000). "Validation and application of a novel elongational device for polymer solutions." *Journal of Rheology* **44**(3): 595-616.

Stelter, M., G. Brenn, A. L. Yarin, R. P. Singh and F. Durst (2002). "Investigation of the elongational behavior of polymer solutions by means of an elongational rheometer." *Journal of Rheology* **46**(2): 507-527.

Stone, H. A. and S. Kim (2001). "Microfluidics: Basic issues, applications, and challenges." *Aiche Journal* **47**(6): 1250-1254.

Tanner, R. I. (1985). *Engineering Rheology.* Oxford, Clarendon.

Tanner, R. I. and A. C. Pipkin (1969). "Intrinsic Errors in Pressure-Hole Measurements." *Transactions of the Society of Rheology* **13**: 471.

Tay, F. E. H., J. A. van Kan, F. Watt and W. O. Choong (2001). "A novel micro-machining method for the fabrication of thick-film SU-8 embedded micro-channels." *Journal of Micromechanics and Microengineering* **11**(1): 27-32.

Thorsen, T., S. J. Maerkl and S. R. Quake (2002). "Microfluidic large-scale integration." *Science* **298**(5593): 580-584.

Tirtaatmadja, V., G. H. McKinley and J. J. Cooper-White (2004). "Drop Formation and Breakup of Low Viscosity Elastic Fluids: Effects of Molecular Weight and Concentration." *Unpublished.*

Tirtaatmadja, V. and T. Sridhar (1993). "A Filament Stretching Device for Measurement of Extensional Viscosity." *Journal of Rheology* **37**(6): 1081-1102.

Townsend, P. and K. Walters (1994). "Expansion Flows of Non-Newtonian Liquids." *Chemical Engineering Science* **49**(5): 749-763.

Trouton, F. T. (1906). "On the coefficient of viscous traction and its relation to that of viscosity." *Proceedings of the Royal Society of London Series A* **77**: 426-40.

Unger, M. A., H. P. Chou, T. Thorsen, A. Scherer and S. R. Quake (2000). "Monolithic microfabricated valves and pumps by multilayer soft lithography." *Science* **288**(5463): 113-116.

Vance, B., D. Bonn, J. Y. Martin and L. Vovelle (2000). "Controlling droplet deposition with polymer additives." *Nature* **405**(6788): 772-775.

Verani, M. and G. H. McKinley (2004). Effects of Polymer Concentration and Molecular Weight on the Dynamics of Visco-Elasto-Capillary Breakup. Aeronautics and Astronautics. Cambridge, MA, Massachusetts Institute of Technology.

Vrentas, J. S. and J. L. Duda (1973). "Flow of a Newtonian fluid through a sudden contraction." *Applied Scientific Research* **28**(4-5): 241-260.

Walters, K. and D. M. Rawlinson (1982). "On Some Contraction Flows for Boger Fluids." *Rheologica Acta* **21**(4-5): 547-552.

Walters, K. and M. F. Webster (1982). "On Dominating Elastico-Viscous Response in Some Complex Flows." *Philosophical Transactions of the Royal Society of London Series a-Mathematical Physical and Engineering Sciences* **308**(1502): 199-&.

White, S. A., A. D. Gotsis and D. G. Baird (1987). "Review of the Entry Flow Problem - Experimental and Numerical." *Journal of Non-Newtonian Fluid Mechanics* **24**(2): 121-160.

Wilding, P., J. Pfahler, H. H. Bau, J. N. Zemel and L. J. Kricka (1994). "Manipulation and Flow of Biological-Fluids in Straight Channels Micromachined in Silicon." *Clinical Chemistry* **40**(1): 43-47.

Xia, Y. N. and G. M. Whitesides (1998). "Soft lithography." *Annual Review of Materials Science* **28**: 153-184.

Xue, S. C., N. Phan-Thien and R. I. Tanner (1998). "Numerical investigations of Lagrangian unsteady extensional flows of viscoelastic fluids in 3-D rectangular ducts with sudden contractions." *Rheologica Acta* **37**(2): 158-169.

Yesilata, B., A. Oztekin, S. Neti and J. Kazakia (2000). "Pressure measurements in highly viscous and elastic fluids." *Journal of Fluids Engineering-Transactions of the Asme* **122**(3): 626-633.

Yoo, J. Y. and D. D. Joseph (1985). "Hyperbolicity and Change of Type in the Flow of Viscoelastic Fluids through Channels." *Journal of Non-Newtonian Fluid Mechanics* **19**(1): 15-41.

Zatloukal, M., J. Vlcek, C. Tzoganakis and P. Saha (2002). "Improvement in techniques for the determination of extensional rheological data from entrance flows:

computational and experimental analysis." *Journal of Non-Newtonian Fluid Mechanics* **107**(1-3): 13-37.

Zhao, B., J. S. Moore and D. J. Beebe (2001). "Surface-directed liquid flow inside microchannels." *Science* **291**(5506): 1023-1026.